HOLST AND TANNEHILL
JULY 1975

Interim Report
ISU-ERI-Ames-75169

NUMERICAL COMPUTATION OF THREE-DIMENSIONAL BLUNT BODY FLOW FIELDS WITH AN IMPINGING SHOCK

Submitted to:
National Aeronautics and Space Administration
Ames Research Center
Moffett Field, California
NASA Grant No. NGR 16-002-038
Principal Investigator: J. C. Tannehill

Project 930-S

ENGINEERING RESEARCH INSTITUTE
IOWA STATE UNIVERSITY
AMES, IOWA 50010 USA

ENGINEERING
RESEARCH

ENGINEERING
RESEARCH

ENGINEERING
RESEARCH

ENGINEERING
RESEARCH

ENGINEERING
RESEARCH

INTERIM REPORT

NUMERICAL COMPUTATION OF THREE-DIMENSIONAL BLUNT BODY FLOW FIELDS WITH AN IMPINGING SHOCK

T. L. Holst
J. C. Tannehill
July 1975

Submitted to:
Mr. John V. Rakich, Technical Officer
National Aeronautics and Space Administration
Ames Research Center
Moffett Field, California
NASA Grant No. NGR 16-002-038

ISU-ERI-Ames-75169
Project 930-S

ENGINEERING RESEARCH INSTITUTE
IOWA STATE UNIVERSITY AMES

NUMERICAL COMPUTATION OF THREE-DIMENSIONAL BLUNT BODY FLOW FIELDS WITH AN IMPINGING SHOCK

Terry L. Holst and John C. Tannehill
Iowa State University

SUMMARY

A time-marching finite-difference method has been used to solve the compressible Navier-Stokes equations for the three-dimensional wing-leading-edge shock impingement problem. The bow shock was treated as a discontinuity across which the exact shock jump conditions were applied. All interior shock layer detail such as shear layers, shock waves, jets, and the wall boundary layer are automatically captured in the solution. The impinging shock was introduced by discontinuously changing the freestream conditions across the intersection line at the bow shock. A special storage-saving procedure for sweeping through the finite-difference mesh has been developed which reduces the required amount of computer storage by at least a factor of two without sacrificing the execution time. Numerical results are presented for infinite cylinder blunt body cases as well as the three-dimensional shock impingement case. The numerical results are compared with existing experimental and theoretical results.

TABLE OF CONTENTS

LIST OF TABLES

LIST OF FIGURES

Figure Page

LIST OF SYMBOLS

a	speed of sound
c	mesh stretching parameter ($= \ln((\beta+1)/(\beta-1))$)
c_1	constant in Sutherland's formula ($= 1.2585 \times 10^{-8}$ N-sec/m^2 - $^{\circ}$K$^{1/2}$ for air)
c_2	constant in Sutherland's formula (= 110.4 $^{\circ}$K for air)
c_i, c_j, c_k	smoothing coefficients in the r-, θ-, and z-directions, respectively
c_p	coefficient of specific heat at constant pressure (= 1004.585 m^2/sec^2 - $^{\circ}$K for air)
c_v	coefficient of specific heat at constant volume (= 717.561 m^2/sec^2 - $^{\circ}$K for air)
C	constant of proportionality
D	cylinder diameter or vector defined by Equation 2.31
$\overline{D}$	vector defined by Equation 2.6
DR	density ratio ($= \rho_\infty/\rho_2$)
DR$_{com}$	density ratio computed from Equation A.7
e	specific internal energy
e_{ij}	rate of strain tensor
E	total energy ($= \rho(e + (u_r^2 + u_\theta^2 + u_z^2)/2)$)
f	mesh stretching function in the radial direction
F	vector defined by Equation 2.28
$\overline{F}$	vector defined by Equation 2.3
g	mesh stretching function in the cross-flow direction
gR	universal gas constant (= 287.024 m^2/sec^2 - $^{\circ}$K for air)
G	vector defined by Equation 2.29
$\overline{G}$	vector defined by Equation 2.4

h	static enthalpy or heat transfer coefficient $(= q/(T_{aw} - T)c_p)$
H	vector defined by Equation 2.30
$\bar{H}$	vector defined by Equation 2.5
H_t	total enthalpy
$\hat{i}_r, \hat{i}_\theta, \hat{i}_z$	orthogonal set of unit vectors in the cylindrical coordinate system fixed with respect to the body
$\hat{i}_N, \hat{i}_T, \hat{i}_B$	orthogonal set of unit vectors in the shock-fixed coordinate system where $\hat{i}_N$ is the outward normal to the bow shock and $\hat{i}_T$ and $\hat{i}_B$ are tangent
J	proportionality factor between heat and work (= 4184 Joules/Kcal)
k	coefficient of thermal conductivity $(= c_p\mu/Pr)$
K_i^n	variable smoothing coefficient defined by Equation 3.33
M	Mach number $\left(= \sqrt{u_r^2 + u_\theta^2 + u_z^2}\Big/ a\right.$
p	pressure
Pr	Prandtl number $(= c_p\mu/k)$ (= 0.72 for air)
PR	pressure ratio across impinging shock $(= p_\infty/p_1)$
q_n	heat transfer rate $(= c_p k(\partial H_t/\partial n))$
q_i	heat transfer rate vector $(= q_r, q_\theta, q_z$ or $q_\xi, q_\eta, q_\zeta)$
r, θ, z	position components in the cylindrical coordinate system (physical domain)
r_b	body radius
r_p	impinging shock radius
r_s	bow shock radius
r_{s_t}	radial shock velocity $(= \partial r_s/\partial t)$
r_{s_θ}	bow shock slope in θ-direction $(= \partial r_s/\partial \theta)$

r_{s_z}	bow shock slope in z-direction ($= \partial r_s/\partial z$)
r_x	distance along a radial ray at $\theta = 0^\circ$
r_y	distance along a radial ray at $\theta = 90^\circ$
Re_D	Reynolds number based on cylinder diameter ($= \rho VD/\mu$)
S	smoothing terms defined by Equations 3.36, 3.37 and 3.38
t	time in the physical domain
T	temperature
T_{aw}	adiabatic wall temperature
u_N, u_T, u_B	velocity components in the shock-fixed coordinate system
u_r, u_θ, u_z	velocity components in the cylindrical coordinate system
U	vector defined by Equation 2.27
$\bar{U}$	vector defined by Equation 2.2
V	velocity vector
V_N	freestream velocity component normal to the bow shock measured in the shock-fixed coordinate system and positive inward
$\vec{V}_{s/b}$	velocity of the bow shock relative to the body
x	quantity defined by Equation 2.18
x_1	normalized distance between body and first grid row just off body
x_2	normalized distance between body and second grid row just off body
x_{int}	intersection location of the planar impinging shock along the x-axis (i.e., $r, \theta, z = x_{int}, 0, 0$)
z_{int}	intersection location of the planar impinging shock along the z-axis
α	z-direction bow shock smoothing coefficient

β	stretching parameter controlling radial mesh point distribution, practical range is $1 < \beta < 2$ with smaller values giving larger amounts of refinement at the body
γ	ratio of specific heats (= 1.40 for air)
$\delta()$	first-order forward-difference operator defined by Equation 3.34
$\Delta()$	first-order backward-difference operator defined by Equation 3.35
$\Delta r, \Delta\theta, \Delta z$	increments in the r-, θ-, and z-directions, respectively
$\Delta\xi, \Delta\eta, \Delta\zeta$	increments in the ξ-, η-, and ζ-directions, respectively
$\Delta\tau$	increment in time
λ	cylinder sweep angle
μ	coefficient of viscosity computed from Sutherland's equation (= $c_1 T^{3/2}/(T + c_2)$)
ξ, η, ζ	position coordinates in the computational domain
ρ	density
$\sum_{\ell=i,j,k}$	summation notation one term for each spacial direction (i, j, and k)
τ	time in the computational domain
τ_{ij}	stress tensor
$\nabla()$	del operator defined by Equation B.16

Subscripts:

b	quantity measured in the body-fixed coordinate system (r, θ, z)
i, j, k	mesh position subscripts in the ξ-, η-, and ζ-directions, respectively, such that $\xi = i\Delta\xi$, $\eta = j\Delta\eta$, and $\zeta = k\Delta\zeta$
max	maximum value
min	minimum value

NI,NJ,NK	maximum values for the i,j,k subscripts, respectively
p	peak value
s	quantity measured in the shock-fixed coordinate system
stag	no impingement stagnation point or stagnation line quantity
u	undisturbed or no impingement quantity
w	wall quantity
1	downstream side of impinging shock
2	downstream side of bow shock
∞	freestream side of bow shock

Superscripts:

c	corrector-smoother step
cp	completor-predictor smoother step
m	exponent, empirically determined for peak heating correlation (Equation 1.1)
n	time step number
$\bar{n}$	time step number for a predictor step
pp	partial-predictor or partial-predictor-smoother step
pc	partial-corrector step
$*$	quantity normalized by corresponding freestream or stagnation quantity

Other:

$\vec{(\ )}$	vector quantity

I. INTRODUCTION

When an extraneous shock strikes the bow shock of a blunt body, a complicated flow pattern results which may contain imbedded shock waves, shear layers, expansion fans or supersonic jets. In addition, large increases in wall heat transfer and pressure can occur and have been measured experimentally by many investigators. Impinging shock flow fields may occur on hypersonic aircraft or reentry vehicles such as the Space Shuttle.

A. Classification of Shock Impingement

The different flow fields which can result have been categorized by Edney [1] into six basic types of shock interference patterns. These patterns are shown in Figures 1-6. Impinging shock strength, freestream Mach number, body shape, and position of impingement (with respect to the subsonic flow region on the blunt body) are the primary factors in determining the type of shock impingement.

A Type I interference pattern (shown in Figure 1) occurs when the impinging shock strikes the bow shock well above the upper sonic line. In this case the impinging and bow shocks are of opposite families. The shear layer emanating from the intersection point does not strike the body and therefore, does not contribute to increases in wall pressure or local heating. However, the transmitted impinging shock can strike the body. If strong enough, this transmitted shock can cause boundary layer separation or transition from laminar to turbulent flow. Increases in

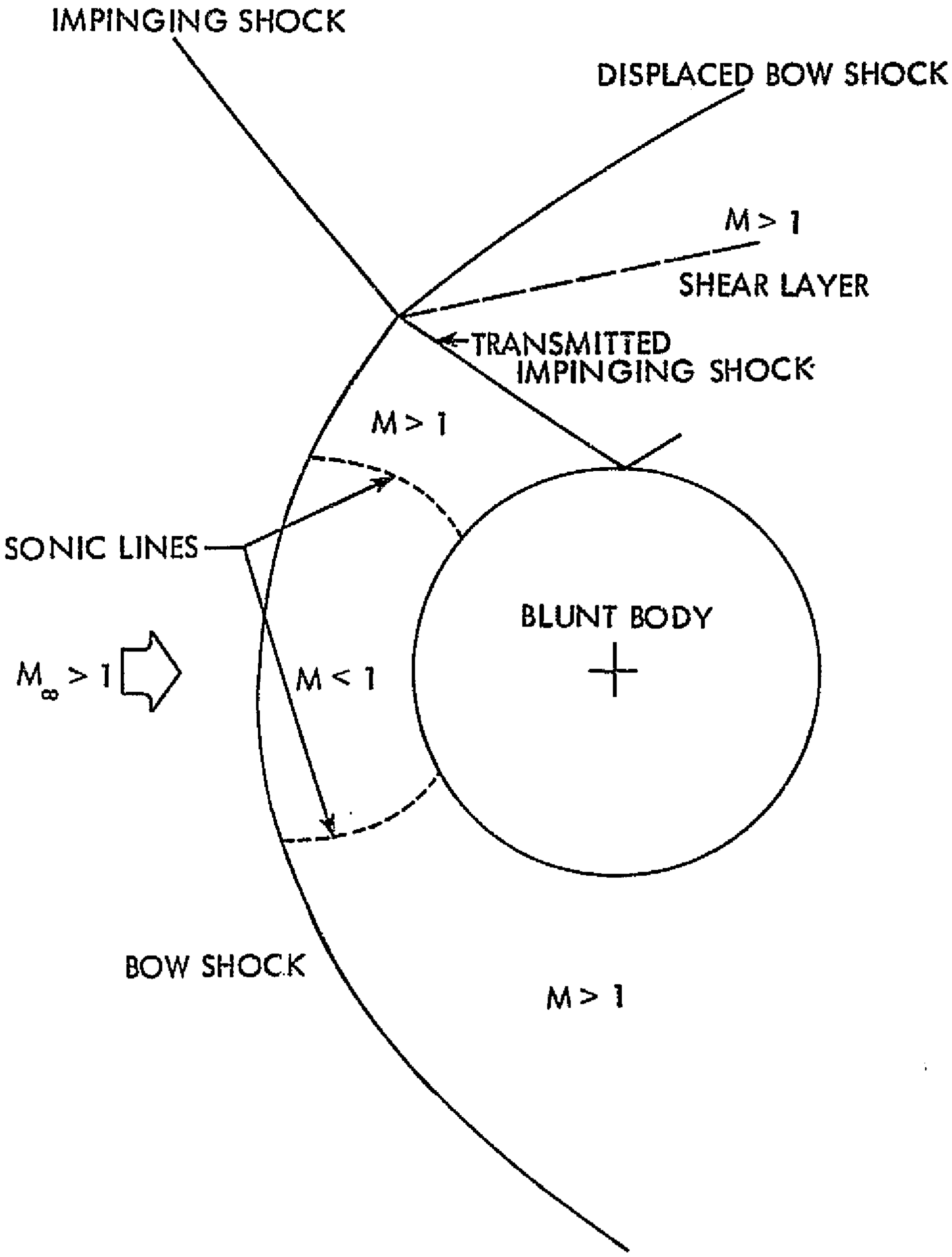

Figure 1. Type I shock interference.

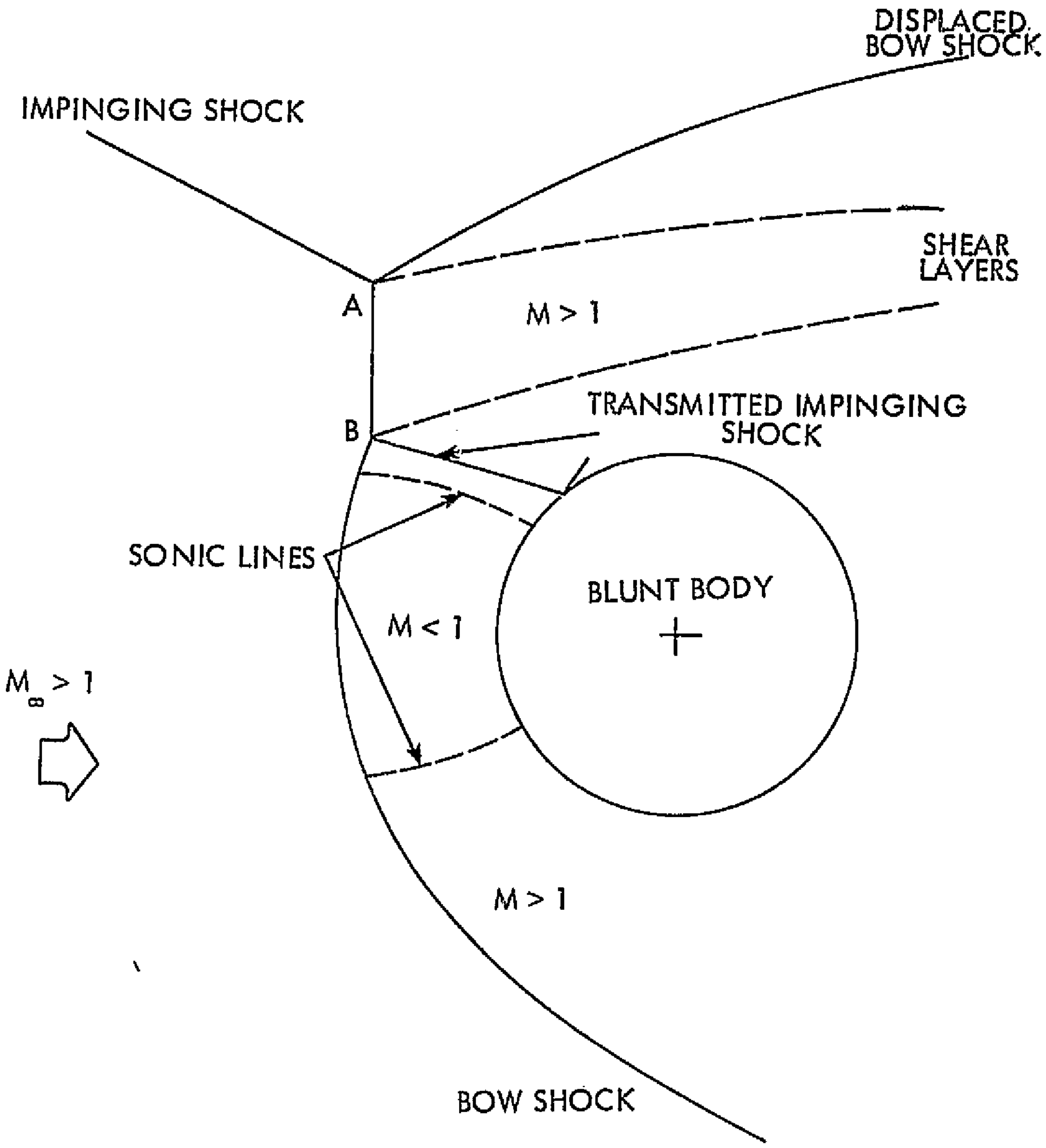

Figure 2. Type II shock interference.

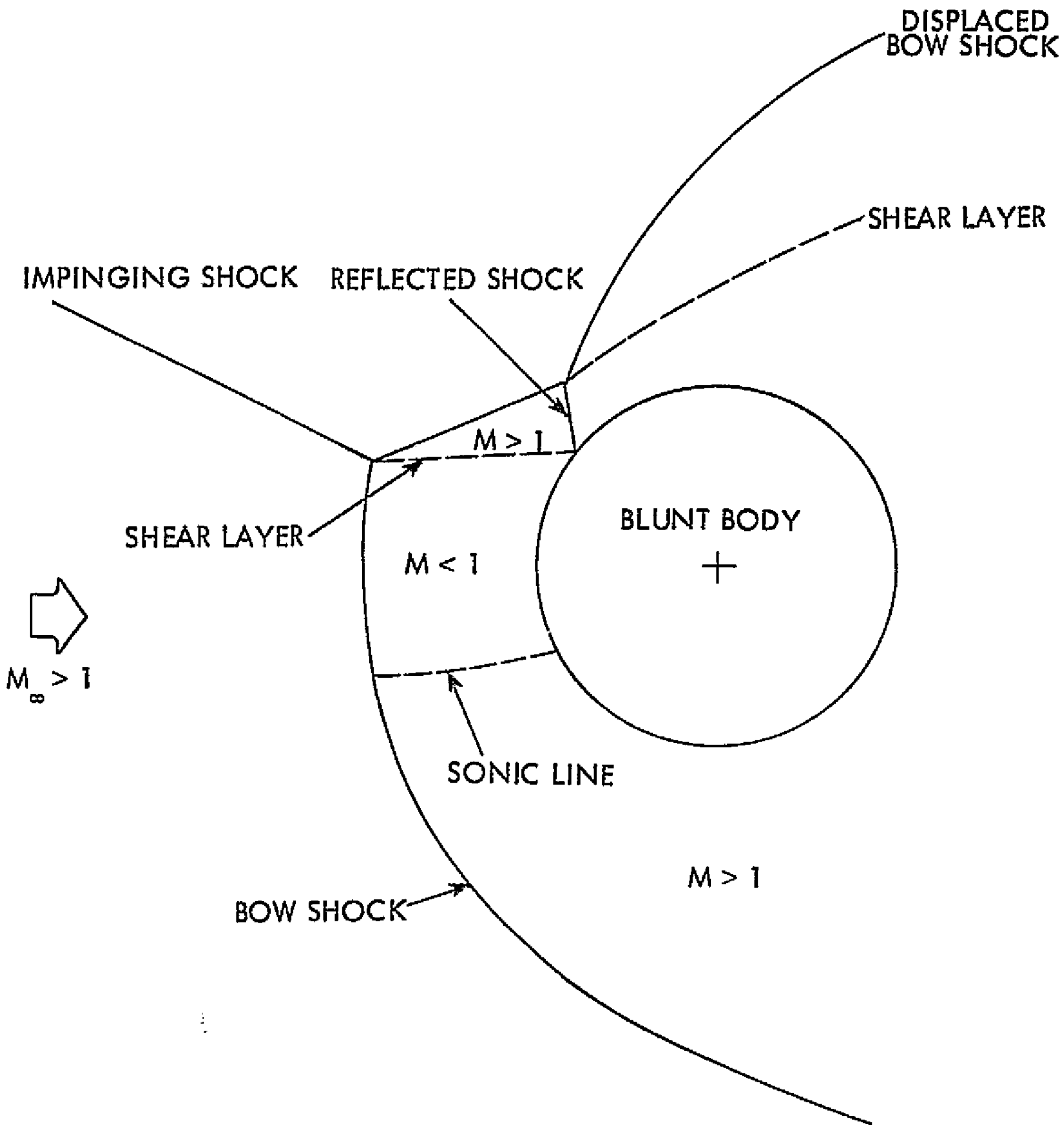

Figure 3. Type III shock interference.

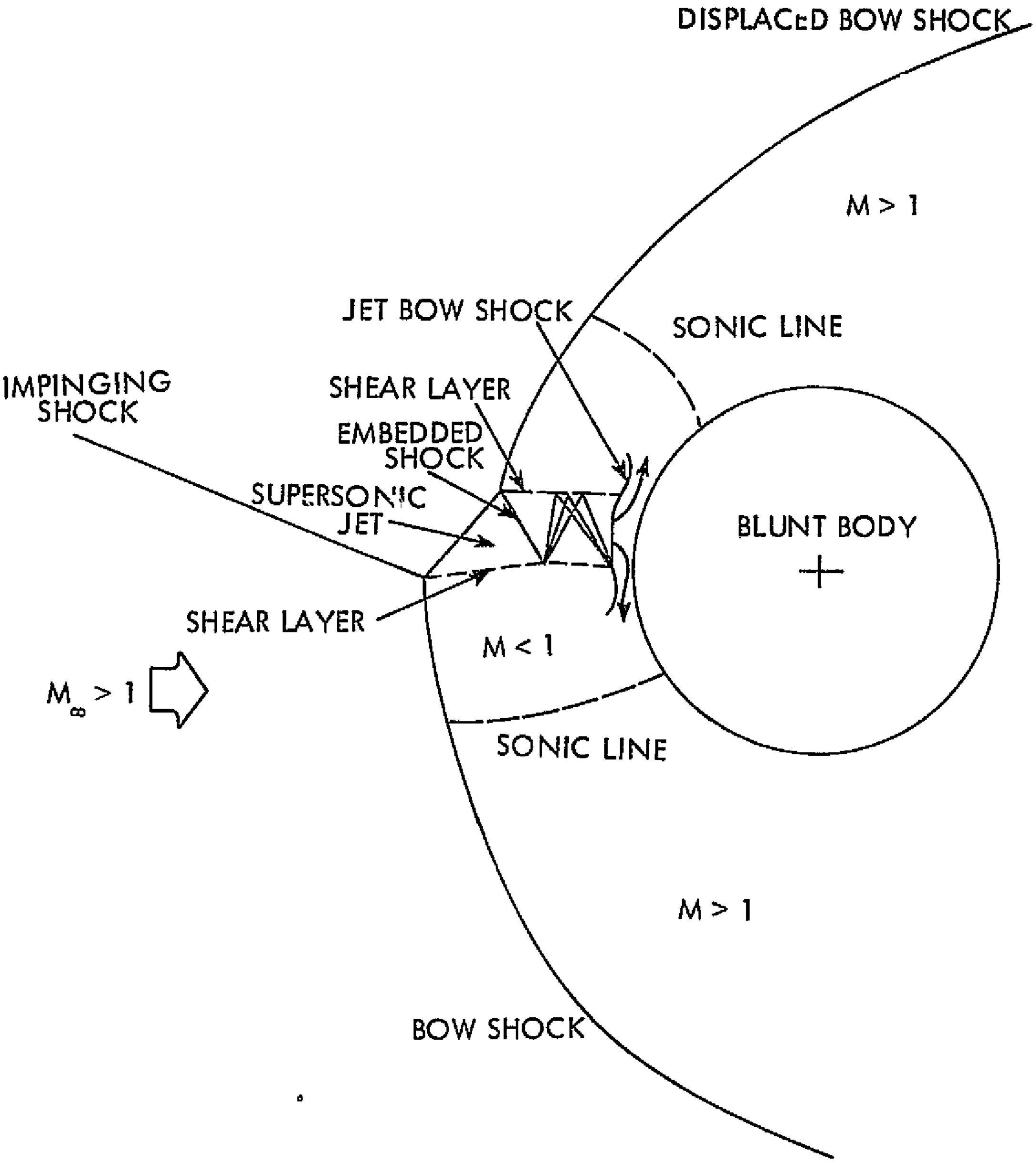

Figure 4. Type IV shock interference.

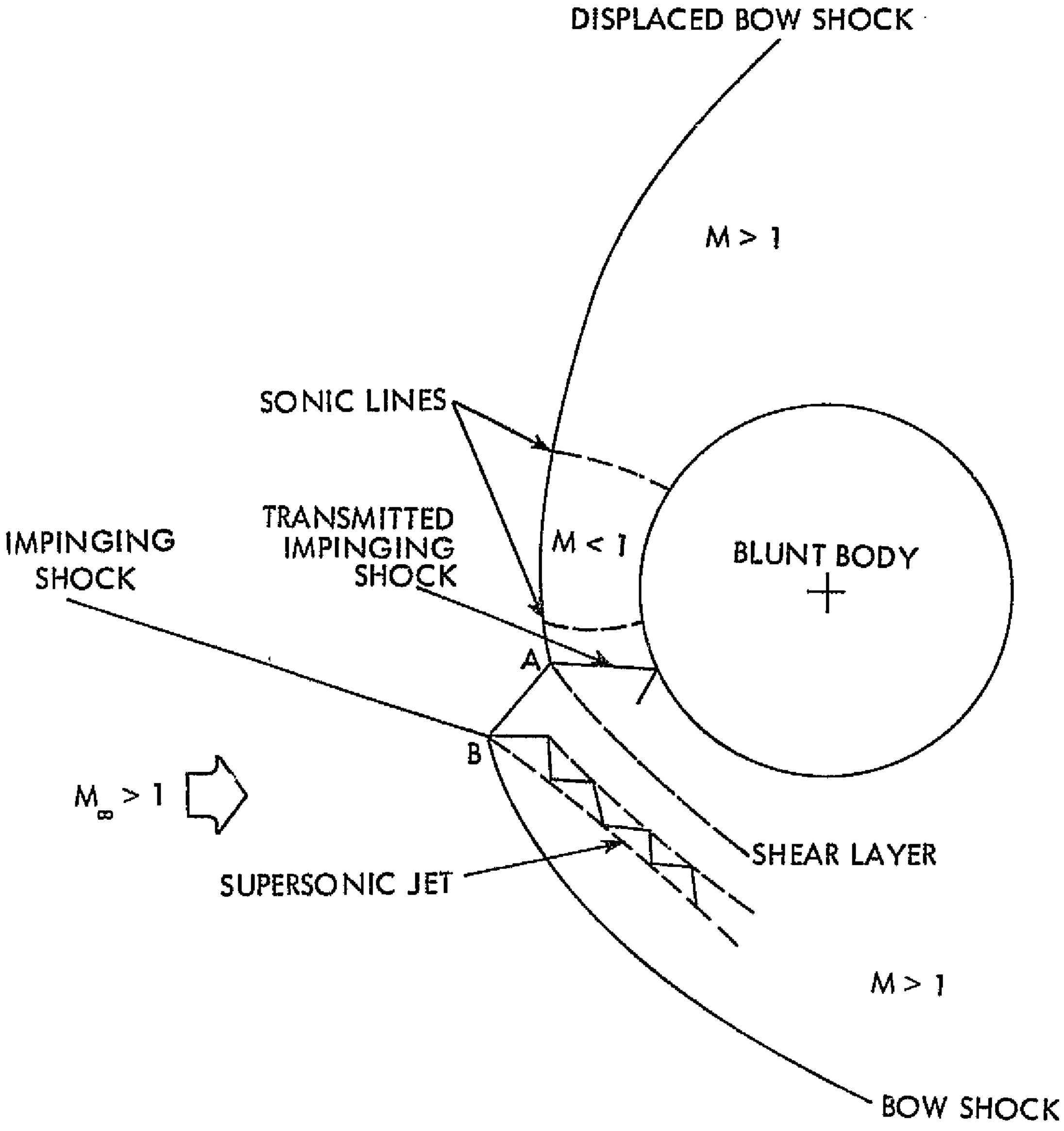

Figure 5. Type V shock interference.

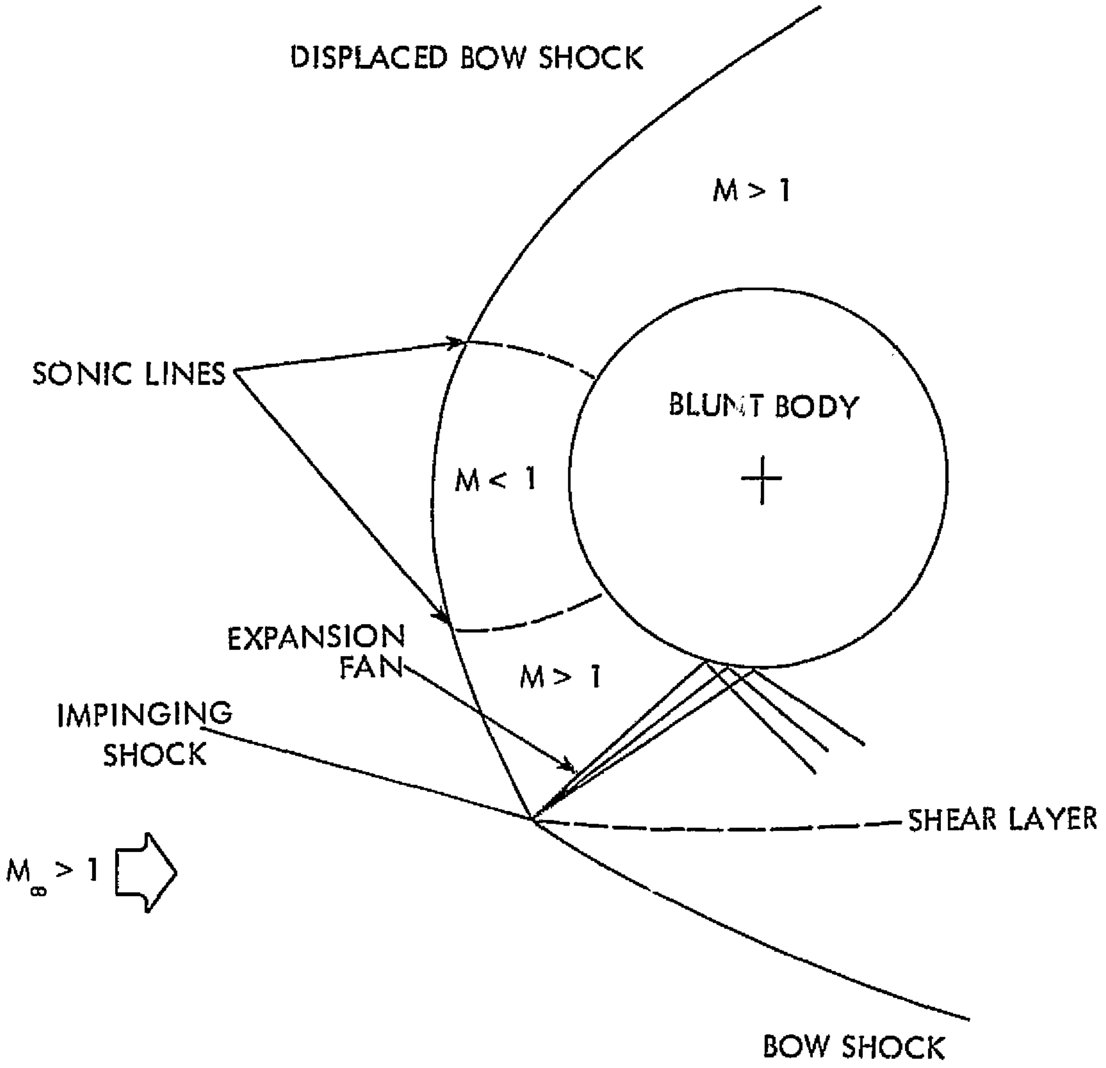

Figure 6. Type VI shock interference.

wall pressure and heat transfer can then result from this shock-boundary layer interaction. Heating amplifications as large as ten can result from a Type I interference.

A Type II interference pattern (shown in Figure 2) occurs when the impinging shock strikes the bow shock just above the upper sonic line. In this case the impinging and bow shocks are also of opposite families. The transmitted impinging shock strikes the body surface resulting in possible boundary layer separation or transition. In addition, two shear layers are formed which may strike the body to cause additional heating and pressure peaks. The shear layer emanating from point B is very weak and can cause only small heating and pressure amplifications. On the other hand, the shear layer emanating from point A is strong and can cause large increases in heating and pressure. Heating amplifications as large as five can be expected from a Type II interference.

A Type III interference pattern (shown in Figure 3) occurs when the impinging shock strikes the bow shock just inside the upper sonic line. A shear layer emanates from the intersection point and strikes the body causing large increases in heat transfer and wall pressure at this point. This shear layer separates regions of subsonic and supersonic flow. The supersonic flow is turned parallel to the body by an oblique shock which exists between the bow shock and the body. Heating amplifications as large as ten can be expected for a Type III interference.

When flow conditions for the Type III case become such that the oblique shock no longer is able to turn the flow parallel to the body, a Type IV shock interference is formed and is shown in Figure 4. This interference pattern occurs when the impinging shock strikes the near-normal part of the bow shock. Imbedded in the subsonic portion of the blunt body flow is a supersonic jet which is terminated by a normal jet bow shock just above the body. The Type IV interference pattern produces the largest heating and pressure peaks due to the jet impingement upon the body. Heating peaks as high as 17 times the undisturbed stagnation value and pressure peaks as high as 8 times the undisturbed stagnation value have been measured [2].

A Type V interference pattern (shown in Figure 5) occurs when the impinging shock strikes the bow shock just below the lower sonic line. This case is nearly a mirror image of the Type II case, except the impinging and bow shocks are of the same family and a thin supersonic jet emanates from the impingement point (point B) instead of a shear layer. Heating amplifications as large as five can be expected for a Type V interference.

A Type VI interference pattern (shown in Figure 6) occurs when the impinging shock strikes the bow shock well below the lower sonic line. This interaction is analogous to the Type I case except that the impinging and bow shocks are of the same family and an expansion fan is transmitted instead of a shock. The interaction of the expansion fan and the wall boundary layer results in a small decrease in the wall pressure and heat transfer.

Further details about the different shock interference patterns are given in the original work by Edney. In addition, an informative discussion on shock interference classification is given by Keyes and Hains [2].

A two-dimensional shock interference geometry is shown in Figure 7a. This geometry can produce any of the six interference patterns. The impinging shock is planar and oriented such that the intersection line is parallel to the axis of the cylinder, causing the flow in each z-plane to be identical. This geometry is important because it qualitatively models the flow field in many three-dimensional cases.

A more physically realistic geometry occurs when a planar impinging shock intersects a circular cylinder as shown in Figure 7b. This configuration can occur when the bow shock from the nose of a vehicle strikes the wing leading edge bow shock. A fully three-dimensional calculation must be performed to obtain this flow field. The sweep angle of the cylinder is a critical parameter in this case because it controls the interference pattern type. For zero or small sweep angles a Type IV interference pattern will result. For moderate sweep angles (around 30°) a Type V interference pattern will occur. For larger sweep angles a Type VI interference pattern will result. Because swept forward wings generally do not exist, Types I, II, and III are not considered for the wing leading edge case. Further discussion about this geometry and some of its flow field detail is presented in the following sections.

B. Literature Review

1. Experimental shock impingement studies

The large number of publications appearing in the literature on shock interference is indicative of the amount of work being done in this area. Because of the complexity of the problem, most studies have been

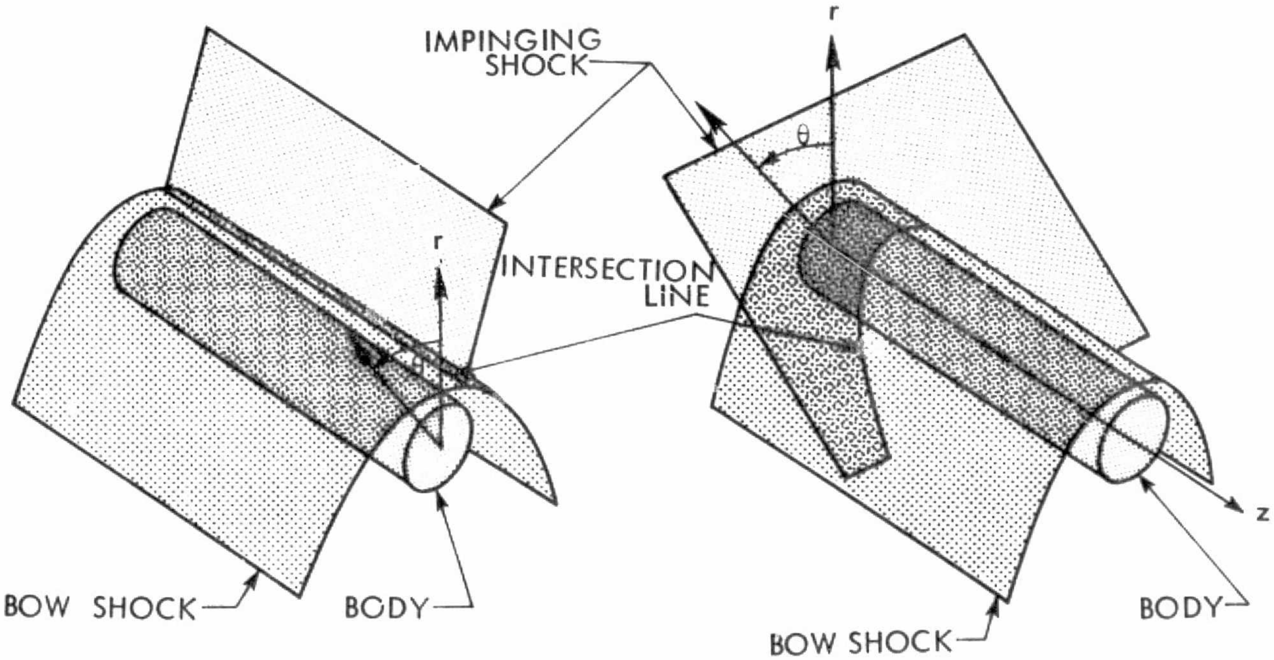

(a) TWO-DIMENSIONAL

(b) THREE-DIMENSIONAL

Figure 7. Shock impingement geometries.

experimental or have used a highly simplified model in a theoretical analysis.

Edney [1], Keyes and Hains [2], and Korkegi [3] provide an extensive survey of the literature on the shock interference problem. References [1] and [4-29], which are reviewed by Keyes and Hains, represent the bulk of the experimental effort from 1961 to 1972. Many different experimental approaches have been used to study the problem of shock interference. The hemisphere and leading edge impingement geometries have received most of the attention. The effects of Reynolds number, Mach number, impinging shock strength, and sweep angle have been recorded through various pressure, heat transfer, and flow visualization measuring techniques. The scatter in the experimental data is unusually large, especially the peak values of heat transfer and pressure. This can be attributed to the very small region over which an impingement interaction occurs, making accurate measurements difficult.

As described earlier, Edney in 1968 published a classical paper on shock impingement in which six basic shock interference patterns were classified (see Figures 1-6). In addition, new techniques for heat transfer measurement were developed which improved the accuracy of the peak heating measurements. In addition to heat transfer measurements, pressure measurements and Schlieren photographs were obtained for hemispheres, leading edge fins, wedges, and flat-faced cylinders.

Keyes and Hains [2] and Hains and Keyes [30] published the results of extensive experimental investigations of shock impingement. All six impingement types due to Edney were investigated. Planar shocks were allowed to impinge upon the bow shocks surrounding both hemispherical and swept fin models. Heat transfer measurements were made by using a phase-change coating technique. This technique has the ability to detect heating peaks over very narrow regions. The heat transfer results, however, are subject to numerous and often large sources of error associated with the measurement of 1) thermophysical properties of the model material, 2) melt temperature, 3) melt time, 4) initial model temperature, and 5) adiabatic wall temperature distribution. Peak heat transfers of 17 times the undisturbed stagnation values and peak pressures of 8 times the undisturbed stagnation pressures were measured for the most critical (Type IV) hemispherical case. In an additional report by Keyes [31], off-center-line heating rates were measured for both hemispheres and swept fins. Heating rates higher than the undisturbed stagnation value due to shock impingement were found over significant portions of the off-center-line body surface.

Doughty et al. [32] determined angle of attack effects on shock impingement heating rates by testing several delta-wing space shuttle models. The same phase-change coating technique was used in this investigation as was used in references [2] and [30]. At low angles of attack (20°), the heating rate increases (due to shock impingement) were restricted to the vicinity of the wing leading edge. Heating rates on the windward side of the trailing edge were almost unaffected by the shock impingement. At moderate angles of attack (40°) increased heating rates due to shock impingement were experienced over a very large portion of the windward side of the wing. No mention was made of the heating rates on the leeward side of the wing.

Other recent experimental studies were performed by Bertin and Hinkle [33], Palko [34], and Craig and Ortwerth [35]. Bertin and Hinkle used a double wedge model to approximate the wing leading edge problem. Palko conducted an extensive series of experiments also on the wing leading edge problem. Stagnation line pressure and heat transfer measurements and Schlieren photographs were obtained for systematic variations of freestream Mach number, leading edge sweep angle, and impinging shock strength.

Craig and Ortwerth investigated the leading edge shock impingement problem but with a different impinging shock orientation. The orientation studied was that of the two-dimensional type shown in Figure 7a. This orientation exactly duplicates the type of flow fields shown in Figures 1-6. Pressure and heat transfer measurements and Schlieren photographs were obtained.

2. Theoretical shock impingement studies

Many authors from references [4-29] have offered theoretical models and methods of peak heating prediction. Most of these authors, however, do not present a conclusive understanding of the shock impingement problem. The results, therefore, are in most cases not satisfactory [2].

Edney established flow models for each of the six shock interference patterns. By determining the nature of the shock interference flowfields, Edney established the mechanisms which produce the pressure and heating peaks. These peaks are caused by one or more of the following phenomena: 1) shock-boundary layer interaction, 2) free shear layer attachment, and 3) supersonic jet impingement. From these flow models semiempirical methods for predicting the approximate flow fields were developed. Edney presented two methods, a graphical method and a numerical method.

The graphical approach, referred to as the heart diagram method, is based on a plot of pressure versus flow deflection angle and can be used to describe the flow fields for each of the six shock interaction types.

The numerical method presented by Edney utilizes the oblique shock relations and an iterative procedure. Types I and VI can be solved exactly while Types II through V require semiempirical values for certain characteristic lengths.

Crawford [36] improved Edney's graphical approach by removing the iteration procedure. This was accomplished by plotting a family of pressure deflection curves with the pressure ratio on a logarithmic scale and flow deflection on a linear scale.

Bramlette [37] improved Edney's numerical scheme with two simplifying assumptions. This modified technique can only be applied to Type III and Type IV interactions, but removes the iterative portion of the solution without sacrificing the accuracy.

Many authors have presented correlations for peak heating due to shock-boundary layer interactions and free shear layer attachment [38-43]. The most useful shock-boundary layer correlation, developed by Markarian [38] and used for shock impingement problems by Keyes and Morris [43], is based upon the inviscid pressure rise across the interaction region. The basic expression is given by

$$\frac{h_p}{h_u} = C\left(\frac{p_p}{p_u}\right)^m \qquad 1.1$$

where h_p and h_u are the peak and undisturbed values of the heat transfer coefficient, respectively, p_p and p_u are the peak and undisturbed values of wall pressure, respectively, and C and m are empirical constants which depend upon the nature of the boundary layer (i.e., laminar, transitional, or turbulent).

The boundary layer reattachment correlation for peak heating, presented by Bushnell and Weinstein [42], was used by Keyes and Morris for the shock impingement free shear layer attachment problem.

Keyes and Hains [2] and Hains and Keyes [30] present the results of an extensive theoretical study of all six types of shock impingement. The flow models introduced by Edney and the peak heating correlations described above have been utilized and extensively compared with experimental results. These theoretical methods for each impingement type have been coded into computer programs and are listed along with detailed descriptions in reference [44]. These theoretical methods provide fast, easily obtainable, and in most cases (where real gas effects are negligible and good flow visualization photographs are available) adequate answers for the peak heating and pressure values resulting from the shock impingement. However, many disadvantages for these theoretical methods exist [2]: 1) The models used are local, two-dimensional models and do not include three-dimensional effects. 2) The calculations are based upon flow visualization photographs or other empirical sources. 3) Shear layer growth or oblique jet impingement are not included.

4) Gas chemistry is not included.

Bertin et al. [45] presented a theoretical study of shock impingement (Types V and VI) on a double wedge model. Real gas effects were included. The method utilized oblique shock relations. Included were perfect gas results, variable gamma (γ) results and results for air in chemical equilibrium in which all properties were obtained by a table look-up scheme. Because of real gas effects, Bertin et al. [45] concluded that extrapolation of wind tunnel data to flight conditions may yield inaccurate results (e.g., in the case of the Space Shuttle).

3. Numerical shock impingement studies

The numerical schemes for computing blunt body flow fields have had a pronounced effect upon shock impingement numerical solutions. Therefore, a brief discussion of blunt body numerical solutions is presented first.

Many schemes have been developed to solve the classical blunt body problem in a supersonic flow. Discussion and classical theory on the blunt body problem can be found in Hayes and Probstein [46]. Daywitt and Anderson [47]present a review of blunt body solutions in which special attention is given to the time-dependent, finite-difference approach. Two basic variations utilizing the time-dependent approach have been developed. The simplest is the so-called "shock-capturing" technique [48-50]. In this technique the detached bow shock is automatically computed with no a priori knowledge of its location or even existence.

The later technique is the so-called "shock-fitting" technique [51]. The bow shock in this approach is assumed to be a boundary of the computational mesh across which the exact shock jump conditions (Rankine-Hugoniot relations) are applied.

Another study [52] presented a viscous blunt body solution for a gas in chemical nonequilibrium. The time-dependent shock fitting approach was used in conjunction with the Navier-Stokes equations. In this approach, not only the inviscid flow field, but also the boundary layer and the chemical species concentrations were computed.

Other numerical techniques for blunt body flows exist, but are not discussed here. Instead, the topic is changed to blunt body flows with an impinging shock.

Tannehill and Holst [53] and Tannehill et al. [54] both obtained two-dimensional shock impingement solutions using the time-dependent approach. In both papers, the complete Navier-Stokes equations were solved. The geometry used is shown in Figure 7a.

The first paper obtained a low Reynolds number solution simulating high altitude conditions by using the shock capturing approach. In addition, a preliminary study of fitting the bow shock and capturing all shock layer detail was presented.

The second paper presented several moderate Reynolds number solutions utilizing the shock fitting method. The impinging shock was introduced by discontinuously changing the freestream conditions at the bow shock.

Holst et al. [55] presents a brief discussion of the present results.

This completes the literature review. A brief presentation of the methodology used in the present study for computing shock impingement flow fields is presented in the next section.

C. Present Methodology

In the present study the three-dimensional wing leading edge shock impingement flow field is numerically computed by using a time-dependent finite-difference method. The choice of a numerical method to solve shock impingement flow fields seems well suited because of the complicated type of problem involved.

The three-dimensional formulation is important. The inclusion of the third dimension provides a "relief effect" which can drastically alter two-dimensional results.

The time-dependent approach was chosen because a subsonic region may exist along the stagnation plane of the wing leading edge. Even if the cross-flow velocity is supersonic before impingement, a subsonic region may form after the impinging shock has been introduced. Since the governing time-dependent equations remain a hyperbolic-parabolic set for both subsonic and supersonic flows, all cases can be solved as an initial-value problem where the steady-state solution is approached asymptotically with time.

A standard approach for the numerical solution of a blunt body problem is to first compute an inviscid solution using the Euler equations and then with the resulting pressure distribution compute a boundary layer solution. This approach is invalid for the present case because of the various types of boundary layer interactions caused by the shock impingement. The Navier-Stokes equations, however, are valid in such situations and have been chosen in the present study. In particular, the laminar, compressible form of the Navier-Stokes equations have been chosen.

Because of the possible existence of shock waves in the computational domain, a conservative form of the governing equations has been used.

The bow shock has been treated as a boundary of the computational domain across which the exact shock jump conditions (Rankine-Hugoniot relations) have been applied. This is the so-called "shock fitting" procedure. All interior detail such as shear layers, shock waves, supersonic jets, and the wall boundary layer are automatically captured. This is the so-called "shock capturing" procedure. The bow shock is strong enough to make an entirely captured solution impractical. On the other hand, fitting any additional shock layer detail (such as the transmitted shock) is generally too complicated (because of the transmitted shock-boundary layer interaction). Therefore, fitting the bow shock and capturing all shock layer detail seems to be a good approach for solving the problem at hand.

For the shock impingement problem, a distinct advantage for numerical methods exists over theoretical or experimental methods. Scale effects must be considered when extrapolating experimental data to flight conditions. Present theoretical methods require empirical inputs. However, numerical methods are able to predict flow fields for flight conditions without empirical inputs. This is a particular advantage for numerical methods when real gas effects enter the problem.

Descriptions of the governing equations, the numerical method, and the numerical results are given in the following sections of this report. The results consist of a series of blunt body infinite cylinder solutions and a three-dimensional wing leading edge shock impingement solution.

The present results are compared with theory and experimental results when possible.

II. GOVERNING EQUATIONS

A. Navier-Stokes Equations in Cylindrical Coordinates

The equations governing the flow of a compressible, viscous fluid in the absence of body forces and electromagnetic effects, and written in weak conservation-law form using three-dimensional cylindrical coordinates, are given by [56,57]

$$\frac{\partial \overline{U}}{\partial t} + \frac{\partial \overline{F}}{\partial r} + \frac{\partial \overline{G}}{\partial \theta} + \frac{\partial \overline{H}}{\partial z} + \overline{D} = 0 \qquad 2.1$$

where

$$\overline{U} = r \begin{bmatrix} \rho \\ \rho u_r \\ \rho u_\theta \\ \rho u_z \\ E \end{bmatrix} \qquad 2.2$$

$$\overline{F} = r \begin{bmatrix} \rho u_r \\ \rho u_r^2 + p - \tau_{rr} \\ \rho u_r u_\theta - \tau_{r\theta} \\ \rho u_r u_z - \tau_{rz} \\ (p+E)u_r - \tau_{rr}u_r - \tau_{r\theta}u_\theta - \tau_{rz}u_z + q_r \end{bmatrix} \qquad 2.3$$

$$\overline{G} = \begin{bmatrix} \rho u_\theta \\ \rho u_r u_\theta - \tau_{r\theta} \\ \rho u_\theta^2 + p - \tau_{\theta\theta} \\ \rho u_\theta u_z - \tau_{\theta z} \\ (p+E)u_\theta - \tau_{r\theta} u_r - \tau_{\theta\theta} u_\theta - \tau_{\theta z} u_z + q_\theta \end{bmatrix} \qquad 2.4$$

$$\overline{H} = r \begin{bmatrix} \rho u_z \\ \rho u_r u_z - \tau_{rz} \\ \rho u_\theta u_z - \tau_{\theta z} \\ \rho u_z^2 + \rho - \tau_{zz} \\ (p+E)u_z - \tau_{rz} u_r - \tau_{\theta z} u_\theta - \tau_{zz} u_z + q_z \end{bmatrix} \qquad 2.5$$

$$\overline{D} = \begin{bmatrix} 0 \\ -(\rho u_\theta^2 + p - \tau_{\theta\theta}) \\ \rho u_\theta u_r - \tau_{r\theta} \\ 0 \\ 0 \end{bmatrix} \qquad 2.6$$

$$E = \rho\left(e + \frac{u_r^2 + u_\theta^2 + u_z^2}{2}\right) \qquad 2.7$$

The Navier-Stokes expressions for the components of the stress tensor (τ_{ij}) and heat flux vector (q_i) have been used in this study and are given by [56,58]

$$\begin{aligned}
\tau_{rr} &= \mu e_{rr} - \frac{1}{3}\mu(e_{rr} + e_{\theta\theta} + e_{zz}) \\
\tau_{\theta\theta} &= \mu e_{\theta\theta} - \frac{1}{3}\mu(e_{rr} + e_{\theta\theta} + e_{zz}) \\
\tau_{zz} &= \mu e_{zz} - \frac{1}{3}\mu(e_{rr} + e_{\theta\theta} + e_{zz}) \\
\tau_{r\theta} &= \tau_{\theta r} = \mu e_{r\theta} \\
\tau_{rz} &= \tau_{zr} = \mu e_{rz} \\
\tau_{\theta z} &= \tau_{z\theta} = \mu e_{\theta z}
\end{aligned} \qquad 2.8$$

where

$$\begin{aligned}
e_{rr} &= 2\frac{\partial u_r}{\partial r} \\
e_{\theta\theta} &= \frac{2}{r}\frac{\partial u_\theta}{\partial \theta} + 2\frac{u_r}{r} \\
e_{zz} &= 2\frac{\partial u_z}{\partial z} \\
e_{r\theta} &= \frac{1}{r}\frac{\partial u_r}{\partial \theta} + \frac{\partial u_\theta}{\partial r} - \frac{u_\theta}{r} \\
e_{\theta z} &= \frac{\partial u_\theta}{\partial z} + \frac{1}{r}\frac{\partial u_z}{\partial \theta} \\
e_{rz} &= \frac{\partial u_z}{\partial r} + \frac{\partial u_r}{\partial z}
\end{aligned} \qquad 2.9$$

and

$$\begin{aligned}
q_r &= -k\frac{\partial T}{\partial r} \\
q_\theta &= -\frac{k}{r}\frac{\partial T}{\partial \theta} \\
q_z &= -k\frac{\partial T}{\partial z}
\end{aligned} \qquad 2.10$$

To complete this set of equations two perfect gas equations of state are used. In addition, Sutherland's equation and a constant Prandtl number assumption are used to compute coefficients of viscosity (μ) and thermal conductivity (k). The resulting equations are given by

$$p = \rho e(\gamma - 1) \tag{2.11}$$

$$p = \rho gRT \tag{2.12}$$

$$\mu = c_1 T^{3/2}/(c_2 + T) \tag{2.13}$$

$$k = c_p \mu/Pr \tag{2.14}$$

where for air in the perfect gas range the constants have the following values:

$$\begin{aligned} gR &= 287.024\ m^2/sec^2 - {}^oK \\ c_1 &= 1.2585 \times 10^{-8}\ N\text{-}sec/m^2 - {}^oK^{1/2} \\ c_2 &= 110.4\ {}^oK \\ c_p &= 1004.585\ m^2/sec^2 - {}^oK \\ Pr &= 0.72 \end{aligned} \tag{2.15}$$

B. Independent Variable Transformation

Equations 2.1 through 2.10 are transformed from the physical domain (r, θ, z, t) into the computational domain (ξ, η, ζ, τ) using the following independent variable transformation:

$$\begin{aligned}
\xi &= f\left(\frac{r_s - r}{r_s - r_b}\right) \\
\eta &= \theta \\
\zeta &= g(z) \\
\tau &= t
\end{aligned} \tag{2.16}$$

The derivatives associated with this transformation are given by

$$\begin{aligned}
\frac{\partial()}{\partial r} &= -\frac{1 -}{r_s - r_b} \frac{\partial f}{\partial x} \frac{\partial()}{\partial \xi} \\
\frac{\partial()}{\partial \theta} &= \frac{\partial f}{\partial x} r_{s_\theta} \frac{1 - x}{r_s - r_b} \frac{\partial()}{\partial \xi} + \frac{\partial()}{\partial \eta} \\
\frac{\partial()}{\partial z} &= \frac{\partial f}{\partial x} r_{s_z} \frac{1 - x}{r_s - r_b} \frac{\partial()}{\partial \xi} + \frac{\partial g}{\partial z} \frac{\partial()}{\partial \zeta} \\
\frac{\partial()}{\partial t} &= \frac{\partial f}{\partial x} r_{s_t} \frac{1 - x}{r_s - r_b} \frac{\partial()}{\partial \xi} + \frac{\partial()}{\partial \tau}
\end{aligned} \tag{2.17}$$

where r_s is the bow shock radius, r_b is the body radius, r_{s_θ} and r_{s_z} are the shock slopes in the θ- and z-directions, respectively, r_{s_t} is the radial shock velocity, and x is defined by

$$x = \frac{r_s - r}{r_s - r_b} \tag{2.18}$$

This transformation maps the z-plane between the bow shock and the blunt body into a rectangular region, stretches the radial distribution of grid points according to the function f, and stretches the axial distribution of grid points according to the function g.

The function f chosen for all cases considered here is given by [59]

$$f(x) \begin{cases} = \frac{1}{c} \ln\left(\frac{\beta + x}{\beta - x}\right) & 1 < \beta < \infty \\ = x & \beta = 0 \end{cases} \qquad 2.19$$

where

$$c = \ln\left(\frac{\beta + 1}{\beta - 1}\right) \qquad 2.20$$

The first and second derivatives of the radial stretching function (f) are given by:

$$\frac{\partial f}{\partial x} = \frac{2\beta/c}{(\beta + x)(\beta - x)} \qquad 2.21$$

$$\frac{\partial^2 f}{\partial x^2} = \frac{1}{c}\left[\frac{1}{(\beta - x)^2} - \frac{1}{(\beta + x)^2}\right] \qquad 2.22$$

Equation 2.19 refines the grid near the body and thus permits better boundary layer resolution. Figure 8 is a plot of the f stretching function for various values of β which controls the amount of refinement. The practical range for β is between 1 and 2 with smaller values giving larger amounts of refinement. When β is set equal to zero no radial stretching of the mesh occurs.

The function g chosen for all cases considered here is simply that of a linear distribution (no stretching of the mesh) and is given by

$$g(z) = z \qquad 2.23$$

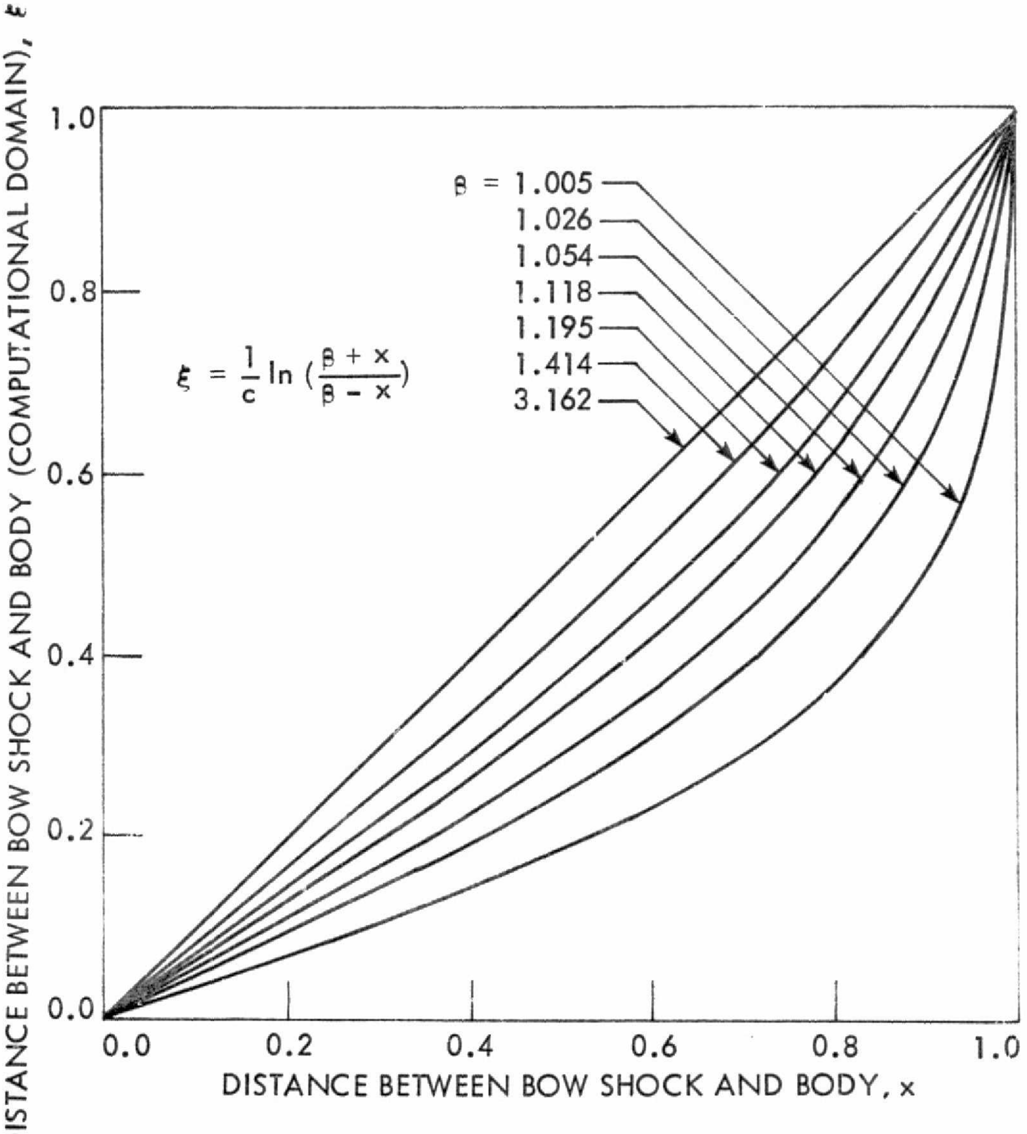

Figure 8. f stretching function distribution.

$$\frac{\partial g}{\partial z} = 1.0 \qquad 2.24$$

$$\frac{\partial^2 g}{\partial z^2} = 0.0 \qquad 2.25$$

The physical domain of the problem is shown in Figure 9a without an impinging shock for clarity. The computational domain which results after the independent variable transformation has been applied is shown in Figure 9b. The grid distribution appearing in a typical θ-plane in the physical domain is shown in Figure 10a. The grid distribution in a typical η-plane, which is the computational counterpart of the physical θ-plane, is shown in Figure 10b. These two figures illustrate what the independent variable transformation does to the physical domain. No matter how the physical domain changes or alters its shape during the computation, the computational domain retains its rectangular box shape with uniform mesh spacing throughout.

C. Governing Equations in Computational Domain

The final form of the governing equations after the independent variable transformation has been applied is given by

$$\frac{\partial U}{\partial \tau} + \frac{\partial F}{\partial \xi} + \frac{\partial G}{\partial \eta} + \frac{\partial H}{\partial \zeta} + D = 0 \qquad 2.26$$

where

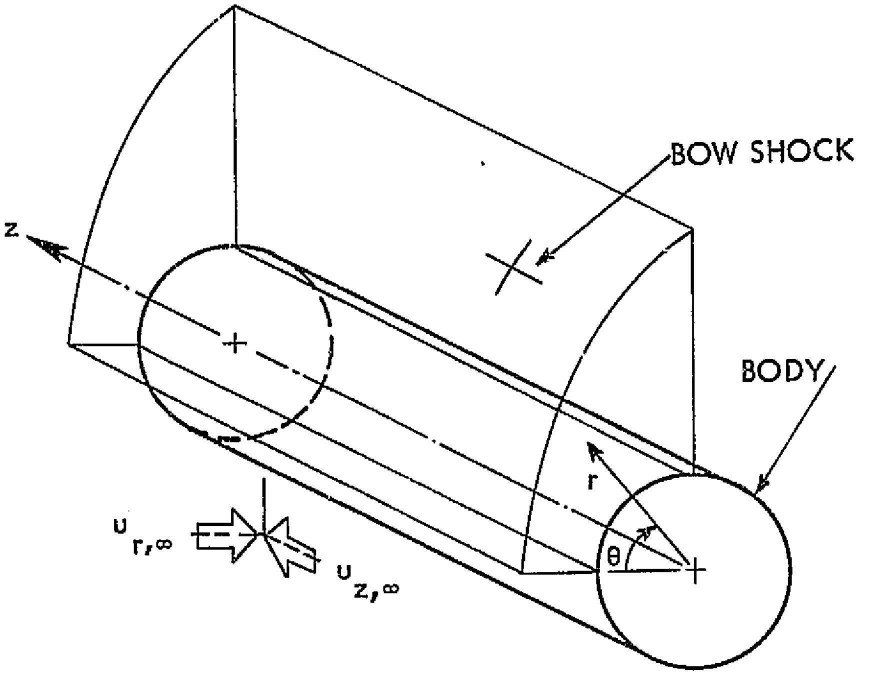

a. PHYSICAL DOMAIN

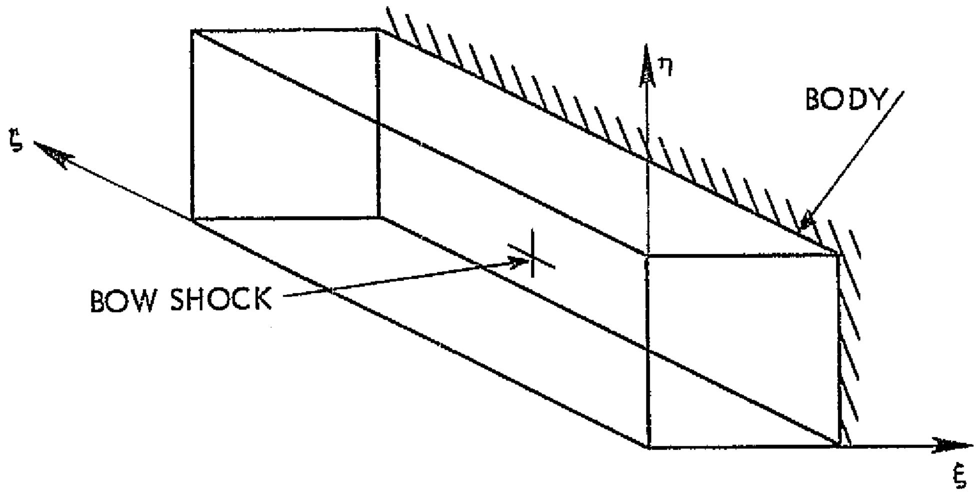

b. COMPUTATIONAL DOMAIN

Figure 9. Physical and computational domains.

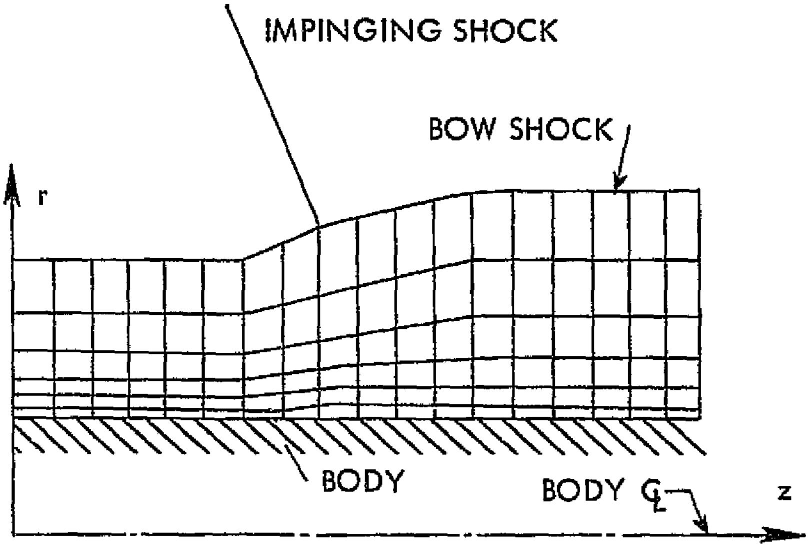

a. TYPICAL θ-PLANE (PHYSICAL DOMAIN)

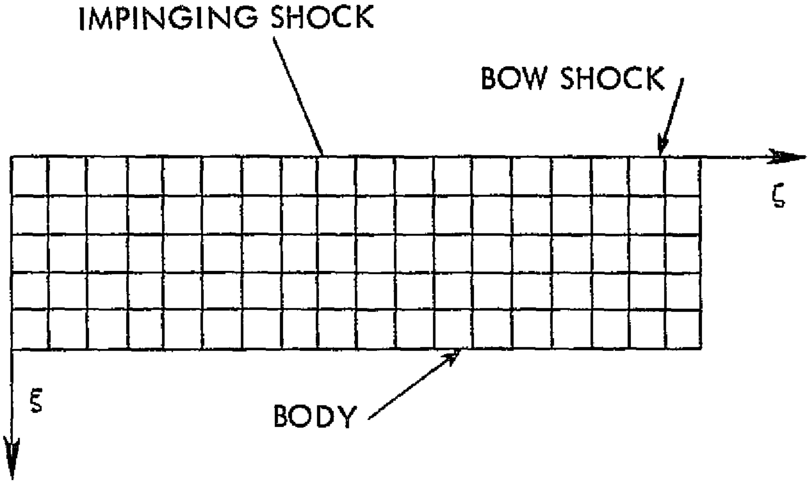

b. TYPICAL η-PLANE (COMPUTATIONAL DOMAIN)

Figure 10. A planar comparison of the physical and computational domains.

$$U = r(r_s - r_b) \begin{bmatrix} \rho \\ \rho u_r \\ \rho u_\theta \\ \rho u_z \\ E \end{bmatrix} \qquad 2.27$$

$$F = -r \frac{\partial f}{\partial x} \begin{bmatrix} \rho u_r \\ \rho u_r^2 + p - \tau_{\xi\xi} \\ \rho u_r u_\theta - \tau_{\xi\eta} \\ \rho u_r u_z - \tau_{\xi\zeta} \\ (p+E)u_r - \tau_{\xi\xi}u_r - \tau_{\xi\eta}u_\theta - \tau_{\xi\zeta}u_z + q_\xi \end{bmatrix} \qquad 2.28$$

$$+ \frac{\partial f}{\partial x} \frac{1-x}{r_s - r_b} \left(r_{s_t} U + r_{s_\theta} G + r_{s_z} \frac{1}{(\partial g/\partial z)} H \right)$$

$$G = (r_s - r_b) \begin{bmatrix} \rho u_\theta \\ \rho u_r u_\theta - \tau_{\eta\xi} \\ \rho u_\theta^2 + p - \tau_{\eta\eta} \\ \rho u_\theta u_z - \tau_{\eta\zeta} \\ (p+E)u_\theta - \tau_{\eta\xi}u_r - \tau_{\eta\eta}u_\theta - \tau_{\eta\zeta}u_z + q_\eta \end{bmatrix} \qquad 2.29$$

$$H = r(r_s - r_b)\frac{\partial g}{\partial z}\begin{bmatrix} \rho u_z \\ \rho u_z u_r - \tau_{\zeta\xi} \\ \rho u_z u_\theta - \tau_{\zeta\eta} \\ \rho u_z^2 + p - \tau_{\zeta\zeta} \\ (p+E)u_z - \tau_{\zeta\xi}u_z - \tau_{\zeta\eta}u_\theta - \tau_{\zeta\zeta}u_z + q_\zeta \end{bmatrix} \qquad 2.30$$

$$D = (r_s - r_b)\begin{bmatrix} 0 \\ -(\rho u_\theta^2 + p - \tau_{\eta\eta}) \\ \rho u_\theta u_r - \tau_{\xi\eta} \\ 0 \\ 0 \end{bmatrix} - \frac{\dfrac{\partial^2 f}{\partial x^2}}{\left(\dfrac{\partial f}{\partial x}\right)^2} F - \frac{\dfrac{\partial^2 g}{\partial z^2}}{\left(\dfrac{\partial g}{\partial z}\right)^2} H \qquad 2.31$$

and

$$\begin{aligned}
\tau_{\xi\xi} &= \mu e_{\xi\xi} - \frac{1}{3}\mu(e_{\xi\xi} + e_{\eta\eta} + e_{\zeta\zeta}) \\
\tau_{\eta\eta} &= \mu e_{\eta\eta} - \frac{1}{3}\mu(e_{\xi\xi} + e_{\eta\eta} + e_{\zeta\zeta}) \\
\tau_{\zeta\zeta} &= \mu e_{\zeta\zeta} - \frac{1}{3}\mu(e_{\xi\xi} + e_{\eta\eta} + e_{\zeta\zeta}) \\
\tau_{\xi\eta} &= \tau_{\eta\xi} = \mu e_{\xi\eta} \\
\tau_{\xi\zeta} &= \tau_{\zeta\xi} = \mu e_{\xi\zeta} \\
\tau_{\eta\zeta} &= \tau_{\zeta\eta} = \mu e_{\eta\zeta}
\end{aligned} \qquad 2.32$$

$$\begin{aligned}
e_{\xi\xi} &= -\frac{2}{r_s - r_b}\frac{\partial f}{\partial x}\frac{\partial u_r}{\partial \xi} \\
e_{\eta\eta} &= \frac{2}{r}\left[\frac{\partial u_\theta}{\partial \eta} + (1 - x)\frac{r_{s_\theta}}{r_s - r_b}\frac{\partial f}{\partial x}\frac{\partial u_\theta}{\partial \xi} + u_r\right] \\
e_{\zeta\zeta} &= 2\left[\frac{\partial g}{\partial z}\frac{\partial u_z}{\partial \zeta} + (1 - x)\frac{r_{s_z}}{r_s - r_b}\frac{\partial f}{\partial x}\frac{\partial u_z}{\partial \xi}\right] \\
e_{\xi\eta} &= \frac{1}{r}\left[\frac{\partial u_r}{\partial \eta} + (1 - x)\frac{r_{s_\theta}}{r_s - r_b}\frac{\partial f}{\partial x}\frac{\partial u_r}{\partial \xi} - u_\theta\right] \\
&\qquad - \frac{1}{r_s - r_b}\frac{\partial f}{\partial x}\frac{\partial u_\theta}{\partial \xi} \\
e_{\eta\zeta} &= \frac{\partial g}{\partial z}\frac{\partial u_\theta}{\partial \zeta} + (1 - x)\frac{r_{s_z}}{r_s - r_b}\frac{\partial f}{\partial x}\frac{\partial u_\theta}{\partial \xi} \\
&\qquad + \frac{1}{r}\left[\frac{\partial u_z}{\partial \eta} + (1 - x)\frac{r_{s_\theta}}{r_s - r_b}\frac{\partial f}{\partial x}\frac{\partial u_z}{\partial \xi}\right] \\
e_{\xi\zeta} &= -\frac{1}{r_s - r_b}\frac{\partial f}{\partial x}\frac{\partial u_z}{\partial \xi} + \frac{\partial g}{\partial z}\frac{\partial u_r}{\partial \zeta} + (1 - x)\frac{r_{s_z}}{r_s - r_b}\frac{\partial f}{\partial x}\frac{\partial u_r}{\partial \xi}
\end{aligned} \tag{2.33}$$

$$\begin{aligned}
q_\xi &= \frac{k}{r_s - r_b}\frac{\partial f}{\partial x}\frac{\partial T}{\partial \xi} \\
q_\eta &= -k\left[\frac{\partial T}{\partial \eta} + (1 - x)\frac{r_{s_\theta}}{r_s - r_b}\frac{\partial f}{\partial x}\frac{\partial T}{\partial \xi}\right] \\
q_\zeta &= -k\left[\frac{\partial g}{\partial z}\frac{\partial T}{\partial \zeta} + (1 - x)\frac{r_{s_z}}{r_s - r_b}\frac{\partial f}{\partial x}\frac{\partial T}{\partial \xi}\right]
\end{aligned} \tag{2.34}$$

In these equations the radial position (r) is given by

$$r = r_s - f^{-1}(\xi)\,(r_s - r_b) \tag{2.35}$$

where the function $f^{-1}(\xi)$ represents the inverse of f. For the present f (Equation 2.19) the inverse is given by

$$f^{-1}(\xi) = \beta \frac{e^{cx} - 1}{e^{cx} + 1} \qquad 2.36$$

In addition Equations 2.7 and 2.11 through 2.15 must be included and are unaltered by the transformation.

Equations 2.26 through 2.34 represent the full three-dimensional Navier-Stokes equations valid for compressible, laminar, time-dependent flows. These equations are solved by a numerical finite-difference procedure which is presented in the next section.

III. NUMERICAL METHOD

A. Finite-Difference Scheme

Equation 2.25 is solved by MacCormack's explicit finite-difference method [60], which is composed of the predictor-corrector sequence given in Equations 3.1 and 3.2.

predictor step:

$$U^{\overline{n+1}}_{i,j,k} = U^{n}_{i,j,k} - \frac{\Delta\tau}{\Delta\xi}\left(F^{n}_{i+1,j,k} - F^{n}_{i,j,k}\right) - \frac{\Delta\tau}{\Delta\eta}\left(G^{n}_{i,j+1,k} - G^{n}_{i,j,k}\right)$$

$$- \frac{\Delta\tau}{\Delta\zeta}\left(H^{n}_{i,j,k+1} - H^{n}_{i,j,k}\right) - \Delta\tau D^{n}_{i,j,k} \qquad 3.1$$

corrector step:

$$U^{n+1}_{i,j,k} = \frac{1}{2}\left[U^{n}_{i,j,k} + U^{\overline{n+1}}_{i,j,k} - \frac{\Delta\tau}{\Delta\xi}\left(F^{\overline{n+1}}_{i,j,k} - F^{\overline{n+1}}_{i-1,j,k}\right)\right. \qquad 3.2$$

$$\left. - \frac{\Delta\tau}{\Delta\eta}\left(G^{\overline{n+1}}_{i,j,k} - G^{\overline{n+1}}_{i,j-1,k}\right) - \frac{\Delta\tau}{\Delta\zeta}\left(H^{\overline{n+1}}_{i,j,k} - H^{\overline{n+1}}_{i,j,k-1}\right) - \Delta\tau D^{\overline{n+1}}_{i,j,k}\right]$$

where $F^{n}_{i,j,k} = F\left(U^{n}_{i,j,k}\right)$, $F^{\overline{n+1}}_{i,j,k} = F\left(U^{\overline{n+1}}_{i,j,k}\right)$, etc. The i,j,k subscripts and the n superscript correspond to the discretized position in the finite-difference mesh in the ξ-, η-, ζ-, and τ-directions such that $\xi = i\Delta\xi$, $\eta = j\Delta\eta$, $\zeta = k\Delta\zeta$, and $\tau = n\Delta\tau$. A bar above the n superscript indicates a predicted value. Forward differences are used in the predictor step to approximate the $\partial F/\partial\xi$, $\partial G/\partial\eta$, and $\partial H/\partial\zeta$ derivatives while backward differences are used for these terms in the corrector step. In the predictor step backward differences are used to approximate the shear stress and heat flux derivatives appearing in the F, G, H, and D components while in the corrector step forward differences are used. This differencing procedure maintains second-order accuracy in both space and time [61].

The computational module for MacCormack's method in three spacial dimensions is shown in Figure 11. Both the predictor and corrector step modules are shown. The symbol o is used to indicate mesh points at which values for F, G, H, or D are required and are used in differences approximating the $\partial F/\partial \xi$, $\partial G/\partial \eta$, and $\partial H/\partial \zeta$ derivatives. The symbol + is used to indicate mesh points requiring values for u_r, u_θ, u_z, or T and are used in differences approximating the shear stress and heat flux derivatives. Note that in both the predictor step (Equation 3.1 and Figure 11a) and the corrector step (Equation 3.2 and Figure 11b) information from only three k-planes is required $(k-1, k, k+1)$. In the predictor step (Equation 3.1) the subscripts k and $k+1$ appear explicitly while the subscript $k-1$ is implicitly imbedded in the shear stress and heat flux derivatives. In the corrector step (Equation 3.2) the subscripts $k-1$ and k appear explicitly while the subscript $k+1$ is implicitly imbedded in the shear stress and heat flux derivatives.

For the present study MacCormack's method is applied to the finite-difference mesh in four steps: 1) partial-predictor step, 2) completor-predictor step, 3) partial-corrector step, and 4) completor-corrector step. These steps are shown in Equations 3.3-3.6.

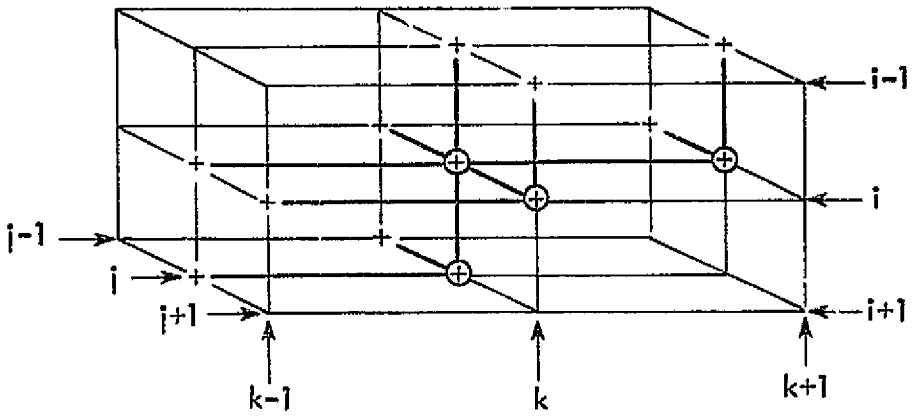

a. PREDICTOR STEP

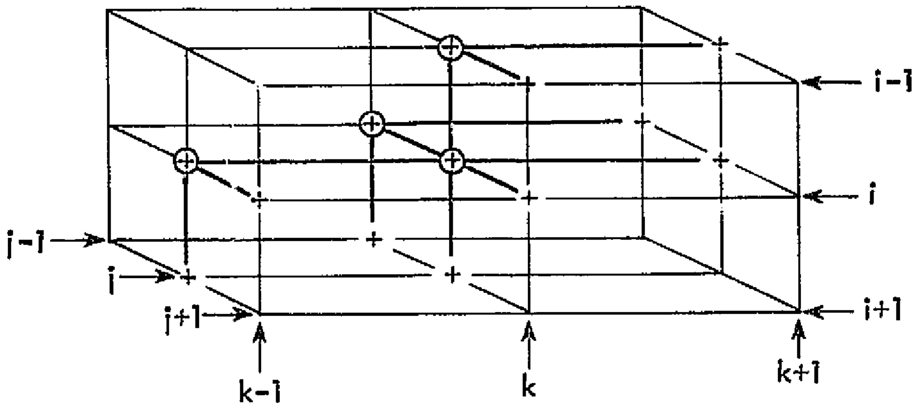

b. CORRECTOR STEP

Figure 11. Computational module for MacCormack's method in three spacial directions.

partial-predictor step:

$$U^{pp}_{i,j,k} = U^{n}_{i,j,k} - \frac{\Delta\tau}{\Delta\xi}\left(F^{n}_{i+1,j,k} - F^{n}_{i,j,k}\right) - \frac{\Delta\tau}{\Delta\eta}\left(G^{n}_{i,j+1,k} - G^{n}_{i,j,k}\right)$$

$$+ \frac{\Delta\tau}{\Delta\zeta} H^{n}_{i,j,k} - \Delta\tau D^{n}_{i,j,k} \qquad 3.3$$

completor-predictor step:

$$U^{\overline{n+1}}_{i,j,k} = U^{pp}_{i,j,k} - \frac{\Delta\tau}{\Delta\zeta} H^{n}_{i,j,k+1} \qquad 3.4$$

partial-corrector step:

$$U^{pc}_{i,j,k} = U^{n}_{i,j,k} + \frac{\Delta\tau}{\Delta\zeta} H^{\overline{n+1}}_{i,j,k-1} \qquad 3.5$$

completor-corrector step:

$$U^{\overline{n+1}}_{i,j,k} = \frac{1}{2}\Big[U^{pc}_{i,j,k} + U^{\overline{n+1}}_{i,j,k} - \frac{\Delta\tau}{\Delta\xi}\left(F^{\overline{n+1}}_{i,j,k} - F^{\overline{n+1}}_{i-1,j,k}\right)$$

$$- \frac{\Delta\tau}{\Delta\eta}\left(G^{\overline{n+1}}_{i,j,k} - G^{\overline{n+1}}_{i,j-1,k}\right) - \frac{\Delta\tau}{\Delta\zeta} H^{\overline{n+1}}_{i,j,k} - \Delta\tau D^{\overline{n+1}}_{i,j,k}\Big] \qquad 3.6$$

where the pp superscript designates the partial-predictor step result and the pc superscript designates the partial-corrector step result. All other notation is identical with the notation used in the standard MacCormack method. Note that when steps 1 and 2 (Equations 3.3 and 3.4) are combined the standard MacCormack predictor step (Equation 3.1) is obtained and that when steps 3 and 4 (Equations 3.5 and 3.6) are combined the standard MacCormack corrector step (Equation 3.2) is obtained.

After each completed predictor or corrector step the U vector

$$U = r(r_s - r_b)\begin{bmatrix}\rho \\ \rho u_r \\ \rho u_\theta \\ \rho u_z \\ E\end{bmatrix} = \begin{bmatrix}U_1 \\ U_2 \\ U_3 \\ U_4 \\ U_5\end{bmatrix} \qquad 3.7$$

is decoded to obtain the primitive variables ($\rho, u_r, u_\theta, u_z, e$) in the following manner:

$$\begin{aligned} u_r &= U_2/U_1 \\ u_\theta &= U_3/U_1 \\ u_z &= U_4/U_1 \\ e &= U_5/U_1 - (u_r^2 + u_\theta^2 + u_z^2)/2 \\ \rho &= U_1/r(r_s - r_b) \end{aligned} \qquad 3.8$$

In all four steps shown in Equations 3.3 - 3.6 information from only two k-planes is required in any single step. This aspect of the modified MacCormack method allows for a unique, storage-saving sweeping procedure. This procedure is described in detail in the next section.

B. Application of the Finite-Difference Scheme (Sweeping Procedure)

MacCormack's method is usually coded to compute predicted values at each grid point over the entire finite-difference mesh before the corrector step calculation is initiated. This requires storage for both the predicted and corrected solution arrays during the computational process. In addition, many codes store other intermediate result arrays over the entire finite-difference mesh. For two-dimensional problems this extra storage may not be a critical restriction. For three-dimensional problems these extra arrays may require large quantities of bulk storage causing significant penalties in program efficiency.

The storage restriction associated with MacCormack's method for three-dimensional problems has been to a large extent alleviated in the present study. A special technique for sweeping through the finite-difference mesh has been developed which requires storage for only a single three-dimensional solution array. Besides the single three-dimentional solution array several smaller two-dimensional arrays (k-planes) are required to store intermediate results. This special sweeping procedure is shown in Figure 12 where it is displayed in five separate diagrams (steps 1 - 5). For this presentation it is assumed that the computer memory is divided into two types: 1) a larger, slower access large core memory (LCM), and 2) a smaller, faster access small core memory (SCM). Data exchange between small and large core memory is efficiently achieved by using block transfer. This is the basic architecture of many computing systems such as the CDC 7600, CDC STAR and Burroughs ILLIAC IV. The three-dimensional solution array resides in LCM and appears at the top of each of the diagrams in Figure 12. The intermediate result arrays reside in SCM and appear below the three-

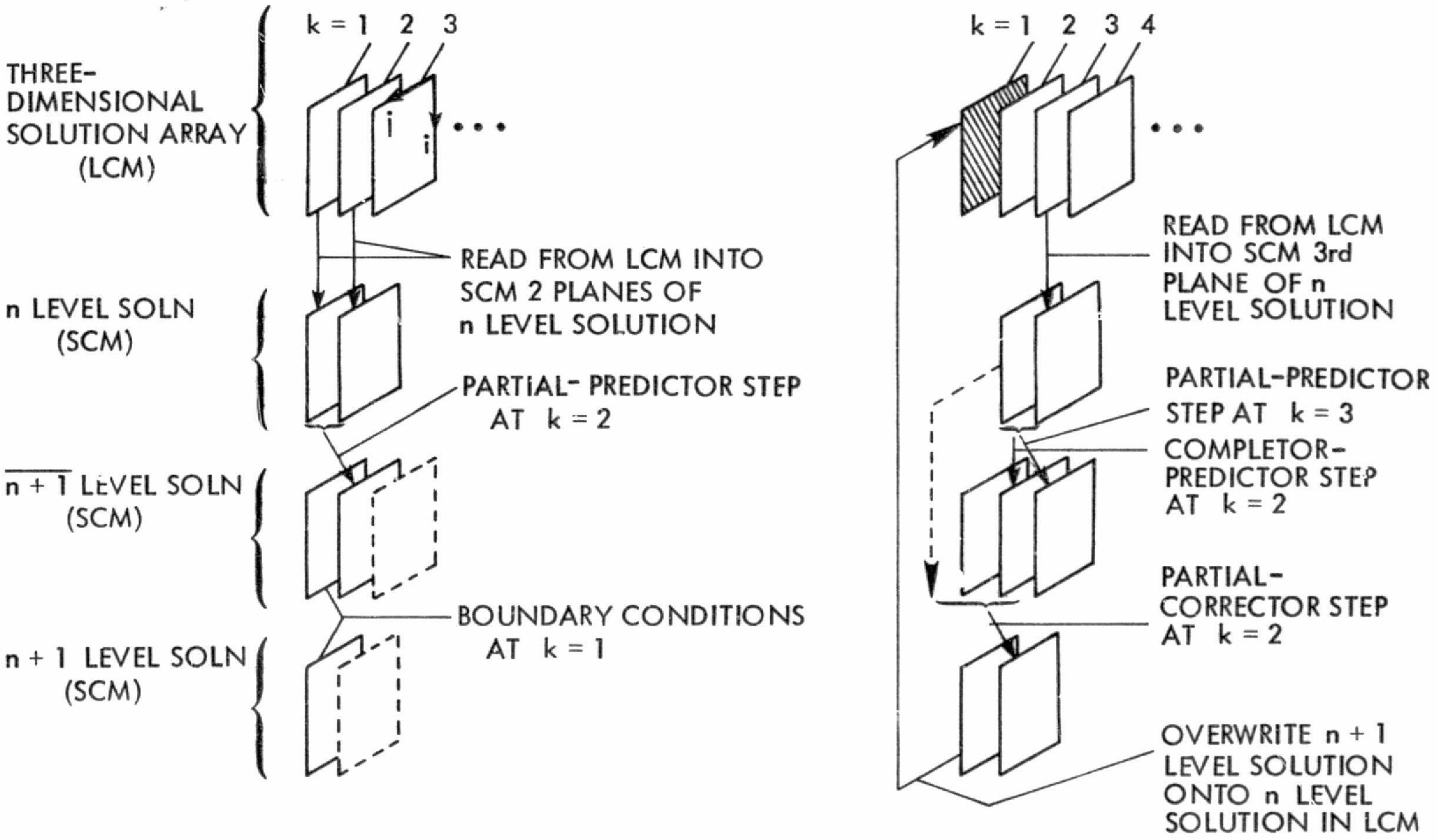

a) STEP 1: START UP

b) STEP 2: START UP

Figure 12. Diagram of the three-dimensional sweeping procedure.

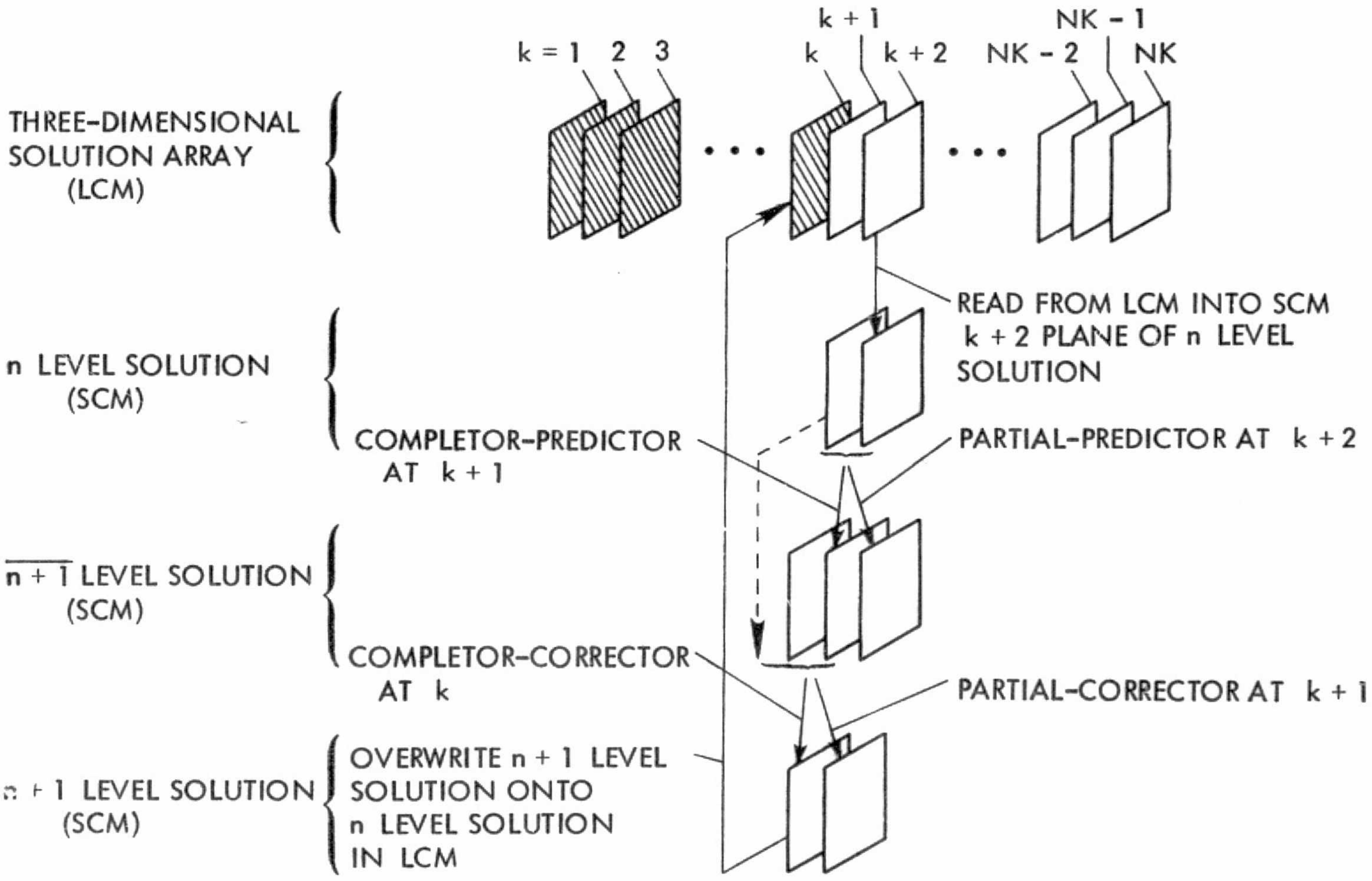

c) STEP 3: THE GENERAL kth PLANE

Figure 12. (Continued).

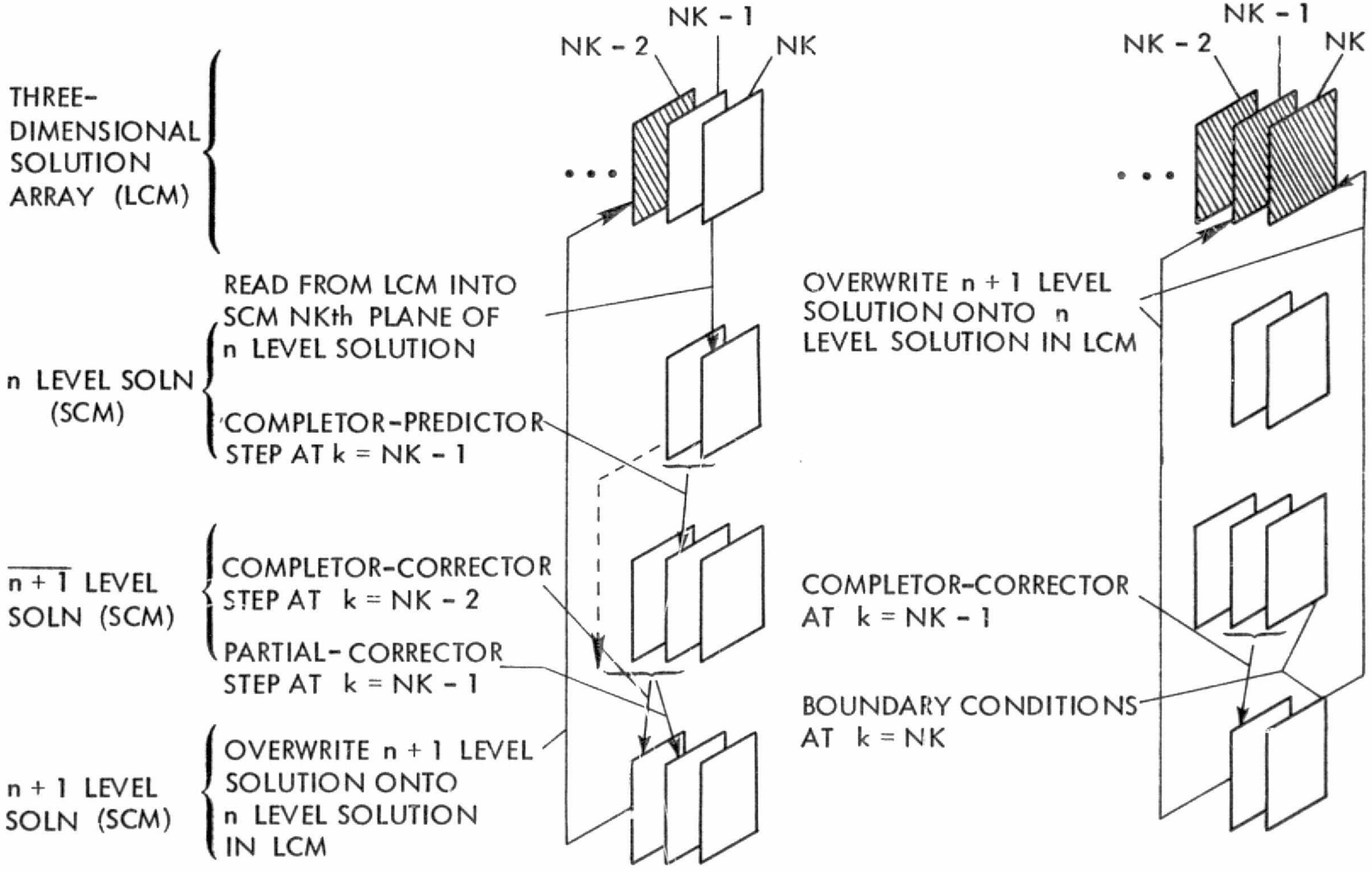

d) STEP 4: COMPLETION OF A SWEEP

e) STEP 5: COMPLETION OF A SWEEP

Figure 12. (Continued).

dimensional solution array in each of the diagrams. These arrays are indicated as planes in Figure 12 with operations between them being indicated by arrows. Each plane represents a set of five arrays, one array for each of the primitive variables (ρ, u_r, u_θ, u_z, e). The basic sweeping direction is the k-direction (z-direction).

The first step of the sweeping procedure is shown in Figure 12a. First, two planes of the n level solution (a total of ten arrays) are read into SCM from the $k = 1$ and 2 planes of LCM. From the data in these two planes the $k = 2$ plane of partial-predictor values is computed. A secondary sweeping procedure is used to obtain these partial-predictor values. This sweeping procedure starts at the bow shock ($i=1$) and sweeps through the k-plane of mesh points toward the body ($i=NI$). The purpose of this planar sweeping procedure is to reduce the number of k-plane intermediate result arrays. Boundary conditions for the $\overline{n+1}$ and the $n+1$ level solutions at $k = 1$ are also applied in this step (see Figure 12a).

The next step continues the start up procedure and is shown in Figure 12b. Since the n level plane at $k = 1$ is no longer needed, it is overwritten with the n level plane at $k = 2$. Next, a new n level plane from LCM at $k = 3$ is read into SCM, keeping the number of n level planes in SCM at two. A plane of partial-predictor values at $k = 3$ and a plane of completor-predictor values at $k = 2$ can now be computed. The completor-predictor step at $k = 2$ uses the partial-predictor values which were computed and saved from the previous plane at $k = 2$. Then, using the $k = 1$ and 2 planes of $\overline{n+1}$ level values and the $k = 2$ plane of n level values, a plane of partial-corrector values at $k = 2$ is computed.

Finally the $n+1$ level plane at $k=1$ is stored in the three-dimensional solution array by overwriting the $k=1$ plane of the n level solution. Planes containing the $n+1$ level solution in the three-dimensional solution array in the diagrams of Figure 12 are shaded while n level planes remain unshaded.

A recursive process for the general kth plane has the following steps (see Figure 12c): 1) read the $k+2$ plane of the n level solution from LCM into SCM, 2) compute a plane of partial-predictor values at $k+2$, 3) compute a plane of completor-predictor values at $k+1$, 4) compute a plane of partial-corrector values at $k+1$, 5) compute a plane of completor-corrector values at k, and 6) store the kth plane of the $n+1$ level solution in the three-dimensional solution array by overwriting the kth plane of n level solution. The recursive process begins at $k=2$ and continues until $k=NK-3$ where NK represents the maximum value of k. Note that by constantly overwriting unnecessary planes of storage the maximum number of intermediate result planes in SCM never exceeds seven; two for the n level solution, three for the $\overline{n+1}$ level solution and two for the $n+1$ level solution.

The treatment for the $NK-2$ plane is shown in Figure 12d. The steps involved are identical to those described in Figure 12c, except that since this is the last value of k for which a plane of predicted values is to be calculated no partial-predictor values are computed.

The final step of the sweeping procedure is shown in Figure 12e. First a boundary condition is applied to the predicted values at NK creating enough information to compute the completor-corrector values at $NK-1$. The final plane of corrected values is then obtained from the same boundary condition which was applied to the predicted values. Then both $n+1$ level planes at NK - 1 and NK are stored in the three-dimensional solution array by overwriting the final two planes of the n level solution. The $n+1$ level solution is now completely stored in the three-dimensional solution array. This completes one sweep of the sweeping procedure as well as a single time step.

The final solution is obtained in a manner typical of the time-dependent approach. Using the previously outlined procedure, the computation is advanced in time from the initial conditions until the solution is changing by a sufficiently small amount. At this point the solution is said to have reached "steady state."

C. Shock Jump Conditions

The bow shock wave is a boundary of the computational domain across which the exact shock jump conditions are applied (Rankine-Hugoniot equations). Exact treatment of a shock wave by such a procedure is called "shock fitting." Because the bow shock position is not known a priori, a procedure for determining its position is incorporated with the application of the shock jump conditions. The three-dimensional shock fitting procedure used in the present study was developed from the two-dimensional procedure used by Tannehill et al. [54]. It is similar to the method used by Daywitt and Anderson [47] (two-dimensional, time-marching problems) and the methods used by Thomas et al. [62] and Kutler et al. [63] (three-dimensional, steady, space-marching problems).

The three-dimensional shock jump conditions used in the present study are applied only one plane at a time in order to be compatible with the sweeping procedure described in the last section. The solution variables at $i = 1$ and along j $(1 \leq j \leq NJ)$ for all completor-predictor and completor-corrector planes are computed from the shock jump conditions. Shock jump conditions as well as other boundary conditions are not required for the partial-predictor or the partial-corrector steps. A detailed description of the three-dimensional shock jump procedure for a perfect gas is now presented. A similar presentation involving a real gas in equilibrium is presented in Appendix A.

The three-dimensional shock jump procedure starts by computing the $\overline{n+1}$ values for the bow shock radius from the Euler predictor equation given by

$$r_{s_{j,k}}^{\overline{n+1}} = r_{s_{j,k}}^{n} + \Delta\tau \left(r_{s_t}\right)_{j,k}^{n} \tag{3.9}$$

where r_s is the shock radius, r_{s_t} the radial shock velocity and $\Delta\tau$ the time increment. Equation 3.9 is used to compute the predicted values for the shock radius everywhere except on the boundaries where the following boundary conditions are used:

$$\begin{aligned}
r_{s_{1,k}} &= r_{s_{2,k}} \\
r_{s_{NJ,k}} &= 3\left(r_{s_{NJ-1,k}} - r_{s_{NJ-2,k}}\right) + r_{s_{NJ-3,k}} \\
r_{s_{j,1}}^{n} &= r_{s_{j,1}}^{1} \qquad \text{(fixed for all time)} \\
r_{s_{j,NK}} &= r_{s_{j,NK-1}}
\end{aligned} \tag{3.10}$$

The next step involves the calculation of the pressure immediately behind the bow shock ($p^n_{1,j,k} \equiv p_2$). This is accomplished by using the partial-predictor, completor-predictor combination given in Equations 3.3 and 3.4. The resulting predicted values are decoded into the primitive variables (ρ, u_r, u_θ, u_z, e) by using Equations 3.7 and 3.8. The pressure is then obtained from the equation of state (Equation 2.11).

Because Equation 3.3 is applied on a boundary (i=1) the backward differences used to approximate some of the derivatives in the shear stress and heat flux terms require unobtainable information at i - 1. To correct this situation forward differences are used wherever backward differences are not valid. The use of forward differences in place of backward differences reduces the method's second-order accuracy in the vicinity of the bow shock but does not harm the overall solution accuracy.

The shock slopes (r_{s_θ} and r_{s_z}) at the $\overline{n+1}$ level are calculated next by using the following central difference formulas

$$\left(r_{s_\theta}\right)^{\overline{n+1}}_{j,k} = \left(r_{s_{j+1,k}}^{\overline{n+1}} - r_{s_{j-1,k}}^{\overline{n+1}}\right)/2\Delta\theta \qquad 3.11$$

$$\left(r_{s_z}\right)^{\overline{n+1}}_{j,k} = \left(r_{s_{j,k+1}}^{\overline{n+1}} - r_{s_{j,k-1}}^{\overline{n+1}}\right)/2\Delta z \qquad 3.12$$

where $\Delta\theta$ and Δz are the physical grid increments in the θ- and z-directions, respectively. Values for the shock slopes on the boundaries which cannot be computed from either Equation 3.11 or 3.12 are obtained by

$$\begin{aligned}
\left(r_{s_\theta}\right)_{1,k} &= \left(r_{s_\theta}\right)_{2,k} \\
\left(r_{s_\theta}\right)_{NJ,k} &= 3\left[\left(r_{s_\theta}\right)_{NJ-1,k} - \left(r_{s_\theta}\right)_{NJ-2,k}\right] + \left(r_{s_\theta}\right)_{NJ-3,k} \\
\left(r_{s_z}\right)_{j,1} &= 0.0 \\
\left(r_{s_z}\right)_{j,NK} &= \left(r_{s_z}\right)_{j,NK-1}
\end{aligned} \qquad 3.13$$

The primitive flow field variables obtained from the modified MacCormack's scheme applied at $i = 1$ are now recomputed from the pressure (p_2), the shock slopes (r_{s_θ} and r_{s_z}) and the shock jump conditions. These conditions are derived from the Rankine-Hugoniot equations and shock geometry considerations in Appendix B and are given by

$$\rho_2 = \rho_\infty \frac{\frac{\gamma-1}{\gamma+1} + \frac{p_2}{p_\infty}}{\frac{p_2}{p_\infty}\frac{\gamma-1}{\gamma+1} + 1} \qquad 3.14$$

$$V_N = \sqrt{\frac{(\gamma+1)}{2}\frac{p_\infty}{\rho_\infty}\left(\frac{\gamma-1}{\gamma+1} + \frac{p_2}{p_\infty}\right)} \qquad 3.15$$

$$u_{r,2} = u_{r,\infty} - \frac{p_\infty - p_2}{\rho_\infty V_N}\,\frac{1}{\sqrt{1 + \left(r_{s_\theta}/r_s\right)^2 + r_{s_z}^2}} \qquad 3.16$$

$$u_{\theta,2} = u_{\theta,\infty} - \frac{p_\infty - p_2}{\rho_\infty V_N} \frac{-r_{s_\theta}/r_s}{\sqrt{1 + \left(r_{s_\theta}/r_s\right)^2 + r_{s_z}^2}} \tag{3.17}$$

$$u_{z,2} = u_{z,\infty} - \frac{p_\infty - p_2}{\rho_\infty V_N} \frac{-r_{s_z}}{\sqrt{1 + \left(r_{s_\theta}/r_s\right)^2 + r_{s_z}^2}} \tag{3.18}$$

$$\begin{aligned} r_{s_t} = {} & V_N \sqrt{1 + \left(r_{s_\theta}/r_s\right)^2 + r_{s_z}^2} + u_{r,2} \\ & - u_{\theta,2}\left(r_{s_\theta}/r_s\right) - u_{z,2}\, r_{s_z} \end{aligned} \tag{3.19}$$

where the 2 subscript indicates conditions just downstream of the bow shock (1,j,k) at the $\overline{n+1}$ level. V_N is the component of freestream velocity normal to the bow shock and measured in a coordinate system fixed with respect to the bow shock (positive inward). All r_s, r_{s_θ}, r_{s_z} and r_{s_t} values are at the (j,k) position in space and the $\overline{n+1}$ level in time. The quantities p_∞, ρ_∞, $u_{r,\infty}$, $u_{\theta,\infty}$, and $u_{z,\infty}$ (infinity conditions) are either freestream conditions or flow conditions downstream of the planar impinging shock.

Before Equations 3.14 - 3.19 can be applied, a test must be made to determine which set of infinity conditions are to be used. This test must be performed for each grid point at which shock jump conditions are applied. First, the position of the intersection line between the planar impinging shock and bow shock waves must be found.

The impinging shock is a fixed plane in the physical domain, and is expressed analytically as follows

$$r_{p_{j,k}} = \left[-\frac{x_{int}}{z_{int}} \Delta z(k-1) + x_{int} \right] \frac{1}{\cos[\Delta\theta(j-3/2)]} \qquad 3.20$$

where r_p is the planar impinging shock radius and x_{int} and z_{int} are the r- and z-intercepts, respectively, of the planar impinging shock in the $\theta = 0^\circ$ plane. Of course, the bow shock cannot be described analytically. Therefore, the description given by the two-dimensional array of values, $r_{s_{j,k}}$, must be used. For a given value of j the intersection line position is found by finding the value of k for which

$$\left[r_{p_{j,k}} - r_{s_{j,k}} \right] \left[r_{p_{j,k+1}} - r_{s_{j,k+1}} \right] < 0.0 \qquad 3.21$$

After finding which side of the intersection line that a particular bow shock point lies, the correct set of infinity conditions required for the shock jump relations are determined. The bow shock moves as part of the time-dependent solution. Therefore, the position of the intersection line is recalculated before each time step. This completes the shock jump predictor step.

The shock jump corrector step is very similar to the predictor step with only two major differences. First, instead of using Equation 3.9 to compute the corrected shock radius, a modified Euler formula is used and is given by

$$r_{s_{j,k}}^{n+1} = r_{s_{j,k}}^{n} + \frac{\Delta\tau}{2}\left[\left(r_{s_t}\right)_{j,k}^{n} + \left(r_{s_t}\right)_{j,k}^{\overline{n+1}}\right] \qquad 3.22$$

Second, when calculating the pressure behind the bow shock, Equation 3.5 and a modified version of Equation 3.6 are used which is given by

$$\begin{aligned} U_{i,j,k}^{n+1} = \frac{1}{2}\Bigg[& U_{i,j,k}^{pc} + U_{i,j,k}^{\overline{n+1}} - \frac{\Delta\tau}{\Delta\xi}\left(F_{i+1,j,k}^{\overline{n+1}} - F_{i,j,k}^{\overline{n+1}}\right) \\ & - \frac{\Delta\tau}{\Delta\eta}\left(G_{i,j,k}^{\overline{n+1}} - G_{i,j-1,k}^{\overline{n+1}}\right) - \frac{\Delta\tau}{\Delta\zeta} H_{i,j,k}^{\overline{n+1}} - \Delta\tau D_{i,j,k}^{\overline{n+1}}\Bigg] \end{aligned} \qquad 3.23$$

Note that a forward difference is used to approximate the $\partial F/\partial\xi$ derivative instead of the usual backward difference. This reduces the method's second-order accuracy in the vicinity of the bow shock but does not harm the overall solution accuracy.

D. Boundary Conditions

The boundary conditions must be incorporated with the sweeping procedure presented earlier. Since only one k-plane of predicted or corrected values is computed at a time, only one k-plane of boundary conditions can be completed at a time. Figure 13 shows a schematic of a typical k-plane in the physical domain with the various boundary conditions indicated.

Along the bow shock the shock jump conditions are applied (as previously discussed) and are given by Equations 3.14 - 3.19. The wall boundary conditions are determined by specifying an isothermal

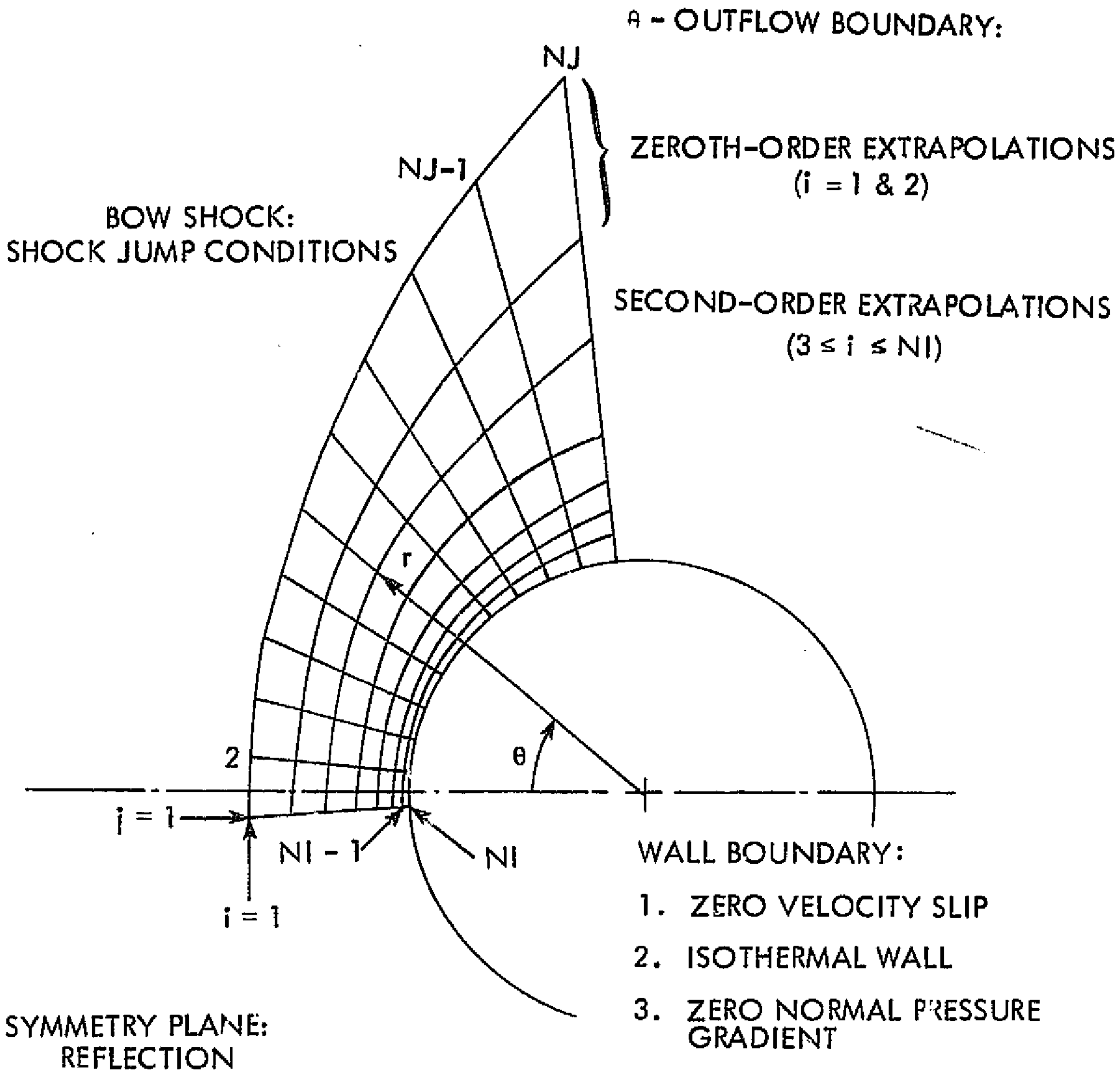

Figure 13. Physical z-plane showing boundary conditions.

wall, a zero normal pressure gradient, and the no-slip condition. These conditions are given by

$$\begin{aligned}
(u_r)_{NI,j,k} &= 0.0 \\
(u_\theta)_{NI,j,k} &= 0.0 \\
(u_z)_{NI,j,k} &= 0.0 \qquad\qquad 3.24 \\
e_{NI,j,k} &= c_v T_w = e_w = \text{constant} \\
\rho_{NI,j,k} &= \rho_{NI-1,j,k}\, e_{NI-1,j,k}/e_w
\end{aligned}$$

where T_w is the specified wall temperature. A perfect gas assumption is required to formulate these boundary conditions.

The θ-outflow boundary is treated with a second-order extrapolation and is given by

$$U_{NJ} = 3(U_{NJ-1} - U_{NJ-2}) + U_{NJ-3} \qquad 3.25$$

where U stands for any of the primitive solution variables. This boundary condition is stable provided the outflow Mach number in the inviscid region of the shock layer is supersonic. When this boundary condition is used near the intersection line for the shock impingement case, numerical difficulties are experienced. The problem arises because Equation 3.25 attempts to extrapolate across the nearly discontinuous region just downstream of the intersection line at $i = 1$ and 2. To correct this a zeroth-order extrapolation is used instead of the second-order extrapolation along $i = 1$ and 2.

A plane of symmetry lies equidistant between the two grid planes at $j = 1$ and 2. This permits a reflective set of boundary conditions at $j = 1$ which is given by

$$\begin{aligned} (u_r)_{i,1,k} &= (u_r)_{i,2,k} \\ (u_\theta)_{i,1,k} &= -(u_\theta)_{i,2,k} \\ (u_z)_{i,1,k} &= (u_z)_{i,2,k} \end{aligned} \qquad 3.26$$

$$\begin{aligned} \rho_{i,1,k} &= \rho_{i,2,k} \\ e_{i,1,k} &= e_{i,2,k} \end{aligned} \qquad 3.27$$

Notice that all solution components are reflected in a positive manner, except the tangential velocity component (u_θ), which is reflected in a negative manner.

Boundary conditions for the inflow and outflow planes in the z-direction are now discussed (see Figure 14). The flow variables at the inflow plane $(i,j,1)$ are held fixed for all time equal to the conditions from a swept infinite cylinder solution calculated prior to the shock impingement solution. The flow variables at the outflow boundary are determined using a zeroth-order extrapolation given by

$$U_{i,j,NK} = U_{i,j,NK-1} \qquad 3.28$$

where U stands for any of the five primitive solution variables.

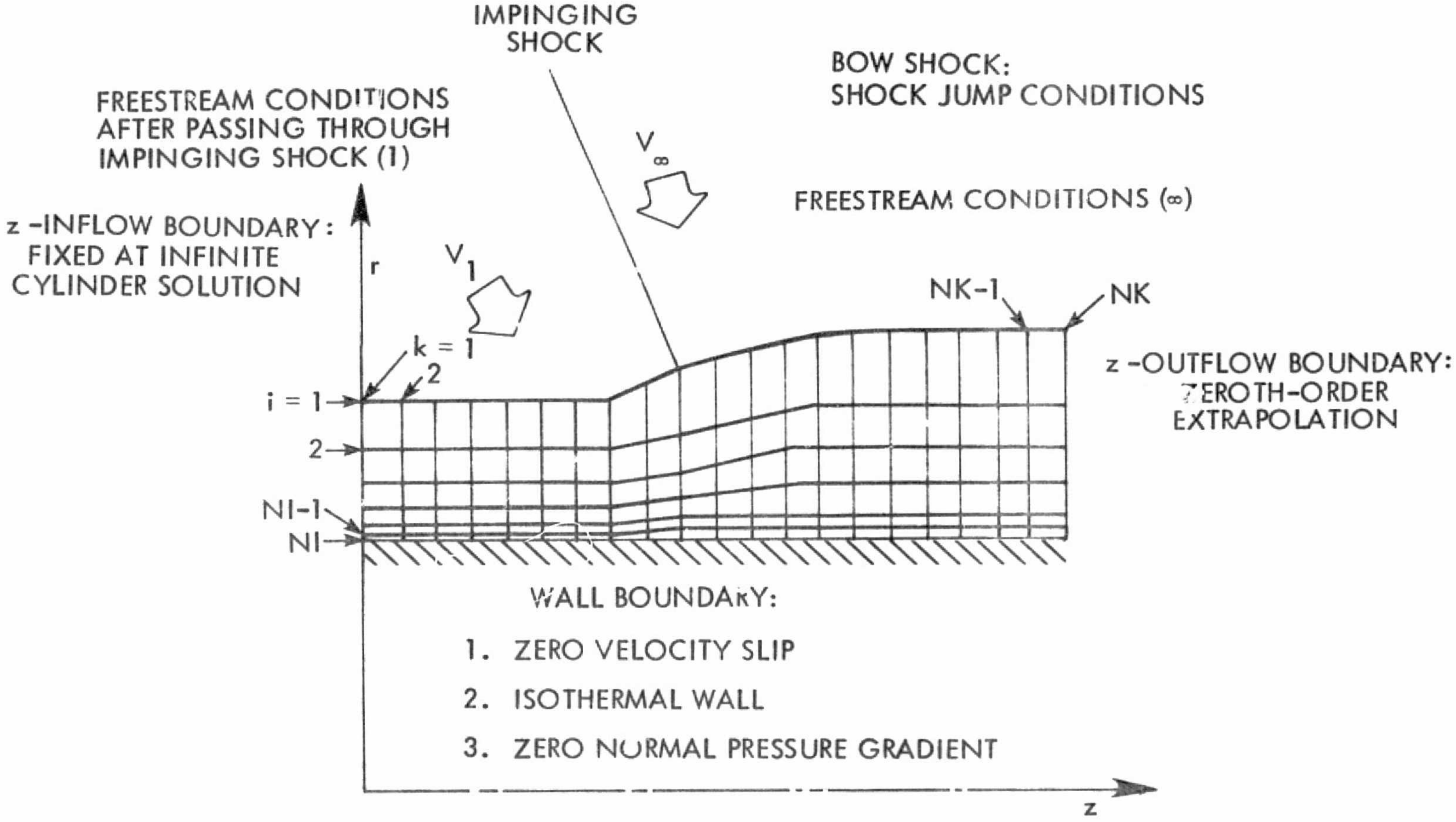

Figure 14. Physical θ-plane showing boundary conditions.

E. Initial Conditions

A swept infinite cylinder solution is calculated prior to the shock impingement solution with freestream conditions matching the conditions behind the impinging shock (region 1, Figure 14). The conditions behind the impinging shock are computed using oblique shock equations [64].

The infinite cylinder solution is computed from the same computer code which computes the three-dimensional shock impingement solutions. An infinite cylinder solution, by definition, must have all z-gradients equal to zero. Rather than impose this condition directly, by setting all z-derivatives equal to zero and thereby changing the computer code drastically, it is done indirectly by changing certain boundary conditions. That is, the z-derivatives are still calculated but automatically come out to be zero because all z-planes are forced to be identical. This identity can be achieved simply by changing two boundary conditions. First, reference to the impinging shock is removed at the bow shock thus taking away the z-gradients across the intersection line. Second, the inflow z-plane (k = 1), instead of being held fixed, is determined by a zeroth-order extrapolation given by

$$U_{i,j,1} = U_{i,j,2} \tag{3.29}$$

where U stands for any of the five primitive solution variables. This removes the z-gradient which could exist between the first two z-planes of the solution. In addition, all z-planes of the infinite cylinder initial condition solution must be identical. With all of these conditions satisfied, a mechanism for producing a nonzero z-gradient does not exist. This procedure yields an identical infinite cylinder solution in each z-plane of the finite-difference grid.

Because all z-planes of the infinite cylinder solution are identical only a single z-plane is needed to completely specify the solution. However, because of the three-dimensional computer code's structure, a minimum of four z-planes must be used to compute an infinite cylinder solution. Two of these four z-planes are boundary condition planes ($k = 1$ and $k = 4$).

At the beginning of a three-dimensional impingement solution calculation, the flow field solution in each z-plane is set equal to the infinite cylinder solution. The shock radius array (r_s), the shock velocity array (r_{s_t}), and the shock slope arrays (r_{s_θ} and r_{s_z}) as well as the flow field variables are initialized in this way. The initial condition infinite cylinder solution is also the solution maintained as the fixed boundary condition at $k = 1$.

The procedure used to establish the infinite cylinder initial condition solution is similar to the procedure used by Tannehill et al. [54]. It involves the approximate curve fit of Billig [65] to get the shock shape and slope, the shock jump conditions with r_{s_t} set equal to zero to get the flow variables behind the bow shock, a Newtonian pressure distribution and wall boundary conditions to get the flow variables on the body, and a linear variation between the bow shock and the body to get the interior flow field.

F. Stability

To insure numerical stability the time step associated with MacCormack's method is limited in size by the CFL condition [61,66], which in three-dimensions is given by

$$\Delta\tau \leq C \frac{1}{\frac{|u_r|}{\Delta r} + \frac{|u_\theta|}{r\Delta\theta} + \frac{|u_z|}{\Delta z} + a\sqrt{\frac{1}{(\Delta r)^2} + \frac{1}{(r\Delta\theta)^2} + \frac{1}{(\Delta z)^2}}} \qquad 3.30$$

where a is the speed of sound and C is an adjustable constant.

Numerical solutions involving steep flow field gradients have used special artificial smoothing terms to remain stable [67-70]. A modified version of the fourth-order product-smoothing term first developed by MacCormack [71] is used in the present study. The original smoothing procedure can be expressed by two basic terms $\left(S^n_{i,j,k}, S^{\overline{n+1}}_{i,j,k}\right)$ which are given by

$$S^n_{i,j,k} = \sum_{\ell=i,j,k} c_\ell\left(K^n_{\ell+1}\,\delta_\ell U^n - K^n_\ell \Delta_\ell U^n\right) \qquad 3.31$$

$$S^{\overline{n+1}}_{i,j,k} = \sum_{\ell=i,j,k} c_\ell\left(K^{\overline{n+1}}_\ell\,\delta_\ell U^{\overline{n+1}} - K^{\overline{n+1}}_{\ell-1}\,\Delta_\ell U^{\overline{n+1}}\right) \qquad 3.32$$

where the U's are defined by Equation 2.27, the summations on ℓ indicate one term for each of the three spacial directions (i,j,k), the c's are constant coefficients, the K's are variable coefficients defined by

$$K^n_{i+1} = \frac{\left|\rho^n_{i+2,j,k} - 2\rho^n_{i+1,j,k} + \rho^n_{i,j,k}\right|}{\left(\rho^n_{i+2,j,k} + 2\rho^n_{i+1,j,k} + \rho^n_{i,j,k}\right)} \qquad 3.33$$

and the $\delta_\ell()$ and $\Delta_\ell()$ operators are forward and backward differences, respectively, defined by

$$\delta_i U^n = U^n_{i+1,j,k} - U^n_{i,j,k} \qquad 3.34$$

$$\Delta_i U^n = U^n_{i,j,k} - U^n_{i-1,j,k} \qquad 3.35$$

When smoothing is desired, $S^n_{i,j,k}$ (Equation 3.31) is added to the predictor step (Equation 3.1), and $S^{n+1}_{i,j,k}$ (Equation 3.32) is added to the corrector step (Equation 3.2).

The variable K-coefficients are composed of a normalized second-order difference of flow field density. The K subscript indicates which direction the difference is in (i,j or k) and also the center of the difference. The K superscript indicates the time level used for the values of density. This always positive variable coefficient is essentially zero in the smooth regions of the flow field and approaches a maximum value of one in regions of large point-wise oscillations. The theoretical maximum value of the coefficient product in front of the U-differences, namely the cK products, is one-half. The K-coefficients can theoretically reach a value of one, causing the c_i, c_j, and c_k constant coefficients to be restricted to a value of one-half or less. However, since the K-coefficients in practice are usually much smaller than one, the constant coefficients can be much larger than one-half. Of course, smaller amounts of smoothing or smoothing in only one or two of the three spacial directions can also be obtained. This is achieved by independently setting the constant coefficients in each of the three directions equal to the appropriate values.

A major difficulty arises when applying this smoothing method to the sweeping procedure presented earlier. To obtain both the predicted and corrected smoothing terms at a particular value of k, solution variables from five k-planes are needed (k + 2, k + 1, k, k - 1, k - 2). Providing the information from such a large number of k-planes does not fit within the framework of the sweeping procedure. At most, information from only three k-planes can be supplied. This leads to a modification of MacCormack's smoothing technique which is given by

$$S^{pp}_{i,j,k} = \sum_{\ell=i,j} c_\ell\left(K^n_{\ell+1}\,\delta_\ell U^n - K_\ell \Delta_\ell U^n\right)$$

$$+ c_k K^n_k (U^n_{i,j,k} - \Delta_k U^n) \qquad 3.36$$

$$S^{cp}_{i,j,k} = c_k K^n_k\, U^n_{i,j,k+1} \qquad 3.37$$

$$S^{c}_{i,j,k} = \frac{1}{2} \sum_{\ell=i,j} c_\ell\left(K^{\overline{n+1}}_\ell\, \delta_\ell U^{\overline{n+1}} - K^{\overline{n+1}}_{\ell-1}\, \Delta_\ell U^{\overline{n+1}}\right)$$

$$+ \frac{1}{2} c_k K^{\overline{n+1}}_k \left(\delta_k U^{\overline{n+1}} - \Delta_k U^{\overline{n+1}}\right) \qquad 3.38$$

where all notation is as it was previously defined. When smoothing is desired, $S^{pp}_{i,j,k}$, the partial-predictor-smoother step, is added to the partial-predictor step (Equation 3.3), $S^{cp}_{i,j,k}$, the completor-predictor-smoother step, is added to the completor-predictor step (Equation 3.4), and $S^{c}_{i,j,k}$, the corrector-smoother step, is added to the completor-corrector step (Equation 3.6).

Note that the modification does not alter the terms in either the i- or j-directions, only the k-direction. Instead of using K-coefficients centered at three different k-locations ($k+1$, k, $k-1$), all K's in the k-direction are centered at k. This modification alone reduces the number of k-planes involved to three.

All quantities in the partial-predictor-smoother step (Equation 3.36) are obtained from two k-planes (k and $k-1$), except $\rho^{n}_{i,j,k+1}$ which appears in the K^{n}_{k} coefficient. Since only the k and $k-1$ planes of the n-level solution exist in SCM at this time, extra density information at $k+1$ must be obtained from LCM. These coefficients are then saved and used in the completor-predictor-smoother step (Equation 3.37).

Instead of breaking the corrector-smoother step into two parts, it is applied as one step just after the completor-corrector step. This is because a third plane of densities (at $k+1$) cannot be read into SCM from LCM to compute a partial-corrector-smoother step. Because of the sweeping procedure, the $\overline{n+1}$-level solution at $k+1$ has not been computed yet. At the time the partial-corrector step is completed, the entire $\overline{n+1}$ solution at $k-1$ is saved in SCM. This can be considered as a partial-corrector-smoother step even though no computations are actually made. Then, after the completor-corrector step is computed, the entire corrector-smoother step (Equation 3.38) is computed with all three k-planes existing in SCM.

When Equation 3.12 is used to compute the shock slopes in the z-direction (r_{s_z}) an unstable point-wise oscillation results in the z-direction. This instability is strongest near the z-direction inflow plane. To alleviate this problem a shock radius smoother is applied during the corrector step which is given by

$$r_{s_{j,k}}^{n+1}\Big|_{new} = r_{s_{j,k}}^{n+1}\Big|_{old} + \alpha\left(r_{s_{j,k+1}}^{\overline{n+1}} - 2r_{s_{j,k}}^{\overline{n+1}} + r_{s_{j,k-1}}^{\overline{n+1}}\right) \qquad 3.39$$

where α is an adjustable constant. When α has a value of 0.25 the amount of smoothing which occurs corresponds to the optimal flattening of a sawtooth curve (r_s vs z distribution) into a straight line. Larger values of α will produce "over smoothing" and if large enough (above 0.5) will actually feed the instability. Values of α smaller than 0.25 (up to an order of magnitude smaller) will allow oscillations to exist but will still keep the procedure stable.

IV. DISCUSSION OF RESULTS

The present method was used to compute two-dimensional blunt body, swept infinite cylinder, and three-dimensional shock impingement solutions. Results for these three problems are presented in this chapter along with the computational statistics of the computer code. In all cases considered in this chapter, air is assumed to be a perfect gas. The Prandtl number (Pr), the coefficient of specific heat at constant pressure (c_p), and the ratio of specific heats (γ) are held constant and are given by

$$\begin{aligned} Pr &= 0.72 \\ c_p &= 1004.58\ m^2/sec^2 - {}^{o}K \qquad 4.1 \\ \gamma &= 1.40 \end{aligned}$$

The simplest case, that of the two-dimensional blunt body solution, is presented first.

A. Two-Dimensional Blunt Body Solution

The two-dimensional blunt body solution was computed using the three-dimensional code in the same manner as the infinite cylinder solutions but with the freestream cross-flow velocity set equal to zero.

The freestream conditions chosen for this two-dimensional computation were

$$\begin{aligned} M_\infty &= 5.94 & p_\infty &= 545.8\ N/m^2 \\ Re_{D,\infty} &= 17326 & T_\infty &= 62.8\ {}^{o}K \end{aligned} \qquad 4.2$$

where M is the Mach number, p is the pressure, T is the temperature, and Re_D is the Reynolds number based upon the cylinder diameter. Other conditions pertinent to this case were chosen to be

$$D = 0.025 \text{ m} \qquad T_w = 1444.4\ ^{\circ}K$$
$$\lambda = 0^{\circ} \qquad \beta = 0 \tag{4.3}$$

where D is the cylinder diameter, λ is the cylinder sweep angle, β is the radial mesh stretching parameter, and T_w is the constant wall temperature. Note that a λ of zero indicates no sweep and therefore, a two-dimensional blunt body case. A β of zero indicates no stretching of the mesh in the radial direction. The adiabatic wall temperature (T_{aw}) in the stagnation region was computed to be 504.9 °K from

$$T_{aw} = T_e\left(1 + r\,\frac{\gamma - 1}{2}\,M_e^2\right) \tag{4.4}$$

where e denotes the edge of the boundary layer and r is the recovery factor set equal to 0.85 for a laminar boundary layer. On comparing the T_w and T_{aw} values, it is apparent that this case has an extremely hot wall.

The computational mesh consisted of 21 equally spaced points in both the radial and tangential directions. The tangential outflow boundary was located along a radial ray 83.8° above the stagnation streamline. The results of this computation are shown in Figures 15 and 16.

A plot of the pressure distribution around the cylinder is shown in Figure 15. The circles are the current numerical results. The solid

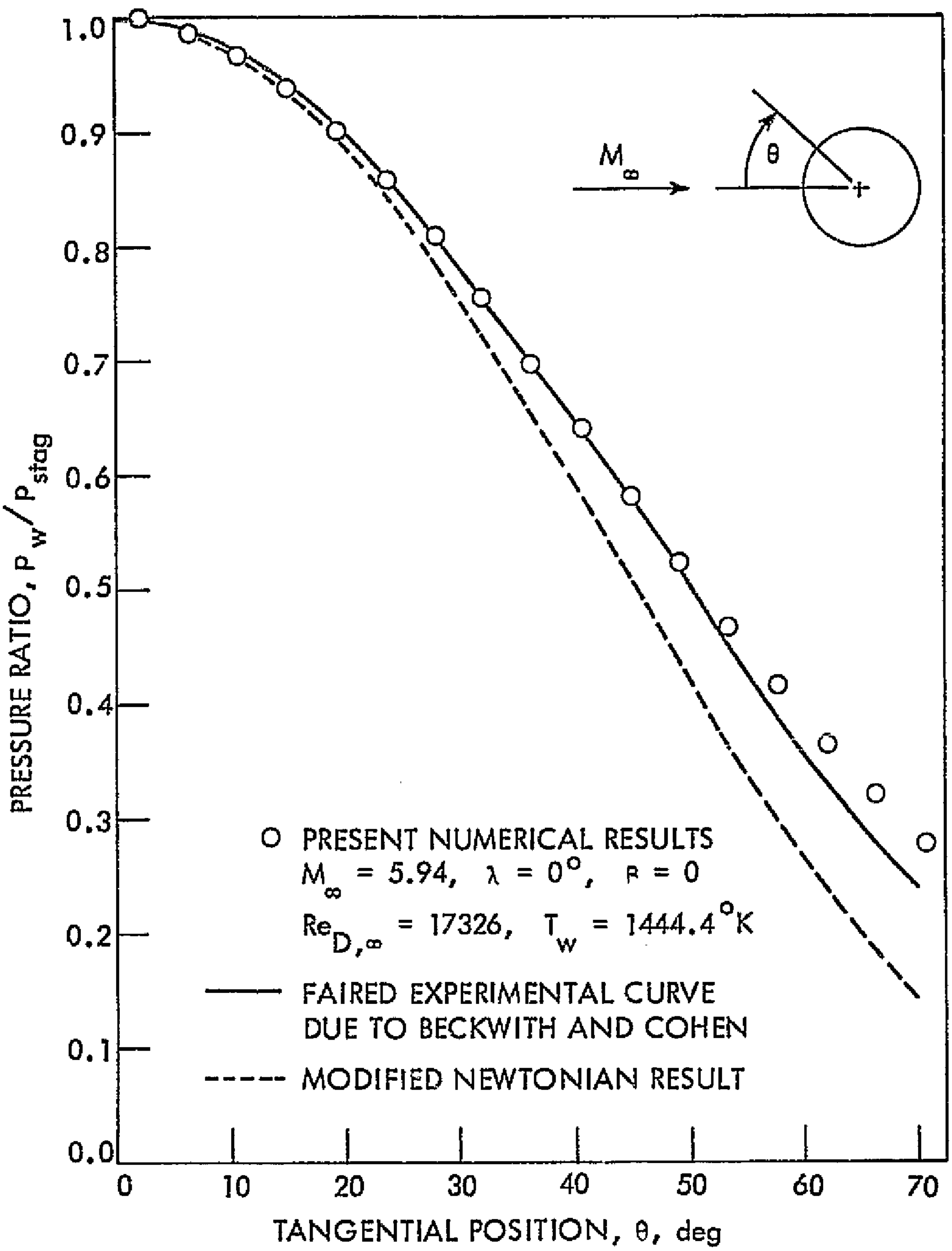

Figure 15. Comparison of pressure distributions on a two-dimensional circular cylinder.

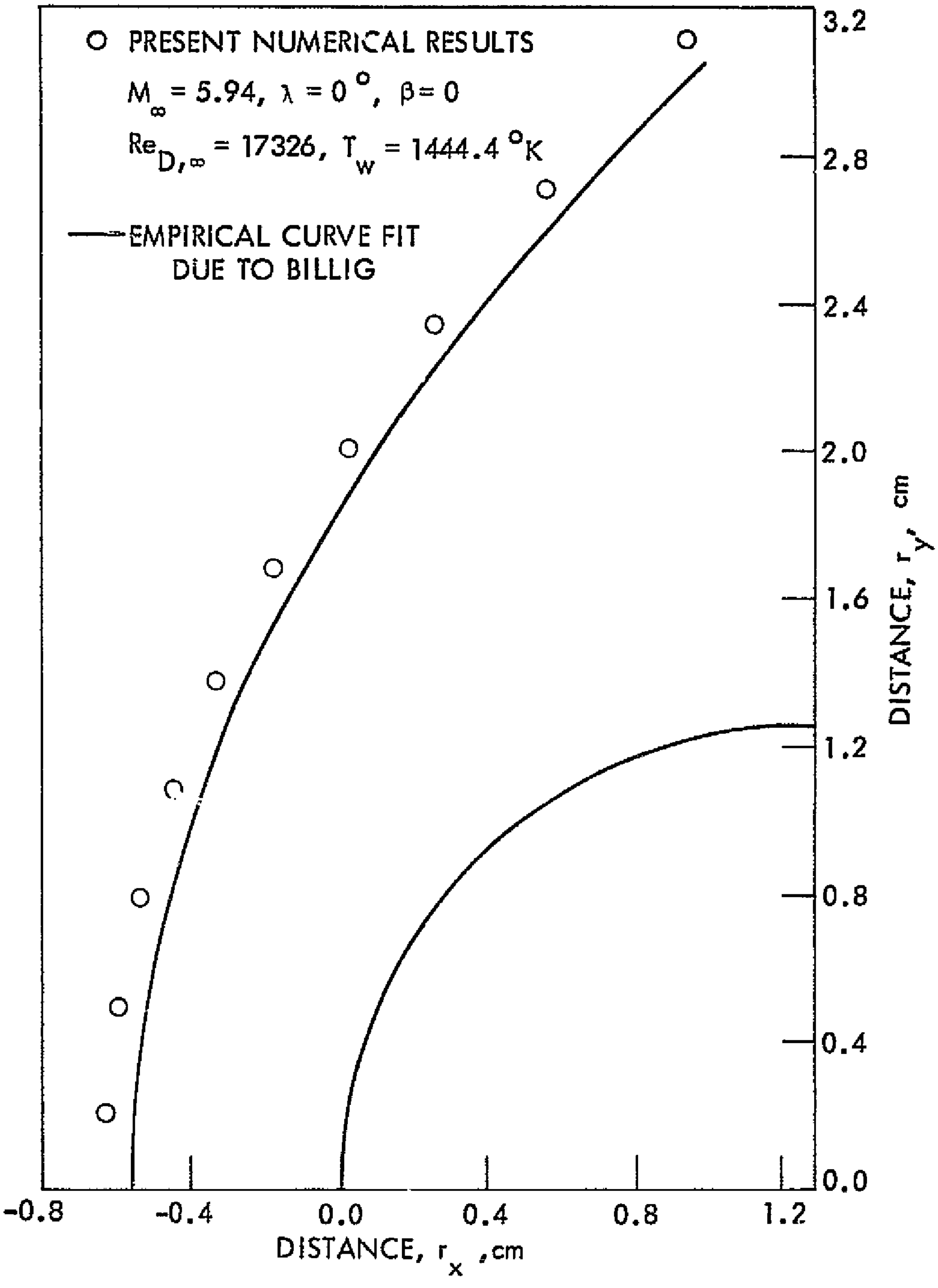

Figure 16. Comparison of shock shapes around a two-dimensional circular cylinder.

curve is a fairing of experimental data due to Beckwith and Cohen [72]. This faired experimental curve consists of data from both two-dimensional blunt body and infinite cylinder results over a range of Mach number. This pressure distribution is independent of sweep angle and normal Mach numbers above two. The dashed curve shown in Figure 15 is the result predicted by the modified Newtonian pressure distribution given by

$$\frac{p_w}{p_{stag}} = \left(1 - \frac{p_\infty}{p_{stag}} \cos^2\theta + \frac{p_\infty}{p_{stag}}\right) \qquad 4.5$$

where p_{stag} is the stagnation point pressure computed from the Rayleigh pitot formula [64].

All three results are in excellent agreement in the stagnation region of the blunt body. In fact, the error between the present numerical result and the stagnation value of pressure as predicted by the Rayleigh pitot formula is less than 0.1 percent. As expected the modified Newtonian pressure disagrees with the other two results away from the stagnation region. The faired experimental curve and the numerical results start disagreeing at about $\theta = 50^\circ$. This disagreement increases to a maximum of about five percent error at $\theta = 80^\circ$. The scatter of the experimental data used to obtain the faired experimental curve in Figure 15 was about ± five percent at $\theta = 80^\circ$.

A comparison of the numerically predicted shock shape with the empirical result of Billig [65] is shown in Figure 16. The circular symbols represent the numerical result while the empirical result is shown as a solid curve. The error between the two results, to a large extent, is due to the extremely hot wall. The large wall temperature heats the boundary layer causing the fluid density near the wall to decrease. This apparently has the effect of increasing the bow shock standoff distance as seen in the next section on infinite cylinder solutions.

B. Swept Infinite Cylinder Solutions

The swept infinite cylinder solution (as already mentioned) was computed using the three-dimensional computer code by restricting all z-gradients to be zero. This was accomplished with the appropriate choice of boundary and initial conditions. Three swept infinite cylinder solutions were computed to establish the validity of the three-dimensional computer code and are presented in this section. In addition, the swept infinite cylinder solution used as the initial condition of the three-dimensional shock impingement case is also presented. In all of these cases, the computational mesh consisted of 21 mesh points in both the radial and tangential directions. The tangential outflow boundary was in all cases located along a radial ray 83.8° above the stagnation streamline.

The specified conditions chosen for the three infinite cylinder solutions are given in Table 1. The freestream Mach number has been divided into two components, the normal component ($M_{r,\infty}$) and the cross-flow component ($M_{z,\infty}$). Except for the addition of a cross-flow component of velocity, the case A conditions are identical to the two-dimensional case. Because of this, the previously computed two-dimensional solution was chosen as the initial condition for the case A infinite cylinder solution. The time-dependent development of the u_z-velocity

Table 1. Specified conditions for the infinite cylinder solutions.

Specified Quantity	Case A	Case B	Case C
M_∞	6.45	6.45	6.45
$M_{r,\infty}$	5.94	5.94	5.94
$M_{z,\infty}$	2.51	2.51	2.51
$Re_{D,\infty}$	18816	18816	18816
p_∞ (N/m^2)	545.8	545.8	545.8
T_∞ (^oK)	62.8	62.8	62.8
λ (deg)	25.0	25.0	25.0
D (m)	0.025	0.025	0.025
T_w (^oK)	1444.4	1444.4	411.8
$T_{aw,stag}$ (^oK)	573.2	572.0	572.5
β	0.0	1.2	1.2

profile along the stagnation line for case A is shown in Figure 17. The u_z-velocity profile develops from the bow shock toward the body. Moderate oscillations occur in the radial direction during the time-dependent process but completely disappear as the steady-state solution is approached. Initially, the solution moves rapidly toward steady state, however, the final small oscillations damp out very slowly as steady state is approached. The process essentially does not disturb the initial solution in the $r\theta$-plane. This suggests independence between the two-dimensional solution and the cross-flow direction solution.

The second infinite cylinder solution (case B) was computed with exactly the same conditions as the first, but with a different radial distribution of mesh points. The mesh was refined near the body with the stretching parameter (β) equal to 1.2. For this value of β, the first grid point off the body is located at 2.3 percent of the shock standoff distance as compared with five percent for an equally spaced mesh. The mesh distribution for 21 points is tabulated in Table 2 for several values of β. The distance between the body and the bow shock has been normalized to one. The first and second derivatives of the stretching transformation are also tabulated in Table 2.

The u_z-velocity and temperature profiles near the stagnation region ($\theta = 0^\circ$) and the u_θ-velocity profile at $\theta = 36.5^\circ$ are shown in Figures 18, 19 and 20, respectively. The distance between the bow shock and the body (x) is normalized to one for all profiles. For comparative purposes the solutions for no stretching (case A) and for stretching (case B) are both plotted. All three profile comparisons are in excellent agreement.

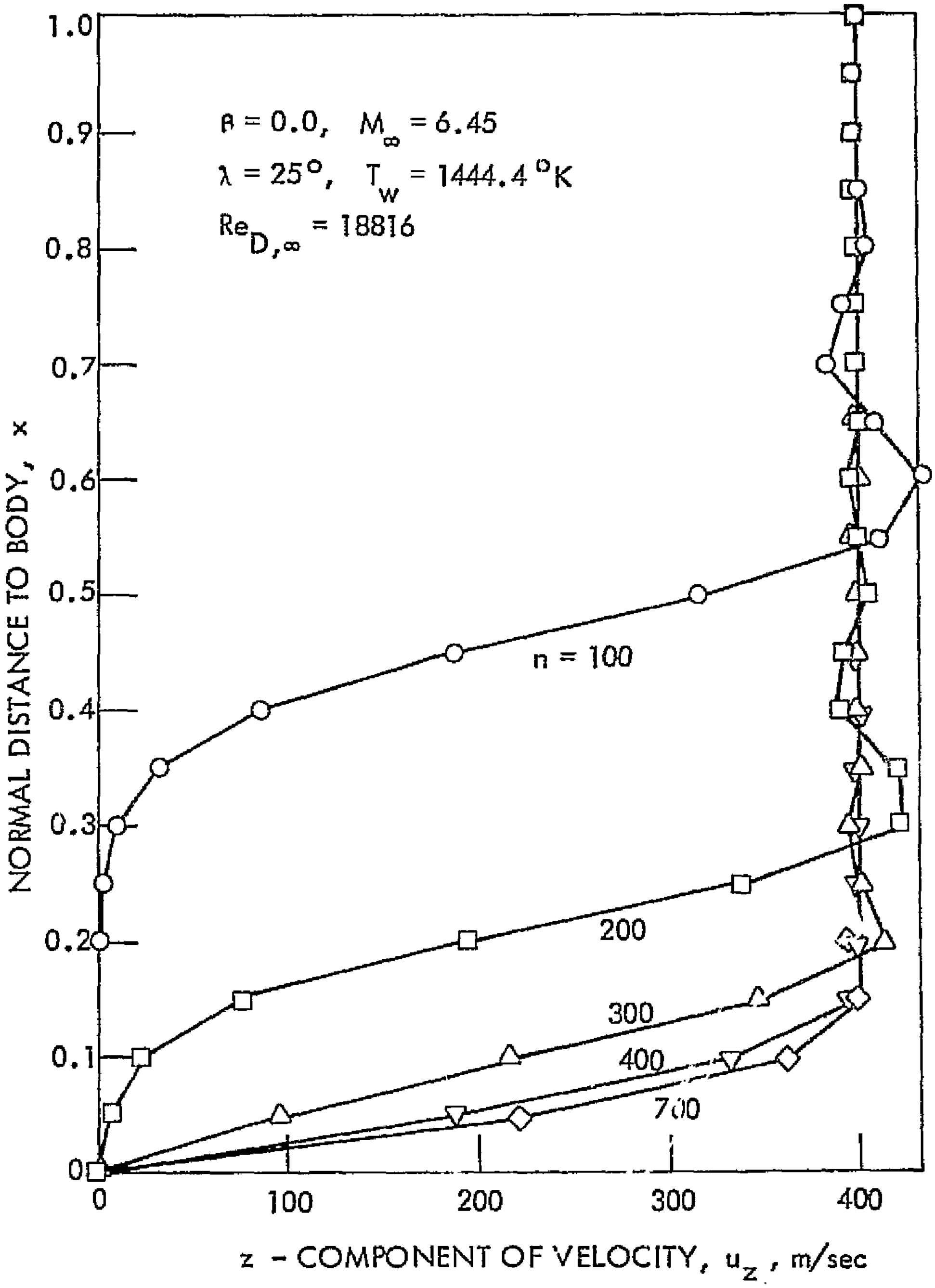

Figure 17. Time development of the u_z-velocity profile near the stagnation region of a swept infinite cylinder.

Table 2. Mesh point distributions for several values of the stretching parameter β.

$\beta = 0$			$\beta = 1.2$			$\beta = 1.12$		
$r - r_b$	$\partial f/\partial x$	$\partial^2 f/\partial x^2$	$r - r_b$	$\partial f/\partial x$	$\partial^2 f/\partial x^2$	$r - r_b$	$\partial f/\partial x$	$\partial^2 f/\partial x^2$
BOW SHOCK								
1.00	1.00	0.0	1.000	0.70	0.00	1.000	0.62	0.00
0.95	1.00	0.0	0.928	0.70	0.07	0.917	0.63	0.08
0.90	1.00	0.0	0.857	0.71	0.14	0.840	0.63	0.16
0.85	1.00	0.0	0.787	0.72	0.22	0.764	0.65	0.26
0.80	1.00	0.0	0.718	0.74	0.31	0.687	0.67	0.37
0.75	1.00	0.0	0.651	0.76	0.40	0.614	0.71	0.49
0.70	1.00	0.0	0.586	0.79	0.51	0.545	0.74	0.65
0.65	1.00	0.0	0.524	0.83	0.65	0.480	0.79	0.84
0.60	1.00	0.0	0.465	0.87	0.80	0.419	0.85	1.08
0.55	1.00	0.0	0.409	0.92	1.00	0.363	0.92	1.38
0.50	1.00	0.0	0.356	0.98	1.23	0.311	1.00	1.77
0.45	1.00	0.0	0.306	1.04	1.51	0.263	1.10	2.28
0.40	1.00	0.0	0.260	1.12	1.86	0.219	1.21	2.93
0.35	1.00	0.0	0.217	1.21	2.29	0.180	1.34	3.78
0.30	1.00	0.0	0.178	1.31	2.82	0.145	1.49	4.88
0.25	1.00	0.0	0.141	1.43	3.49	0.113	1.67	6.33
0.20	1.00	0.0	0.107	1.56	4.32	0.085	1.87	8.23
0.15	1.00	0.0	0.077	1.70	5.36	0.059	2.11	10.73
0.10	1.00	0.0	0.049	1.87	6.66	0.037	2.38	14.03
0.05	1.00	0.0	0.023	2.06	8.29	0.017	2.70	18.37
0.00	1.00	0.0	0.000	2.27	10.34	0.000	3.07	24.11
BODY								

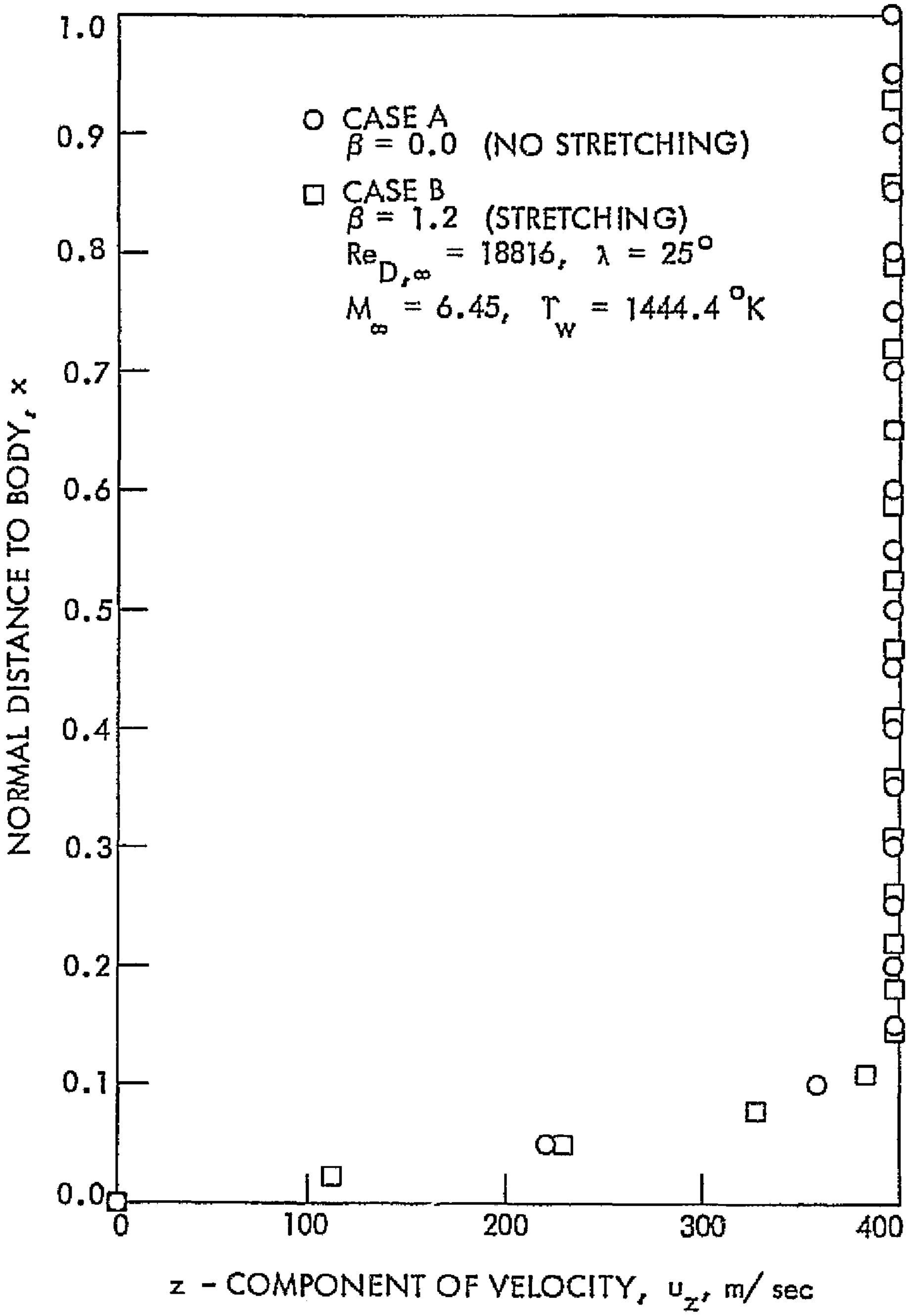

Figure 18. u_z-velocity profile near the stagnation region of a swept infinite cylinder.

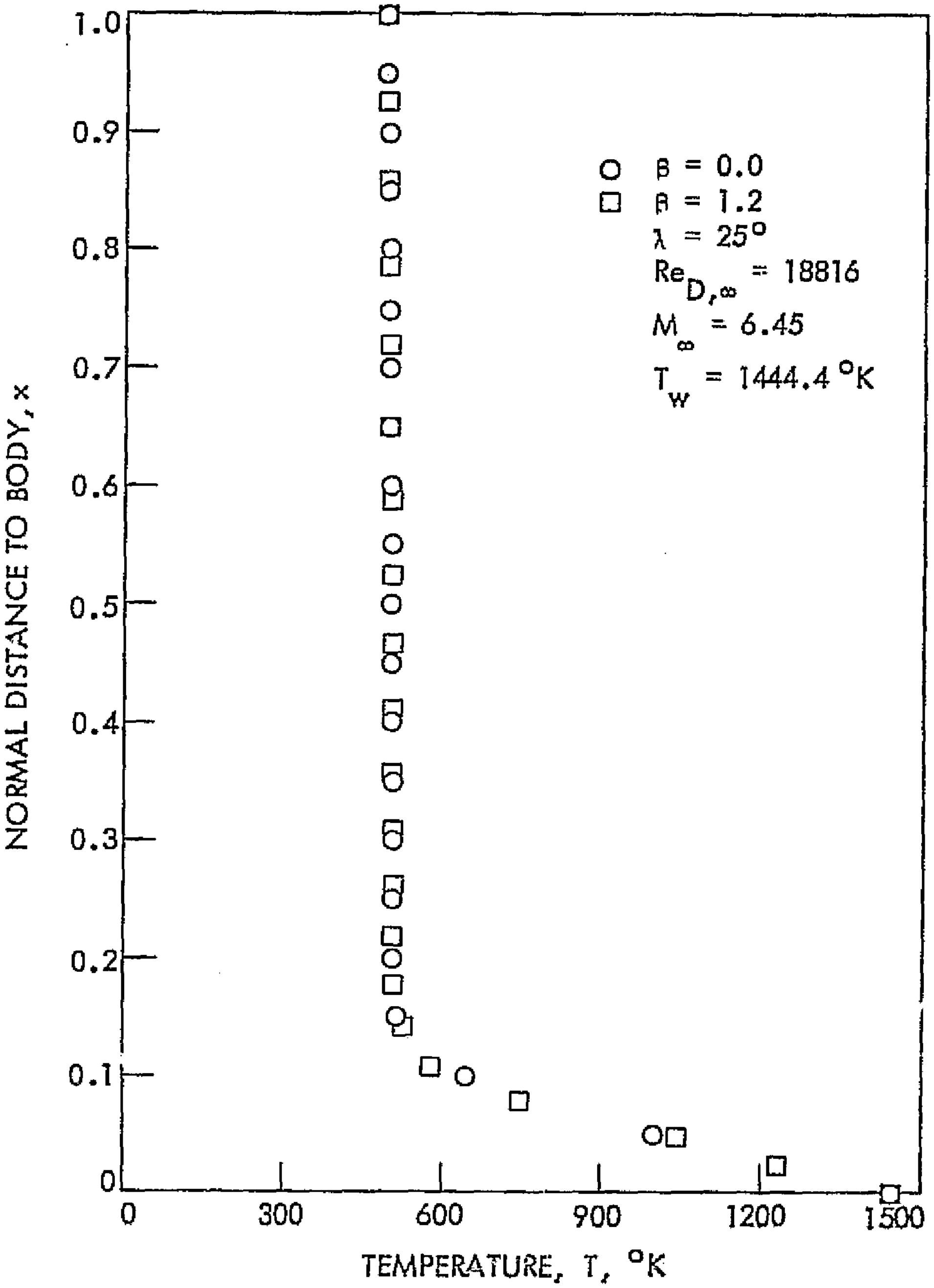

Figure 19. Temperature profile near the stagnation region of a swept infinite cylinder.

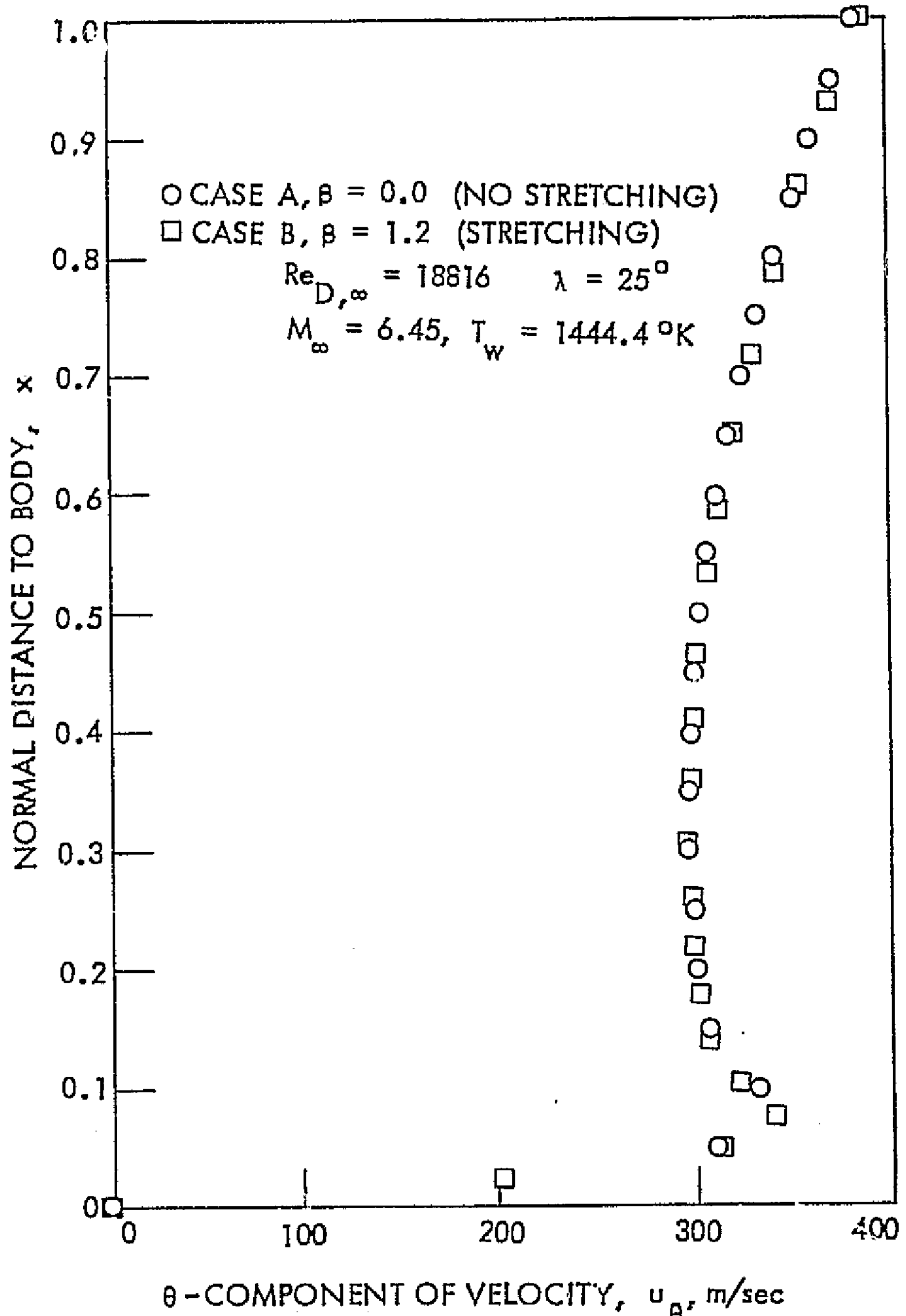

Figure. 20. u_θ-velocity profile at $\theta = 36.5^\circ$ on a swept infinite circular cylinder.

The u_z-velocity profile (Figure 18) is typical of all such profiles on the infinite cylinder regardless of the tangential position. The inviscid portion of the profile has a constant value equal to the z-component of freestream velocity. The boundary layer portion of the profile changes only slightly with tangential position. This occurs in this computation because the mesh expands (due to the shock layer growth) at the approximate growth rate of the boundary layer.

The temperature profile (Figure 19) shows the extent of the hot wall. The u_θ-velocity profile at $\theta = 36.5^\circ$ (Figure 20) has a velocity overshoot which is characteristic of such a hot wall solution. The better boundary layer resolution of the stretched solution is apparent in all three of the profile comparisons. However, even better resolution through more grid points or larger amounts of stretching would be desirable for this solution.

The third infinite cylinder solution (case C) was computed with exactly the same conditions as case B but with a wall temperature slightly less than the adiabatic wall temperature (see Table 1). Therefore, case C is a cold wall case. As pointed out earlier, the hot wall condition seemed to cause a slight increase in the shock standoff distance. A plot of the three infinite cylinder shock standoff results along with the empirical result of Billig [65] is shown in Figure 21. The empirical result was computed from the normal component of the freestream Mach number and therefore, is identical to the two-dimensional shock standoff curve. If a hot wall increases the shock standoff distance, then a cold wall should decrease the shock standoff distance. However, the hot wall cases considered in the previous solutions were

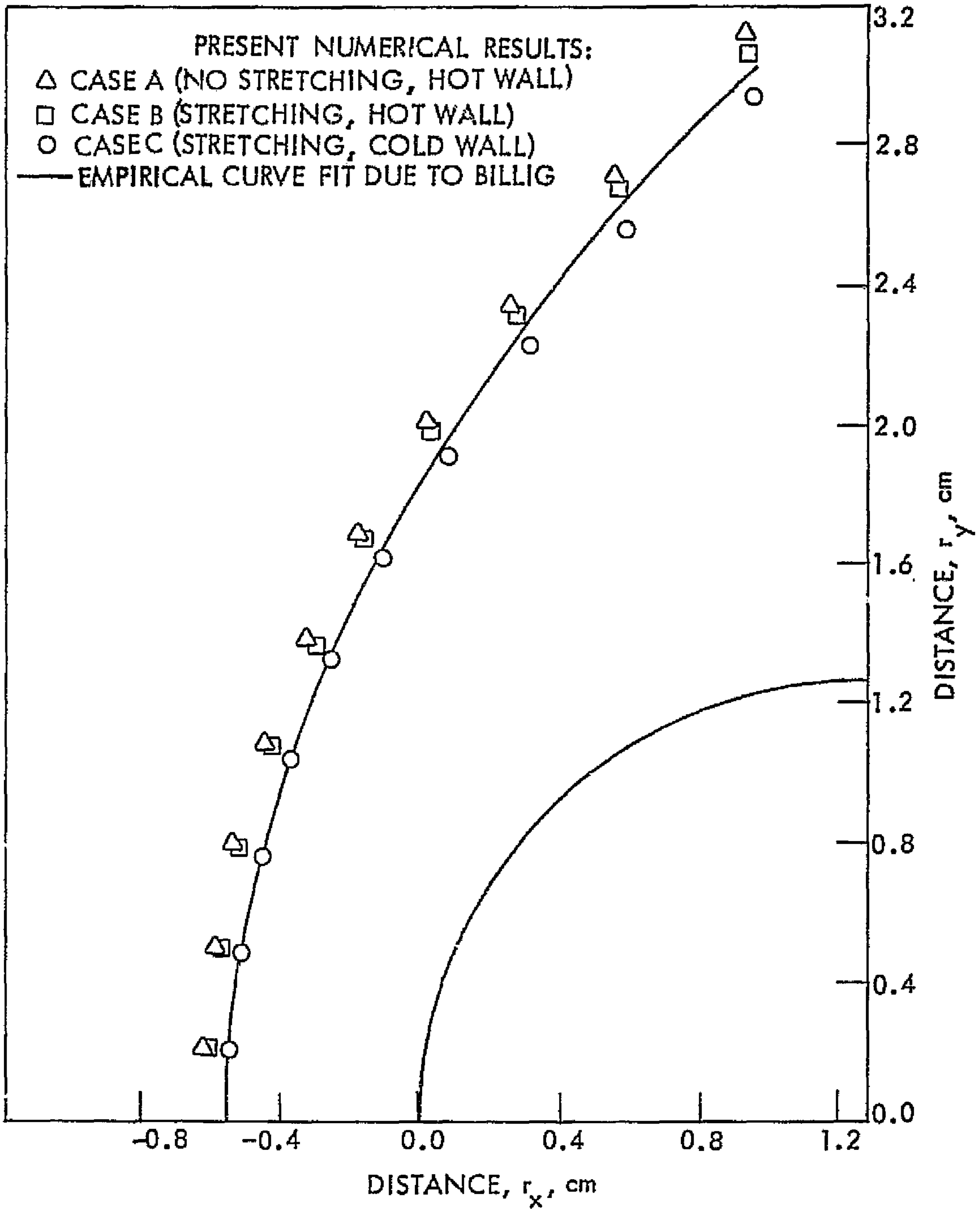

Figure 21. Comparison of shock shapes around a swept infinite circular cylinder.

extreme cases. The cold wall case under current consideration is only a slightly cold wall being very close to the adiabatic wall temperature. Therefore, the close agreement shown in Figure 21 between the cold wall shock shape and the empirical curve fit is expected.

A plot of the pressure distribution around the swept infinite cylinder is shown in Figure 22. The three numerical solutions are represented by symbols. The solid curve is a fairing of experimental data due to Beckwith and Cohen [72] which was discussed earlier. The agreement is generally quite good over the entire curve.

A u_θ-velocity profile comparison is shown in Figure 23. The hot wall profile from Figure 20 (case B) and the cold wall profile of case C are both plotted. Both profiles are from the same position on the cylinder ($\theta = 36.5^\circ$) and have identically stretched meshes. As expected, the velocity overshoot has disappeared from the cold wall profile. Otherwise, the two curves are almost identical.

The infinite cylinder solution used as the initial condition for the three-dimensional shock impingement solution is presented next. The freestream conditions chosen for this case were

$$\begin{aligned} M_{r,\infty} &= 3.77 \qquad & P_\infty &= 2034.8\ \mathrm{N/m^2} \\ M_{z,\infty} &= 2.64 \qquad & T_\infty &= 91.5\ {}^\circ\mathrm{K} \\ Re_{D,\infty} &= 27486 \end{aligned} \tag{4.6}$$

Other conditions pertinent to this case were chosen to be

$$\begin{aligned} D &= 0.025\ \mathrm{m} \qquad & T_w &= 394\ {}^\circ\mathrm{K} \\ \lambda &= 35^\circ \qquad & T_{aw} &= 460\ {}^\circ\mathrm{K} \\ \beta &= 1.12 \end{aligned} \tag{4.7}$$

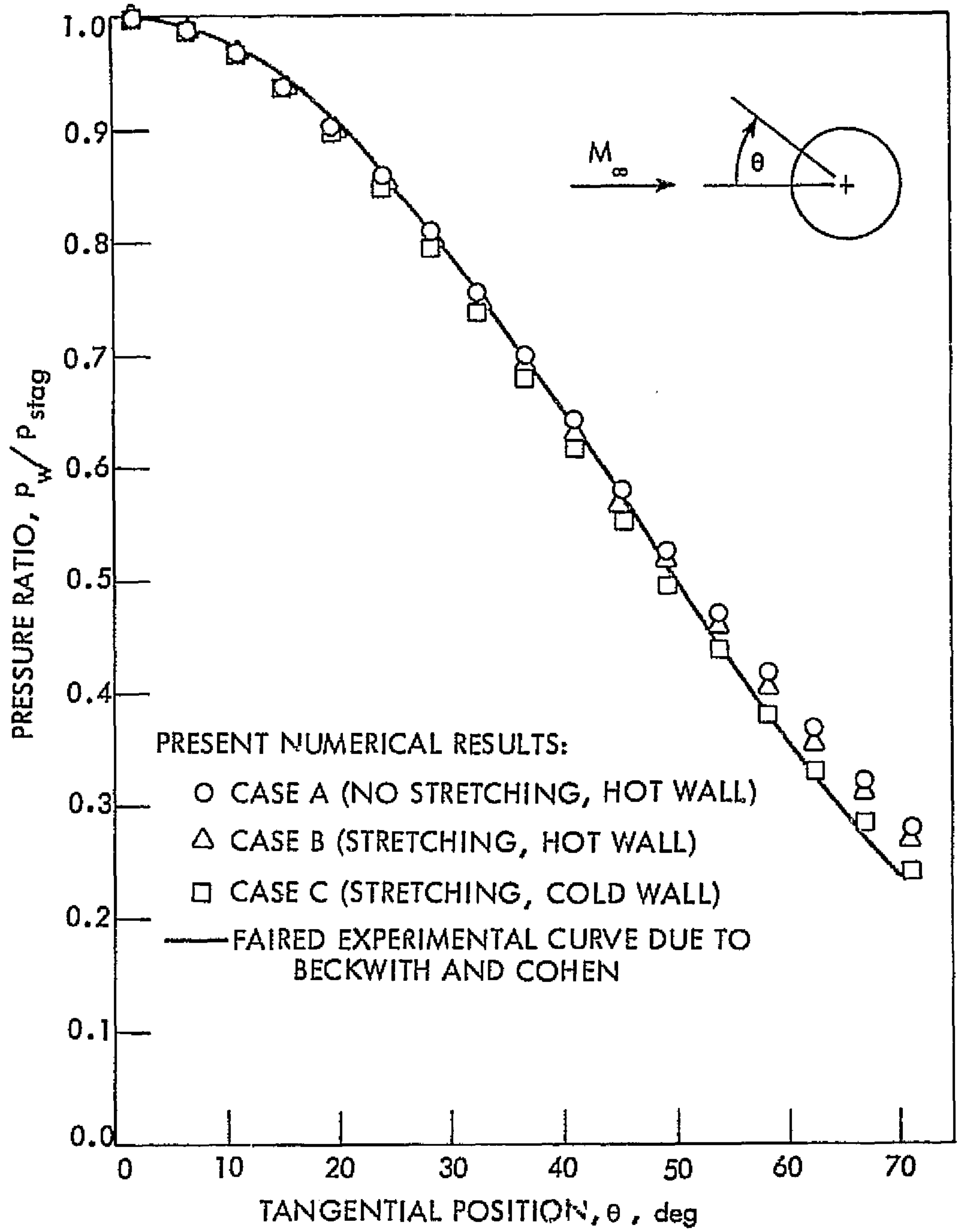

Figure 22. Comparison of the pressure distributions on a swept infinite circular cylinder.

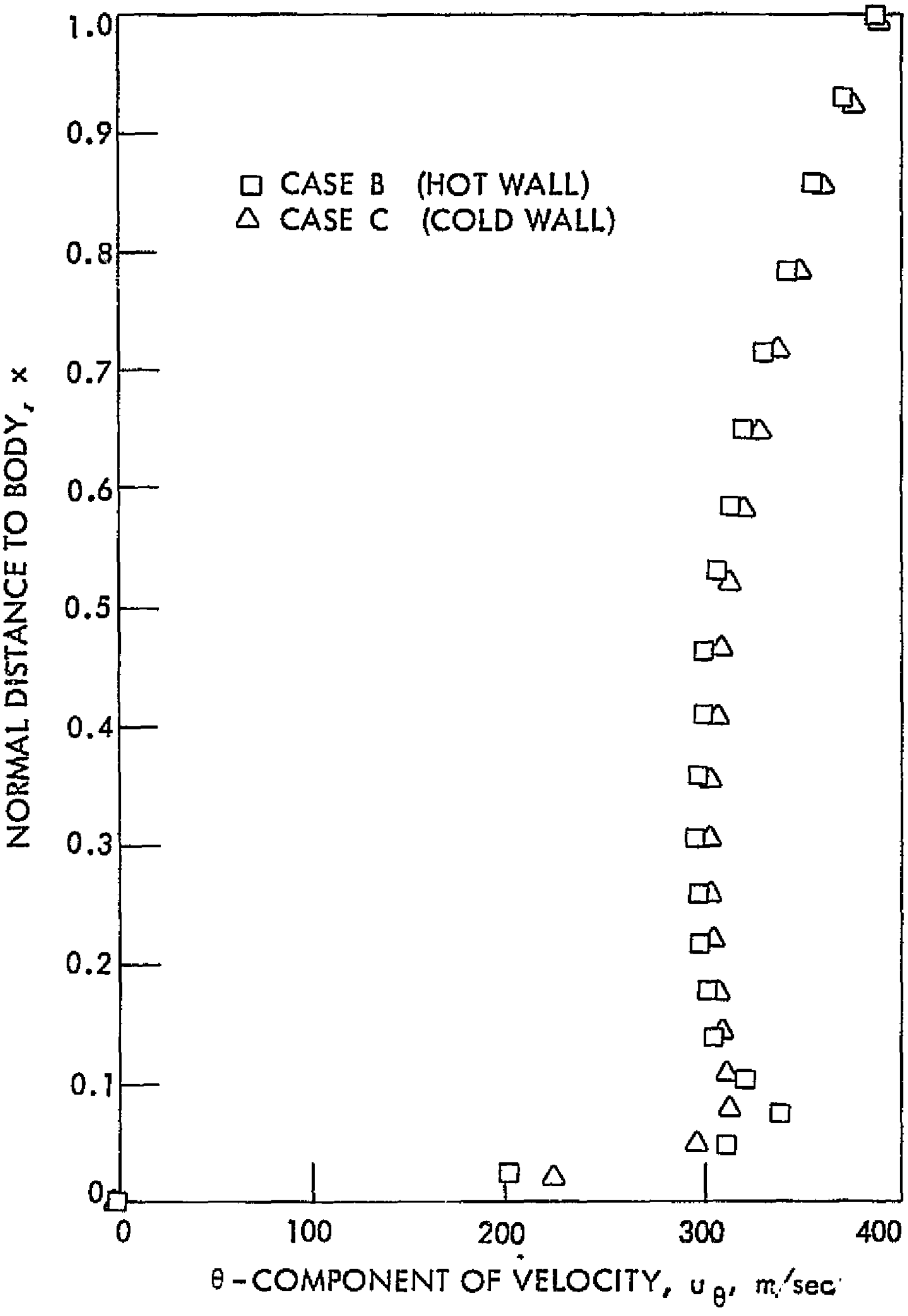

Figure 23. u_θ-velocity profile at $\theta = 36.5^\circ$ on a swept infinite cylinder.

These conditions were selected to permit a comparison with the experiment of Keyes and Hains [2]. The inflow plane in the z-direction for the three-dimensional shock impingement solution is fixed at the initial infinite cylinder solution. Therefore, the freestream conditions for the infinite cylinder solution (except $Re_{D,\infty}$) were computed to agree with the experimental conditions on the downstream side of the impinging shock. These conditions were computed from the given experimental freestream conditions and the oblique shock relations [64]. The freestream viscosity was chosen to be an order of magnitude larger than in the experiment, thus making the Reynolds number ten times smaller. This was done to physically thicken the boundary layer and make its resolution possible with fewer grid points. The results of this computation are shown in Figures 24-30.

A plot of the maximum and the minimum radial shock velocity (r_{s_t}) as a function of time step number (n) is shown in Figure 24. These velocities should approach zero as the steady-state solution is approached. The solution moves rapidly toward a steady state initially with large time-dependent oscillations appearing. In the final part of the solution, the convergence is very slow and has a monotonic behavior.

Plots of the numerical wall pressure and the heat transfer distributions around the swept infinite circular cylinder are shown in Figures 25 and 26, respectively. The pressure distribution in Figure 25 is compared with the faired experimental pressure distribution due to Beckwith and Cohen [72]. The comparison is in general quite good. No experimental results for the heat transfer distribution are available for the

C-2

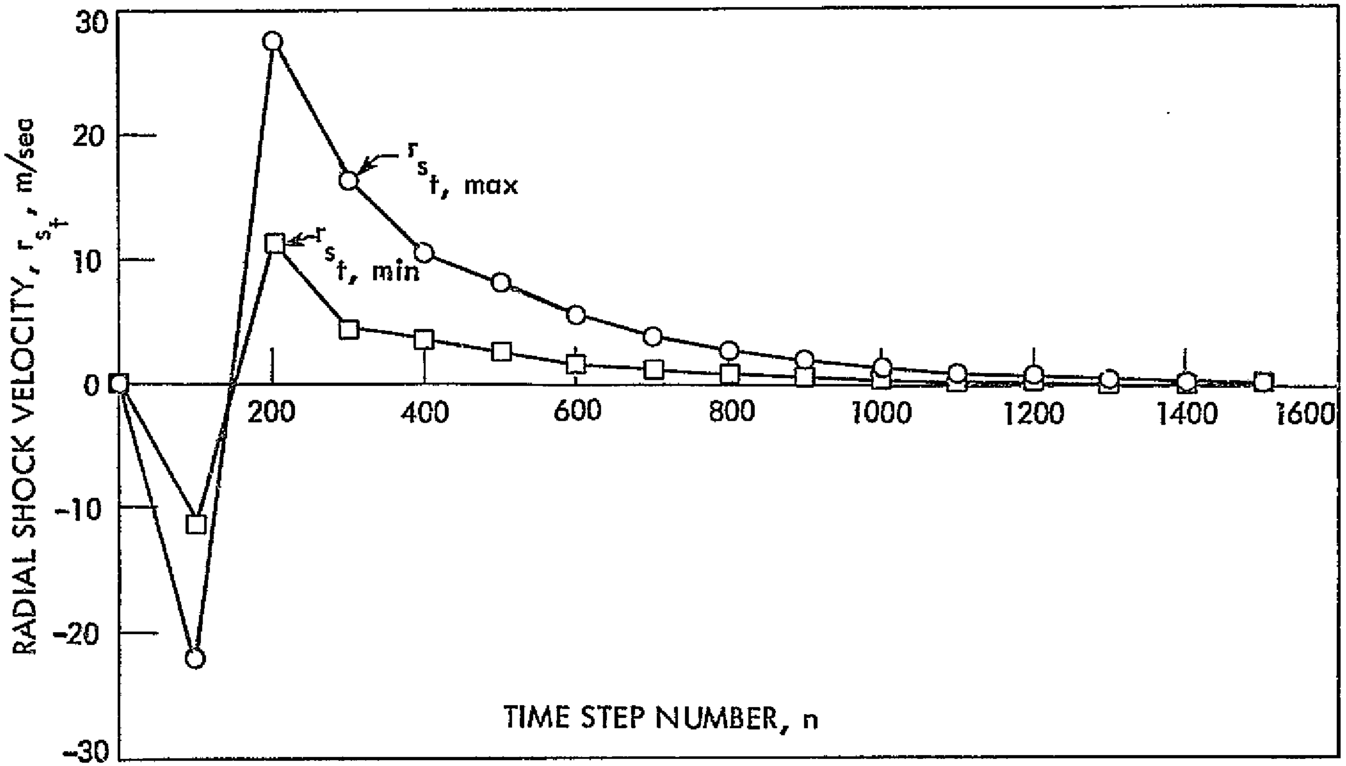

Figure 24. Radial shock velocity as a function of time step number.

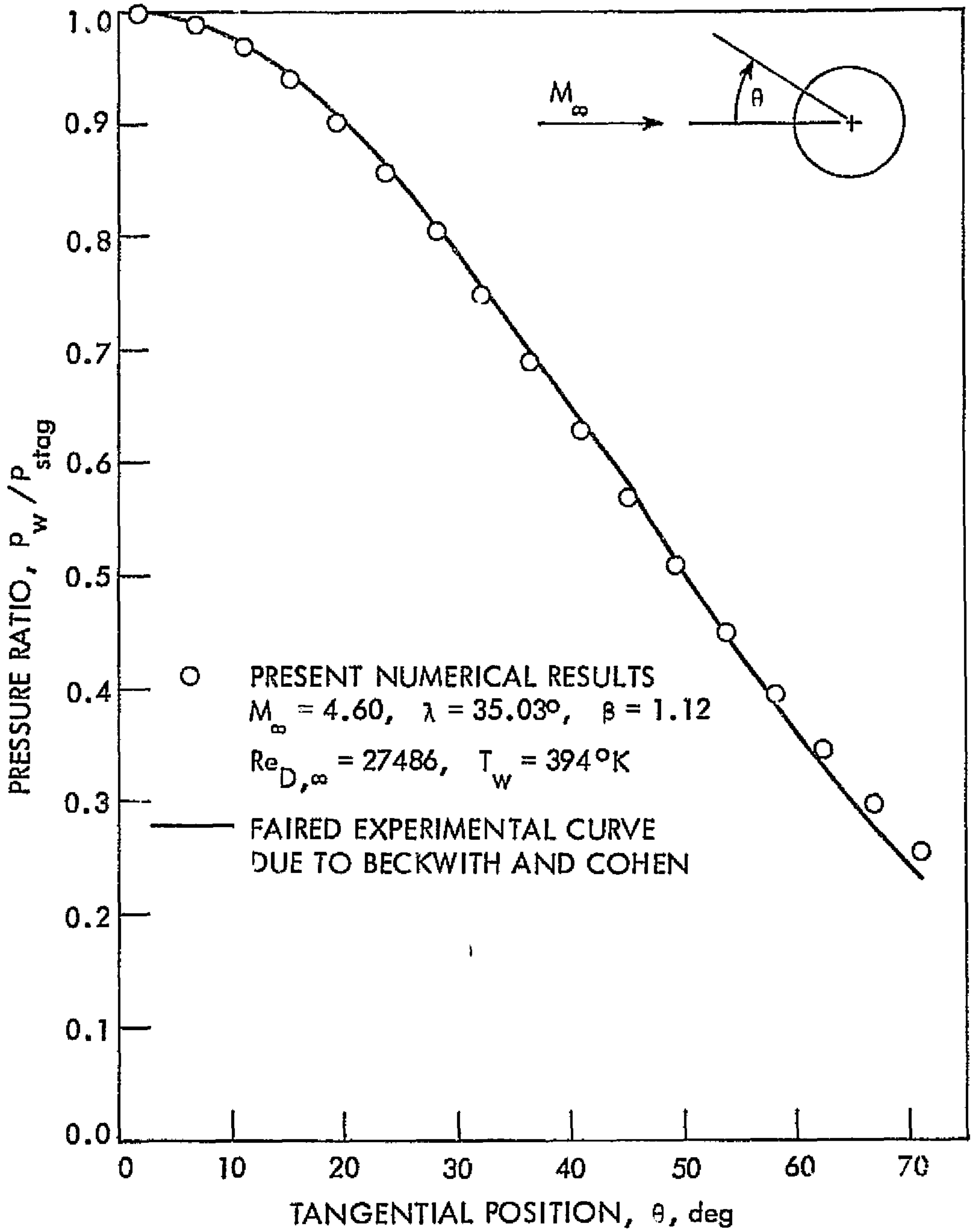

Figure 25. Comparison of the pressure distributions on a swept infinite circular cylinder.

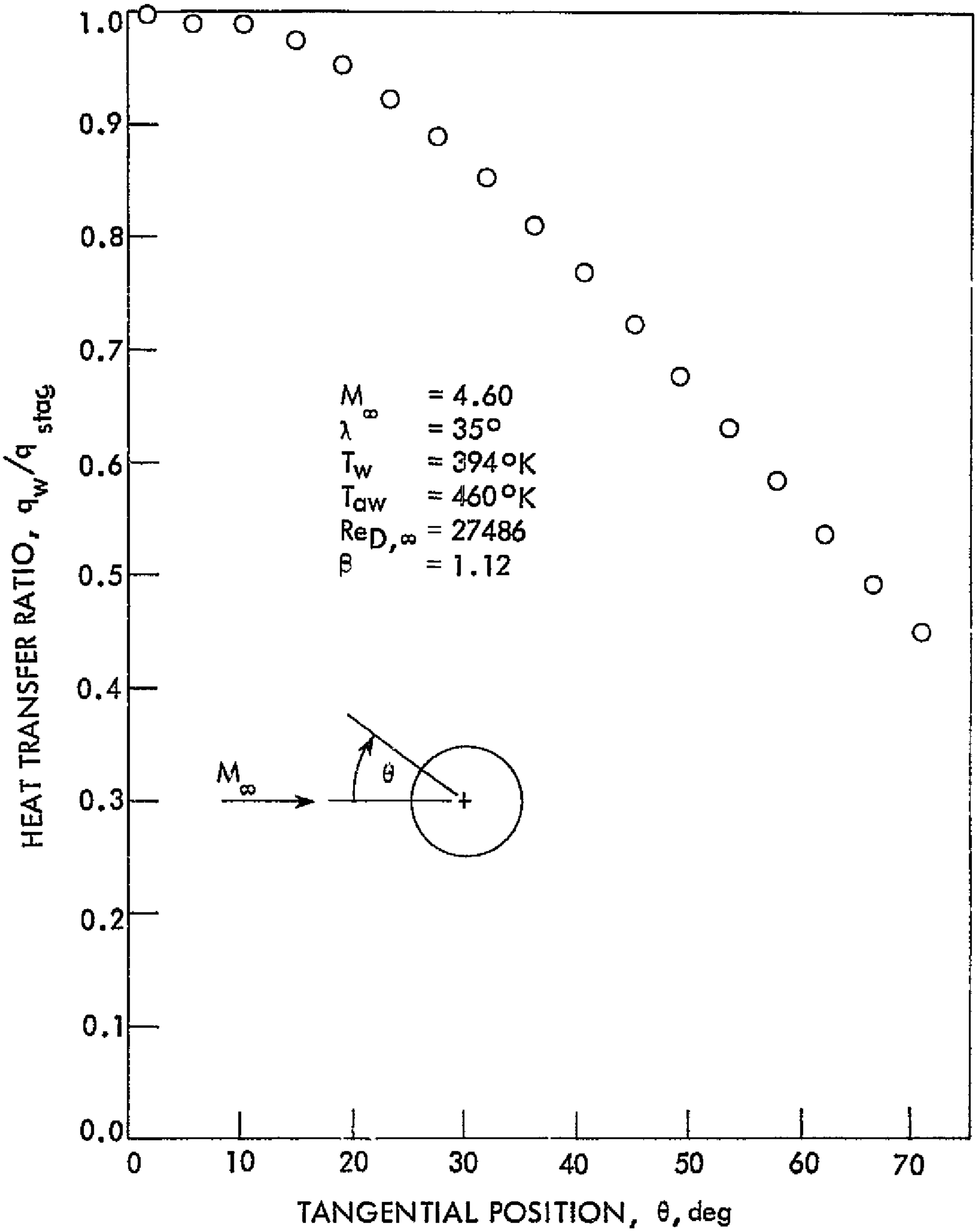

Figure 26. Heat transfer distribution on a swept infinite circular cylinder.

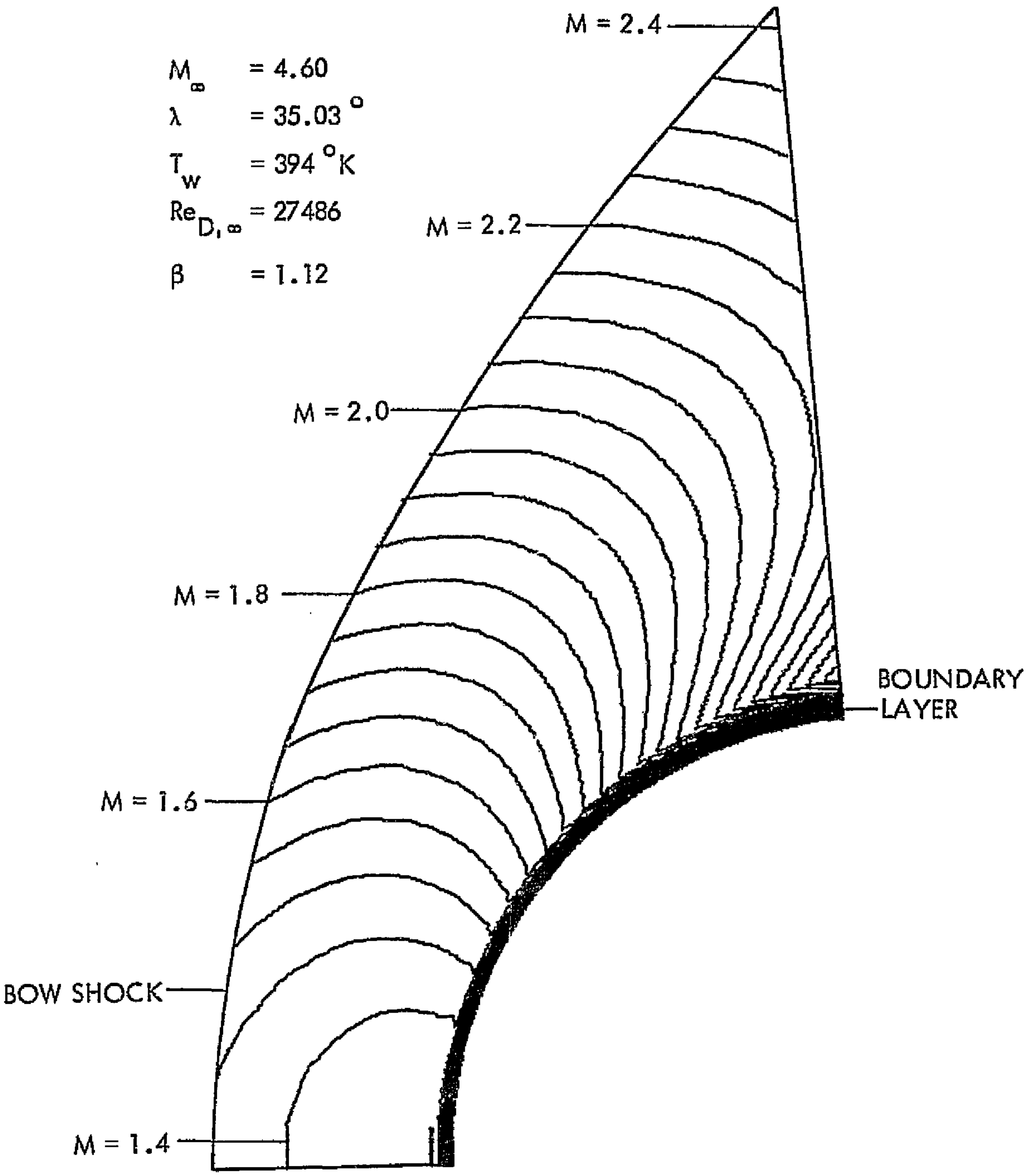

Figure 27. Mach number contours around a swept infinite circular cylinder.

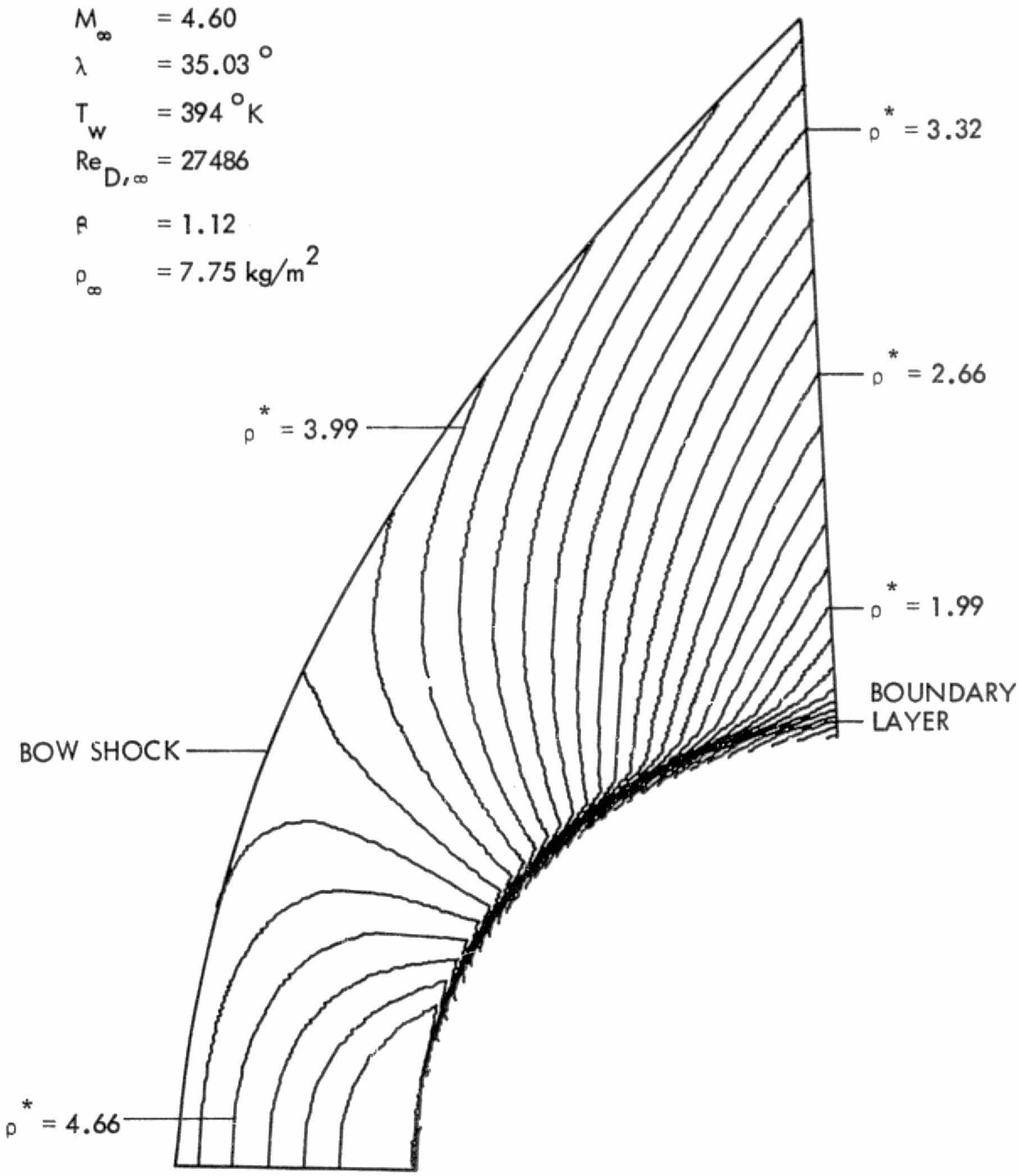

Figure 28. Density contours around a swept infinite circular cylinder.

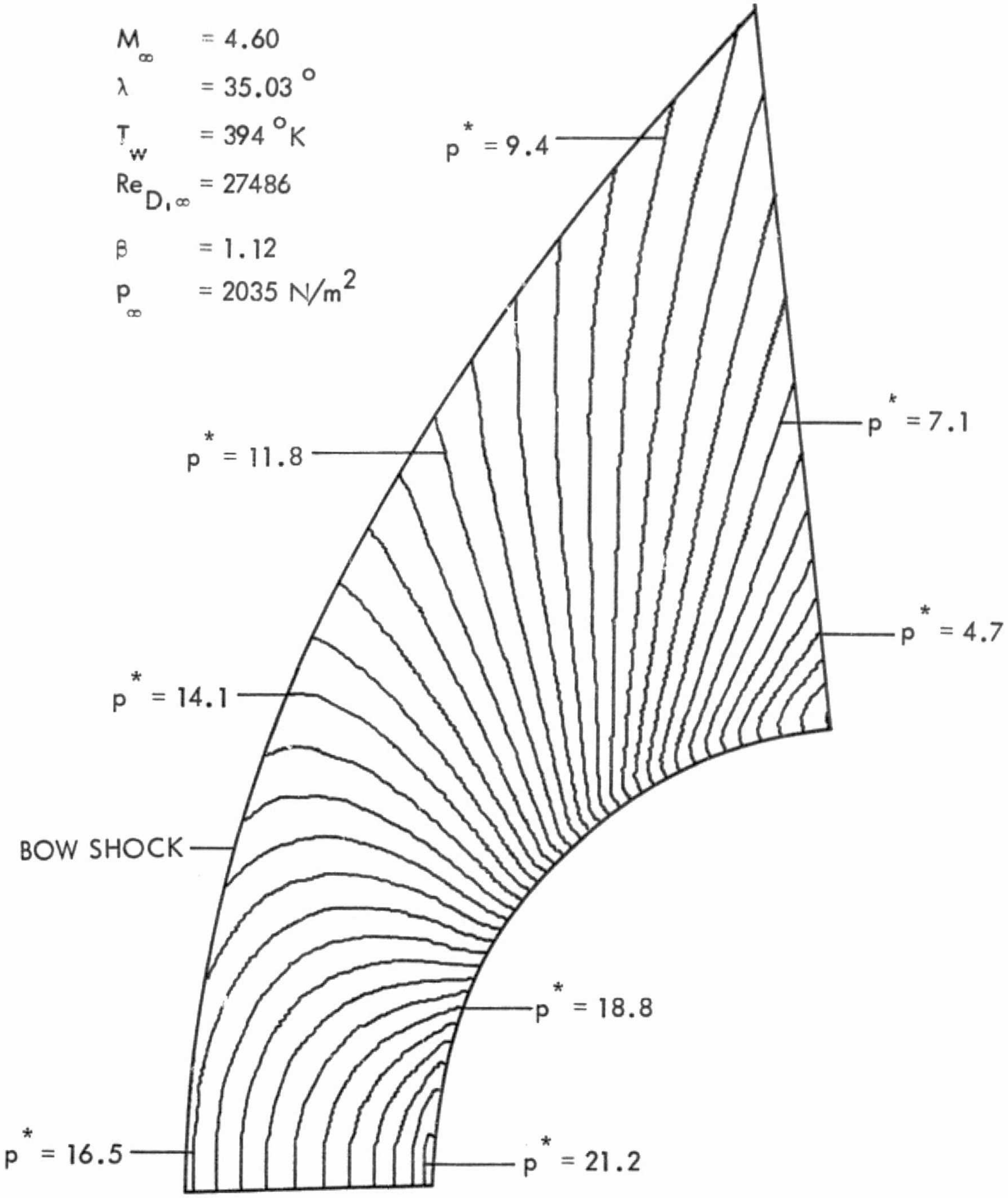

Figure 29. Pressure contours around a swept infinite circular cylinder.

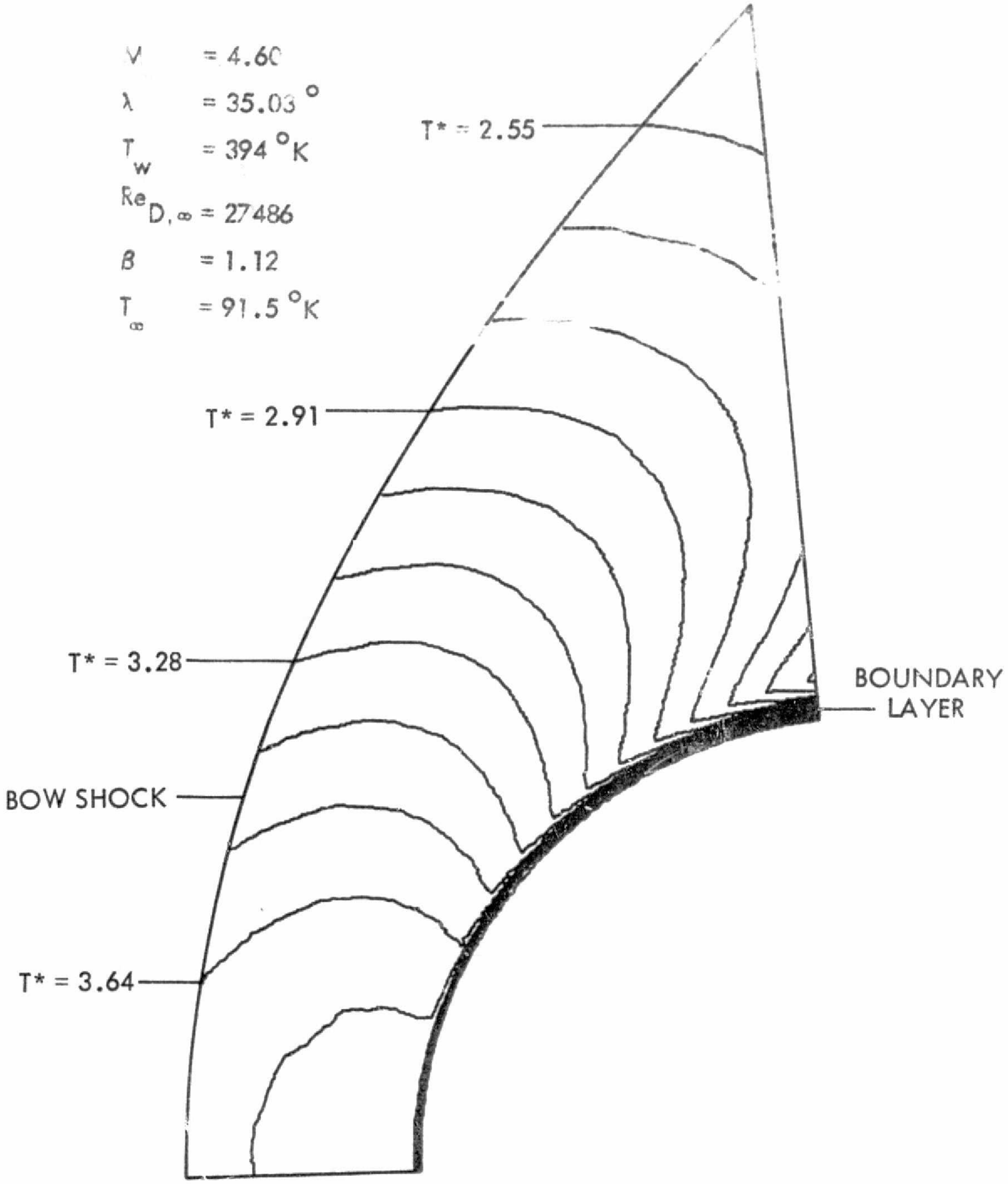

Figure 30. Temperature contours around a swept infinite circular cylinder.

conditions of the current solution. However, the stagnation line value of heat transfer can be compared with theoretical results.

The stagnation line heat transfer for a laminar boundary layer on a yawed infinite circular cylinder can be obtained from [73]

$$q_{stag} = k_\infty \frac{T_{aw} - T_w}{2D} \left(\frac{2Re_{D,\infty} \mu_{stag}}{M_\infty \mu_\infty} \right)^{1/2} \left[\frac{2T_\infty p_{stag}}{\gamma T_{stag} p_\infty} \left(\frac{p_{stag}}{p_\infty} - 1 \right) \right]^{1/4} \qquad 4.8$$

where the subscript "stag" stands for values measured along the stagnation line, k_∞ is the freestream coefficient of thermal conductivity, μ is the coefficient of viscosity computed from the Sutherland viscosity law, and T_{aw} is given as before from Equation 4.4. The value of stagnation line heat transfer computed from this formula is about 15 percent lower than the corresponding numerical value. This may be the result of not obtaining enough resolution in the boundary layer. The numerical values of wall heat transfer are computed by evaluating the slopes of the total enthalpy profiles at the wall. The slopes are approximated by three values of total enthalpy ($i = NI$, $NI - 1$, and $NI - 2$). This approximation is inaccurate for coarse mesh spacings.

Another consideration for the difference between the two results is the accuracy of the theoretical result. Beckwith and Gallagher [73] compare this theory with experimental results but for Reynolds numbers two orders of magnitude larger than the present value. In addition, only a limited number of comparisons were made between theory and experiment. In light of these considerations, the comparison between the theory and the present numerical result seems reasonable.

Contour plots of Mach number, density, pressure, and temperature for the present infinite cylinder solution are shown in Figures 27-30, respectively. These contour plots have been drawn by a computer plotter and are displayed in the physical plane. No characteristic blunt body sonic line is shown in Figure 27 because the z-component of Mach number in the shock layer is by itself supersonic. The boundary layer can clearly be seen in Figures 27, 28 and 30. Note the unusually large boundary layer thickness in the stagnation line region which is characteristic of an infinite cylinder solution. The general validity of the zero normal pressure gradient assumption can be seen from the pressure contours shown in Figure 29. The stagnation line region of Figure 29, however, does seem to suggest a nonzero normal gradient in pressure.

This concludes the infinite cylinder solution presentation. The results for the three-dimensional shock impingement solution are presented in the next section.

C. Three-Dimensional Shock Impingement Solution

An infinite cylinder solution was used to obtain the initial conditions for the three-dimensional wing-leading-edge shock impingement solution. The flow field variables in each z-plane of the three-dimensional initial solution were set equal to the flow field variables from the infinite cylinder solution. The planar impinging shock was introduced by discontinuously changing the freestream conditions across the intersection line. The solution was advanced in time by using the numerical procedure previously described until the wall pressures were changing by sufficiently small amounts.

The freestream conditions chosen for this three-dimensional shock impingement computation were

$$\begin{aligned} M_{r,\infty} &= 5.38 & p_\infty &= 559.1\ \text{N/m}^2 \\ M_{z,\infty} &= 2.51 & T_\infty &= 59.6\ {}^{\circ}\text{K} \\ Re_{D,\infty} &= 19344 & \theta &= 10^{\circ} \end{aligned} \qquad 4.9$$

where θ is the angle that the planar impinging shock makes with respect to the freestream velocity vector. For this set of freestream conditions, the pressure ratio across the impinging shock (PR) has a value of 3.6. The flow field conditions, which result after the freestream flow passes through the impinging shock, must be identical to the freestream conditions used for the infinite cylinder solution. Other conditions pertinent to this case were

$$\begin{aligned} D &= 0.025\ \text{m} & T_w &= 394\ {}^{\circ}\text{K} \\ \lambda &= 25^{\circ} & T_{aw} &= 460\ {}^{\circ}\text{K} \\ \beta &= 1.12 & \alpha &= 0.25 \\ & & c_i = c_j &= c_k = 1.0 \end{aligned} \qquad 4.10$$

where α is the smoothing coefficient for the (previously presented) bow shock smoother (see Equation 3.39) and c_i, c_j, and c_k are the coefficients for the 4th-order product smoothing terms used in conjunction with the (previously presented) finite difference method (see Equations

3.31 and 3.32). The sweep angle (λ) given in Equation 4.10 corresponds to a Type V interaction.

The three-dimensional computation was broken up into two parts. First, a coarse solution was computed in which the computational mesh consisted of 21 grid points in all three of the spacial directions. A plot of wall pressure at two different stagnation line locations (midpoint and outflow) versus time step number for this coarse solution is shown in Figure 31. Note the large fluctuations which occur initially in the solution. The solution appears converged after approximately 400 time step iterations.

Second, a refined solution was computed in which the computational mesh consisted of 21 points in both the radial and tangential directions and 41 points in the cross-flow direction. The coarse solution was used to obtain an initial condition for the refined solution. A linear interpolation was used to generate an additional z-plane of values between each already existing z-plane. Thus, the size of the physical domain in going from the coarse solution to the refined solution did not change. Instead, the number of grid points in the z-direction was doubled (Δz was halved) to improve the solution. No other changes were made. A plot of wall pressure at two different stagnation line locations (midpoint and outflow) versus time step number is shown in Figure 32. The large fluctuations in the initial portion of the solution are much smaller than for the previous case with the coarse mesh. This is probably due to the more exact initial condition solution. The solution appears converged after approximately 400 iterations.

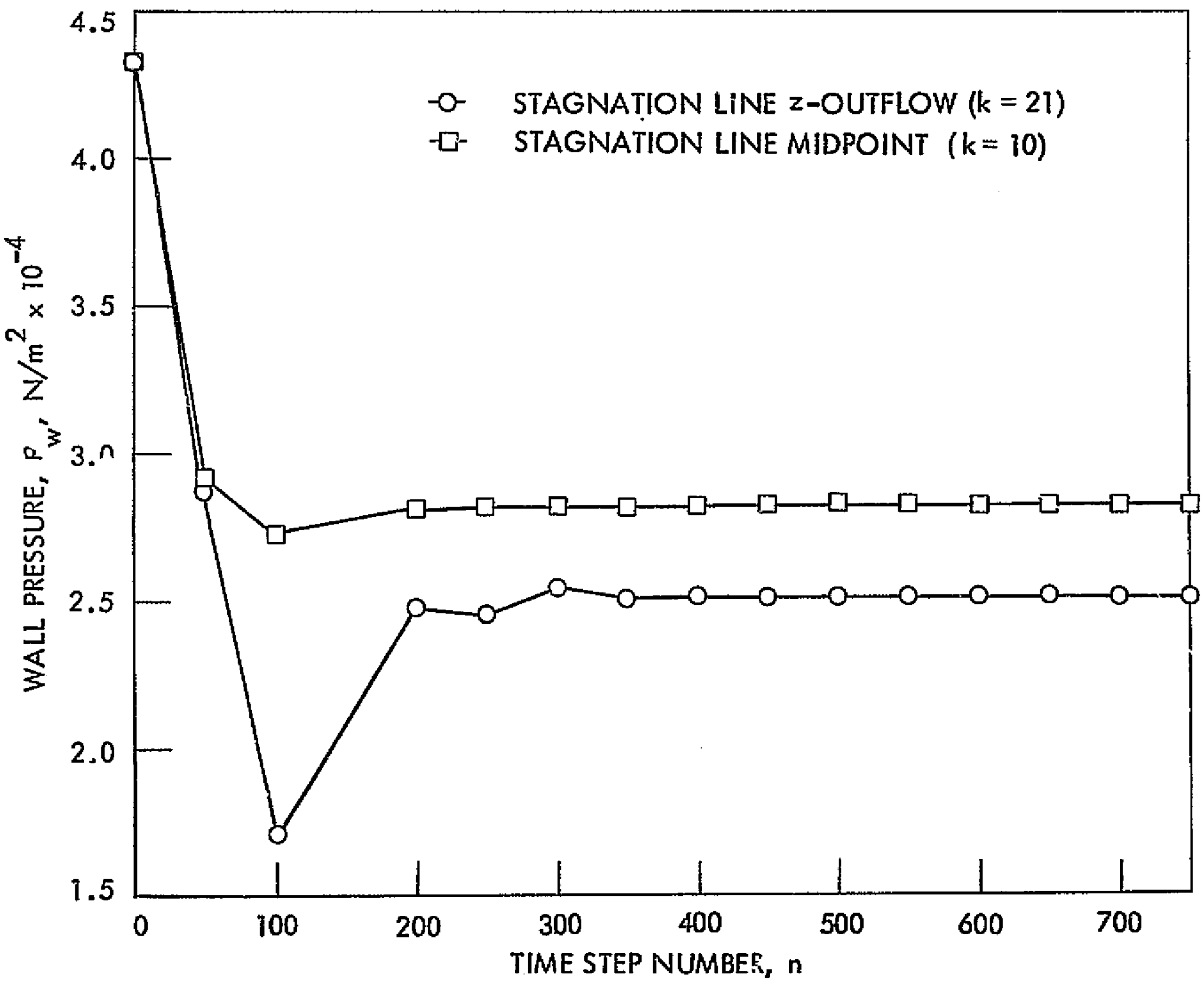

Figure 31. Time-dependent variation of wall pressure for the 21 x 21 x 21 mesh.

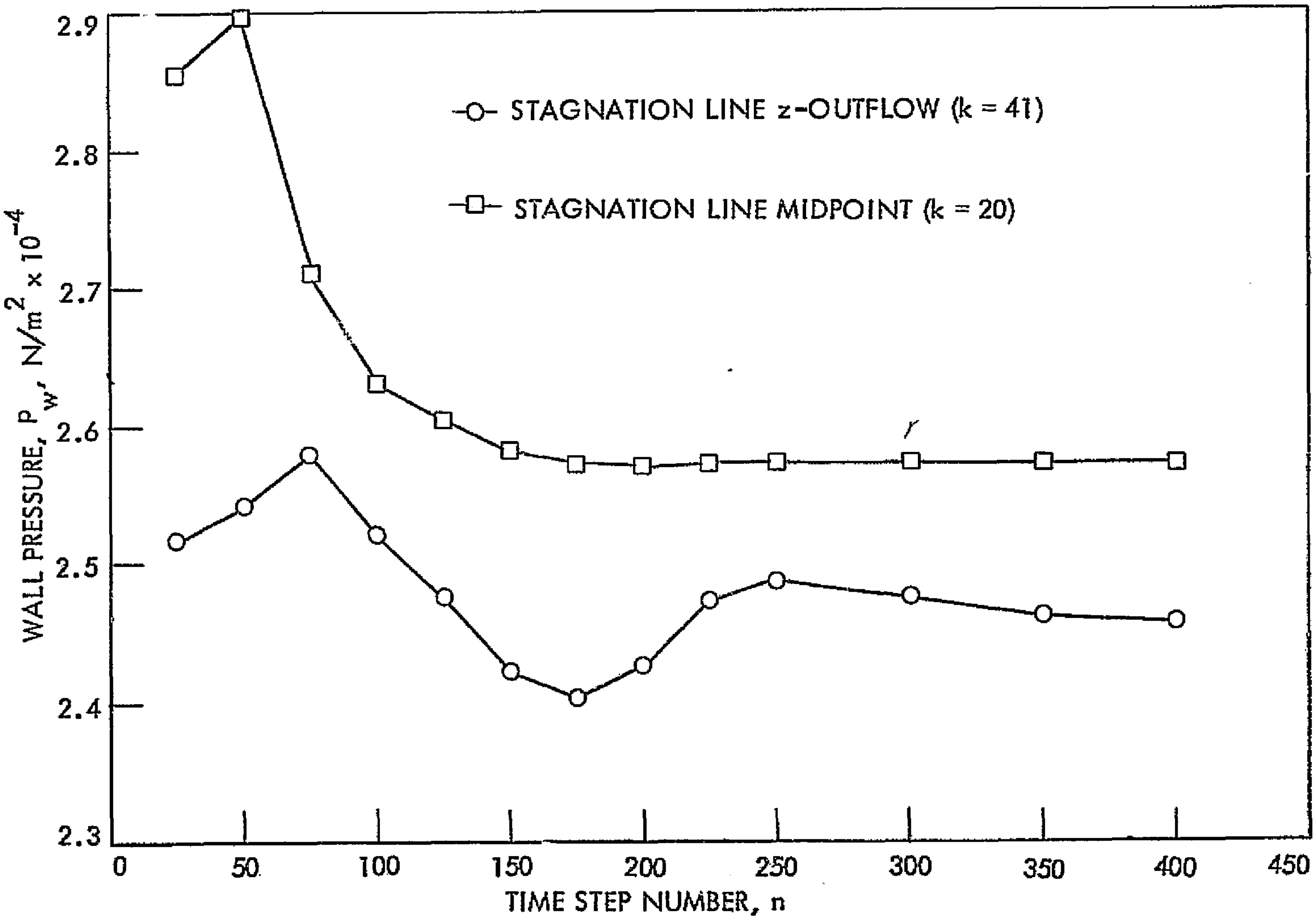

Figure 32. Time-dependent variation of wall pressure for the 21 x 21 x 41 mesh.

Because of the bow shock smoothing technique employed in the three-dimensional case, the radial shock velocities (r_{s_t}) were not able to approach zero in the vicinity of the intersection line. The shock smoothing technique, which removed erroneous numerical oscillations from the bow shock in the z-direction, also removed all desired physical "kinks." The physics of the three-dimensional problem tried to restore the physical kinks by developing large shock velocities. The bow shock, of course, did approach a steady-state position as the non-zero shock velocities and the shock smoothing approached equilibrium.

The conditions given by Equations 4.9 and 4.10 were all chosen (except for $Re_{D,\infty}$) to agree with the experiment of Keyes and Hains [2]. As with the infinite cylinder solution, the viscosity was chosen to be an order of magnitude larger to physically thicken the boundary layer and make its resolution possible with fewer grid points. In addition to increasing the boundary layer and shear layer thicknesses, this change also affected the wall shear stress and heat transfer values. Therefore, nondimensional ratios should be used when comparing these quantities with the experiment.

A comparison of the stagnation plane shock shapes is shown in Figure 33. The solid curve is the experimental result of Keyes and Hains [2] taken from a Schlieren photograph. The symbols represent the present numerical results and are plotted in such a manner that the experimental and numerical positions of the impinging shocks agree exactly. The experimental results were obtained by allowing a planar impinging shock to strike the shock layer on a finite swept cylinder. The intersection point along the stagnation plane was only three centi-

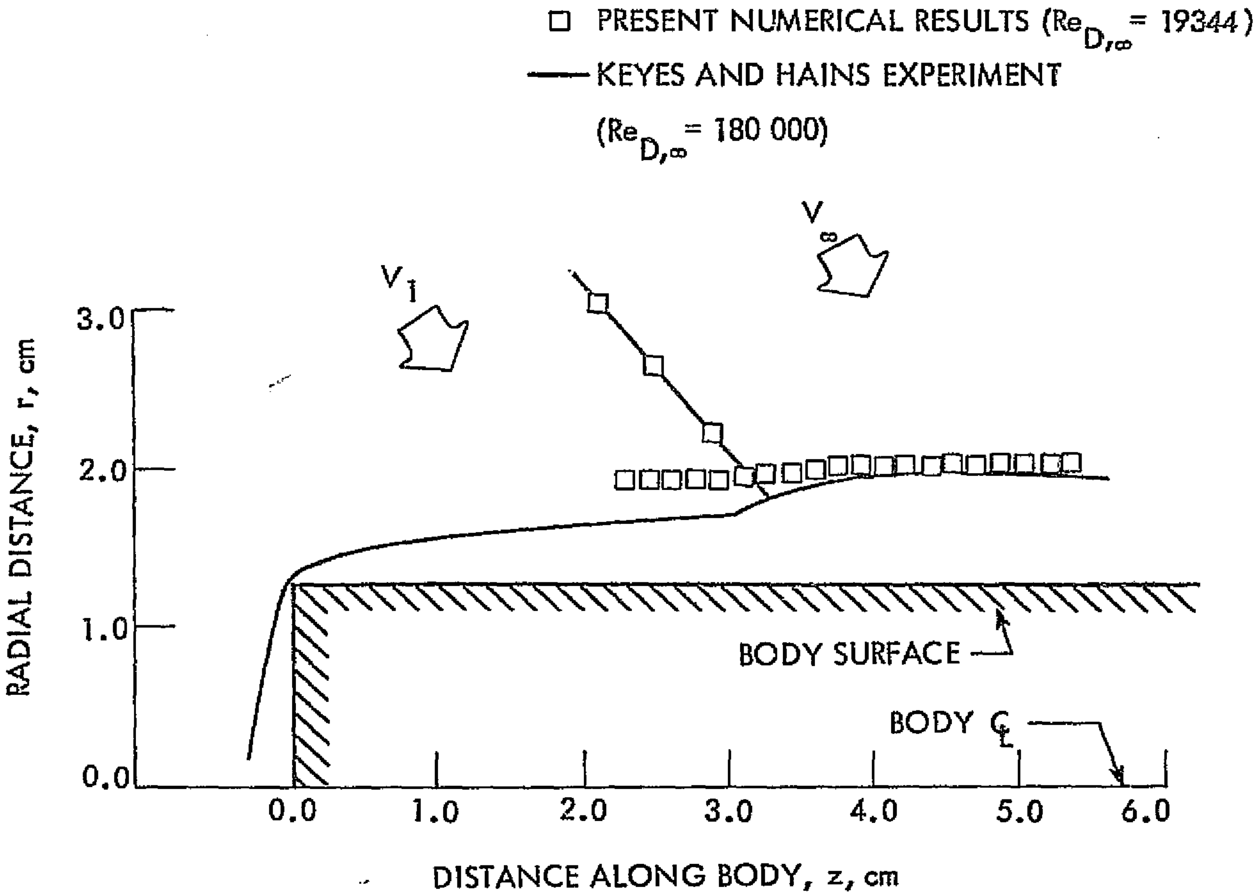

Figure 33. Stagnation plane shock shapes.

meters downstream from one end of the cylinder. The shock standoff distance for the initial numerical z-plane is therefore, much different than the corresponding value of the experimental result. When these curves are examined in light of this difference the comparison seems quite good. Note the effect of the bow shock smoothing in the numerical result. The physical kinks which appear in the experimental Schlieren photograph did not develop to the full extent in the numerical result.

A comparison of the stagnation line wall pressure is shown in Figure 34. The symbols represent the experimental results of Keyes and Hains [2] and were obtained from static pressure ports in conjunction with electrical strain-gage pressure transducers. The solid curve represents the present numerical result. The z-direction position of the numerical pressure distribution curve was determined from the shock shape comparison of Figure 33. The general trend of the comparison is quite good. However, the peak value in the experimental curve, which is caused by a boundary layer interaction with the transmitted shock, is not reproduced in the numerical results. A small peak does occur in the numerical results indicating that the transmitted shock is partially formed.

A comparison of the stagnation line heat transfer is presented in Figure 35. The symbols represent the experimental results of Keyes and Hains [2] obtained from the phase-change coating technique. The solid curve is the present numerical result. A peak in the heating rate is measured for both the numerical and experimental results although the heights of the peaks are not in good agreement. The coarse grid,

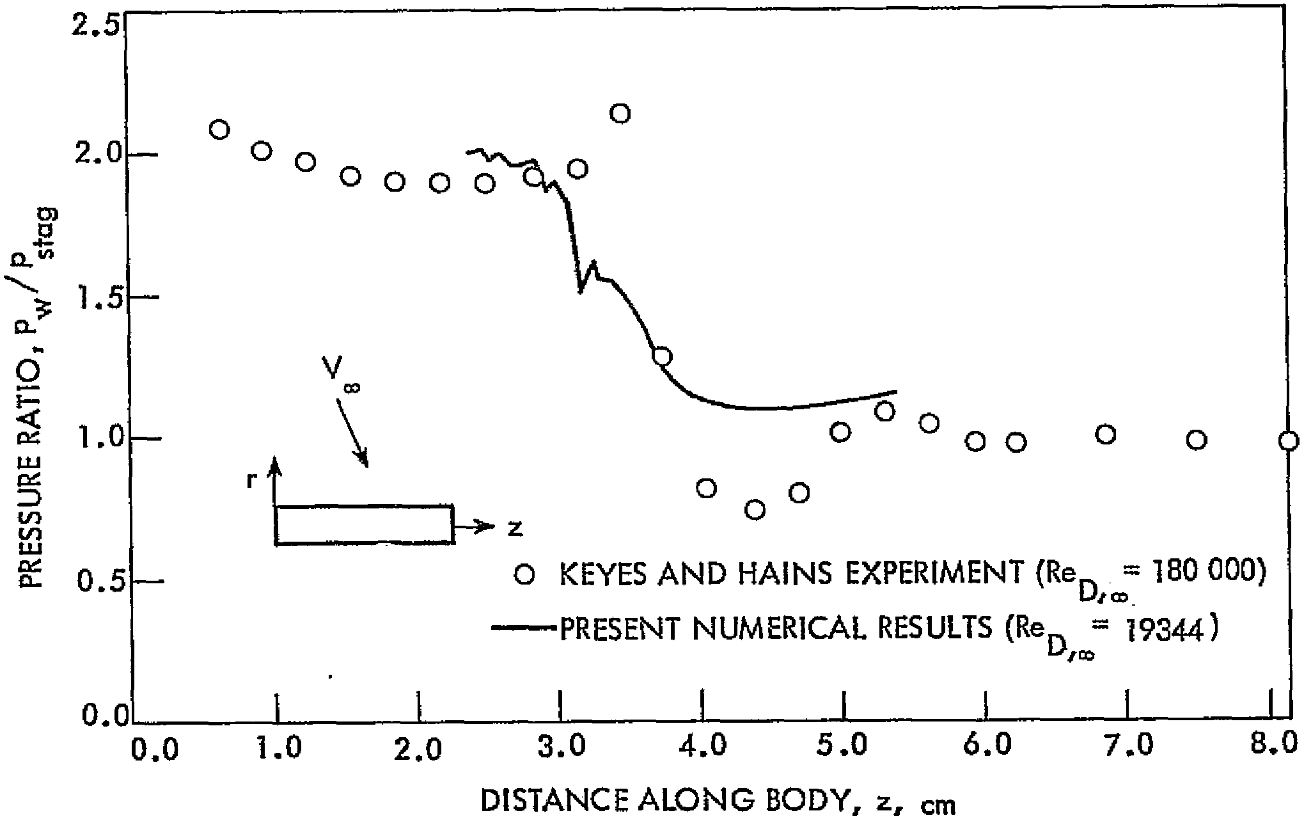

Figure 34. Stagnation line wall pressures.

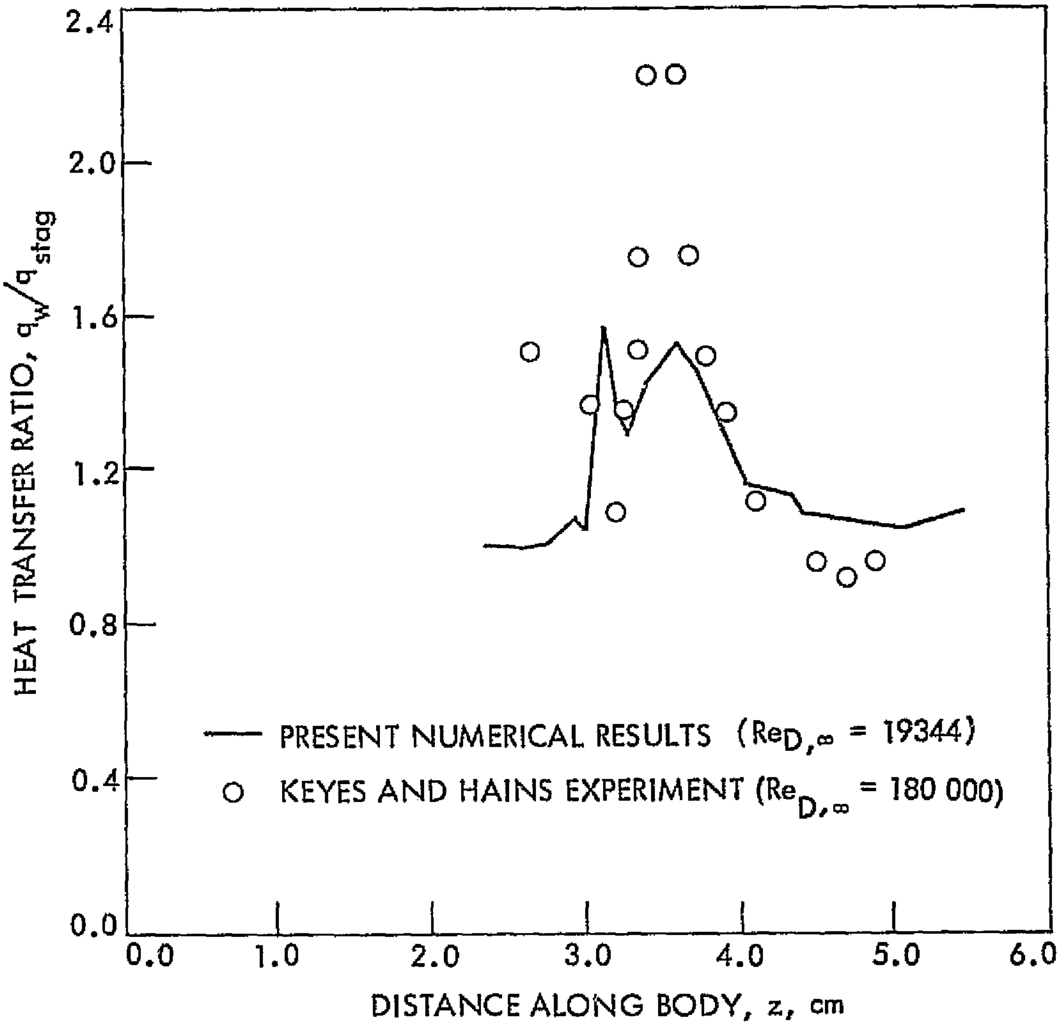

Figure 35. Stagnation line heat transfer rates.

numerical smoothing, and increased physical viscosity probably all contributed to the poor resolution of the transmitted shock and therefore, to the poor agreement.

More insight into the numerical solution can be obtained from contour plots of the important solution variables. Contour plots of Mach number, density, pressure, and temperature are shown for selected z-plane and θ-plane locations in Figures 36-50. Each of these contour plots was drawn with a computer plotter. The Mach number, density, pressure, and temperature increments were 0.05, 1.03×10^{-2} kg/m^3, 957.6 N/m^2, and 11.11 °K, respectively. The sketch in the upper left-hand corner of each contour plot figure identifies the approximate location of the plane being plotted. For clarity all plots are shown in the physical domain.

Mach number contour plots at $k = 8$, 14, 20, 28, and 36 are shown in Figures 36, 37, 38, 42, and 43, respectively. This series of contour plots shows the effect of shock impingement at various z-plane locations. The stagnation plane impingement point is between $k = 11$ and 12. Therefore, the Mach number contour plot at $k = 8$ (Figure 36) shows no sign of the impinging shock. The next five Mach number contour plots show the development of a strong shear layer which is the result of the impinging shock. The shear layer, which is seen in cross-section, emanates from the bow shock and approaches the body.

In addition to Mach number, z-plane contour plots of density, pressure, and temperature at $k = 20$ are shown in Figures 39-41, respectively. The shear layer is apparent in both the density and temperature contour plots but not pressure. An intersection point between the

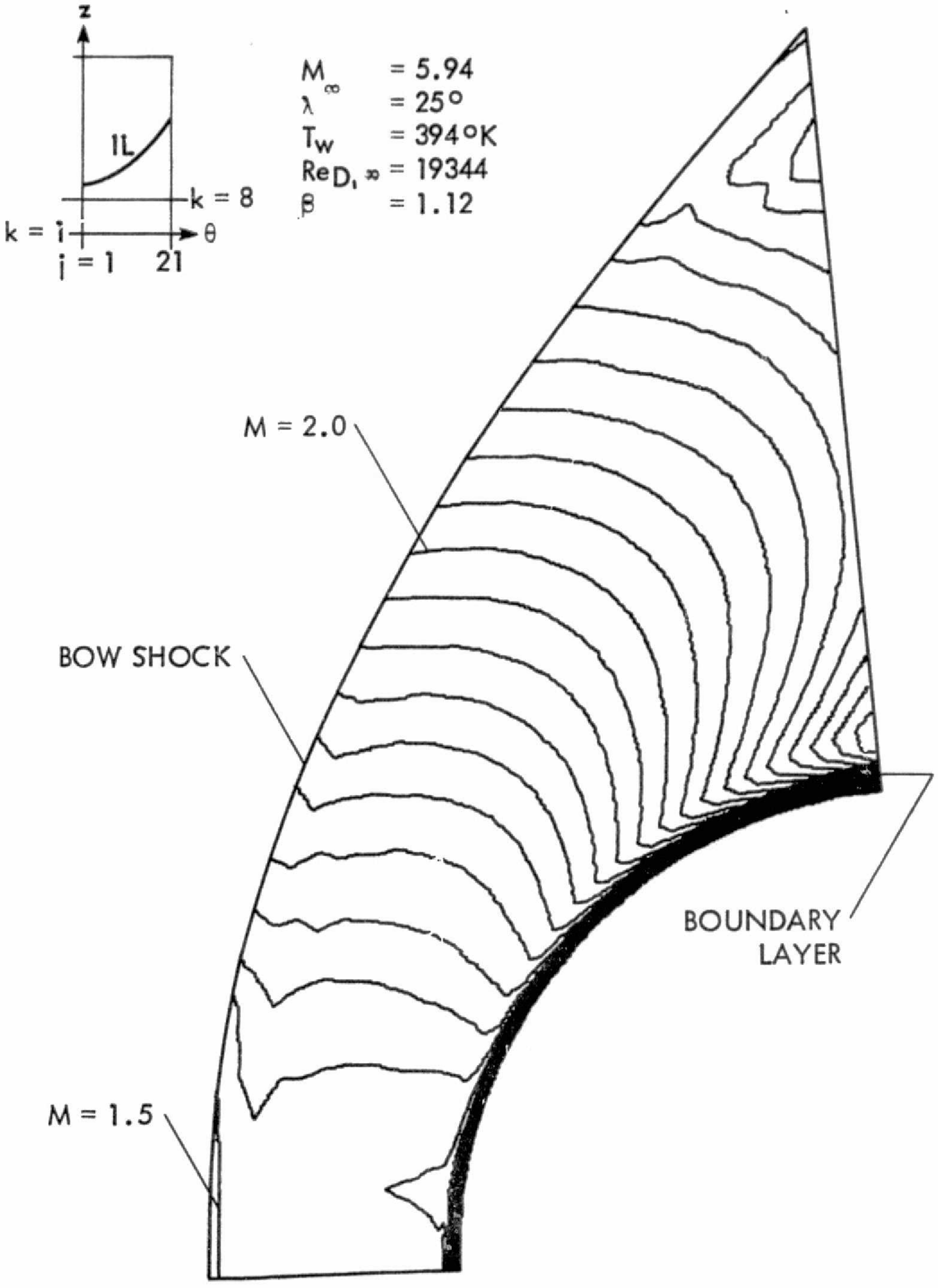

Figure 36. z-plane Mach number contours for a swept circular cylinder under the influence of an impinging shock (k = 8).

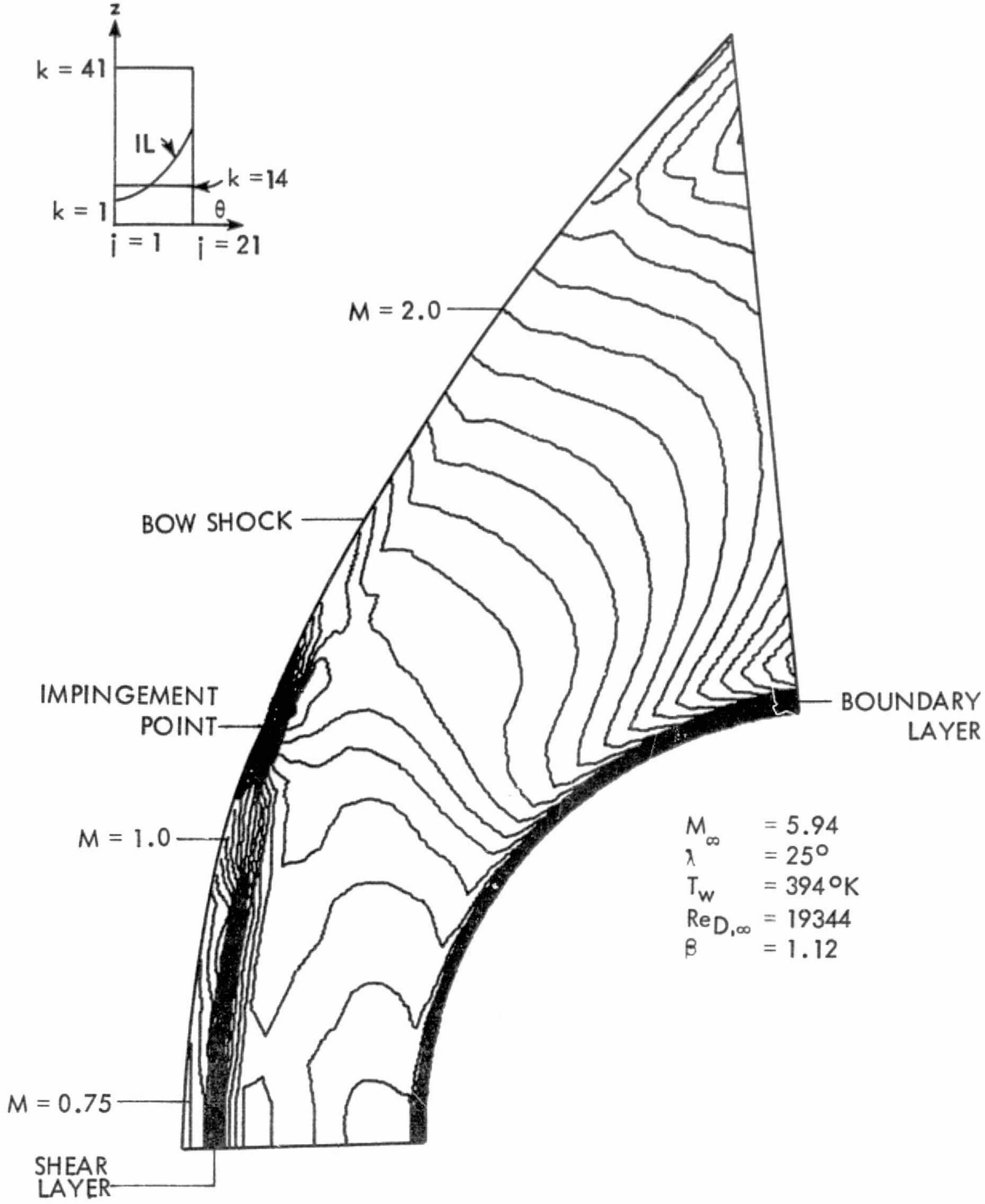

Figure 37. z-plane Mach number contours for a swept circular cylinder under the influence of an impinging shock (k = 14).

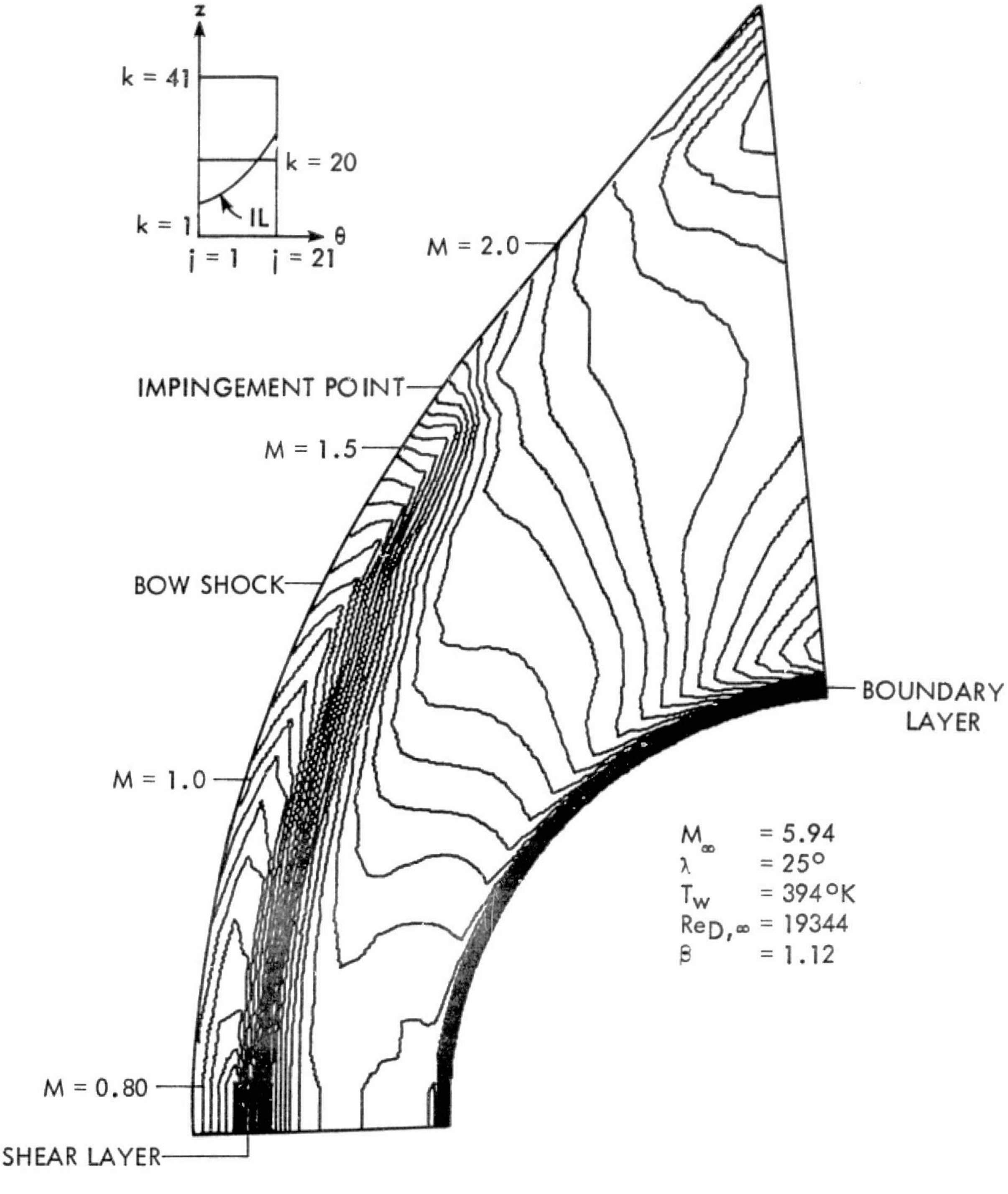

Figure 38. z-plane Mach number contours for a swept circular cylinder under the influence of an impinging shock (k = 20).

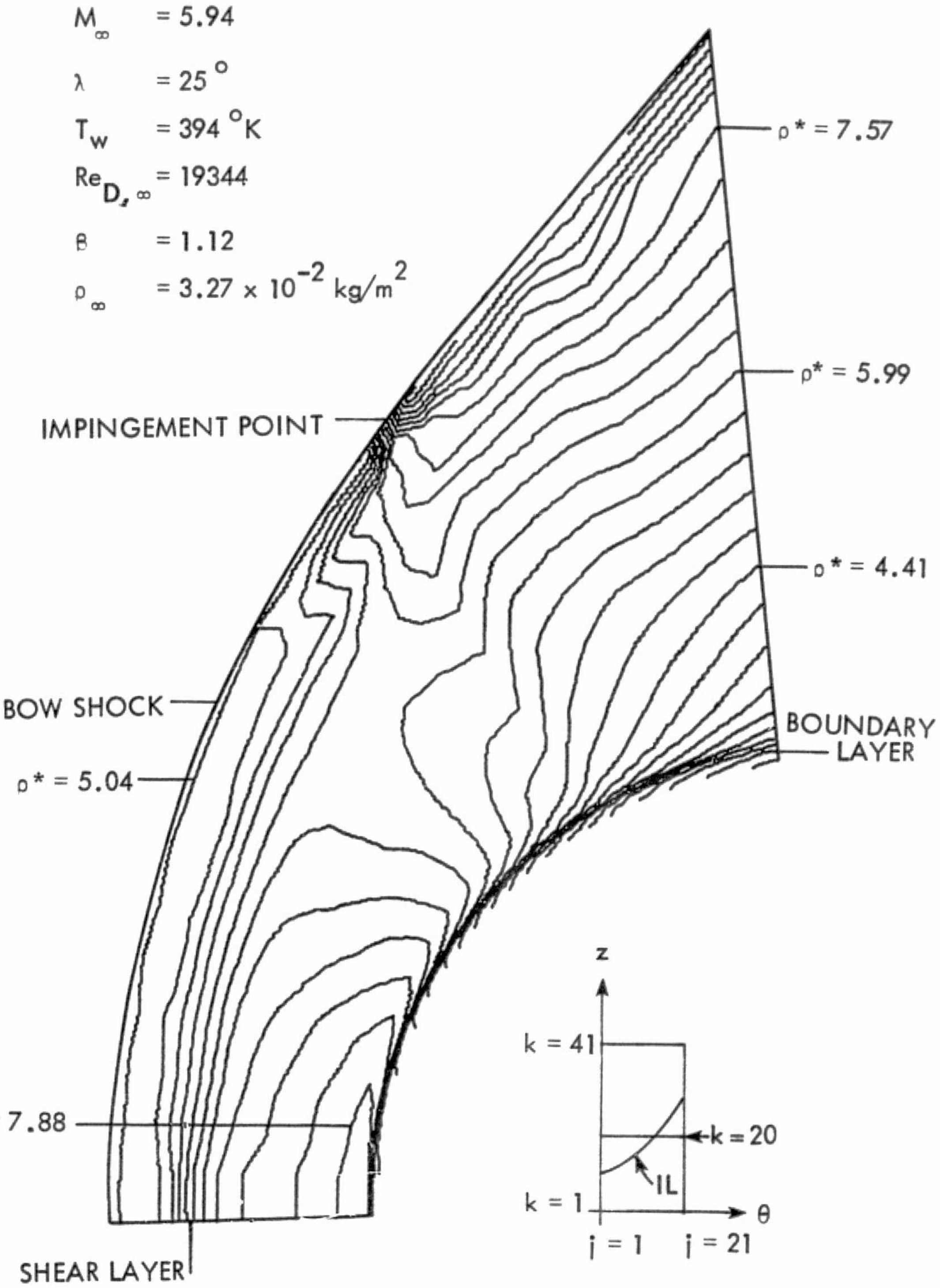

Figure 39. z-plane density contours for a swept circular cylinder under the influence of an impinging shock (k = 20).

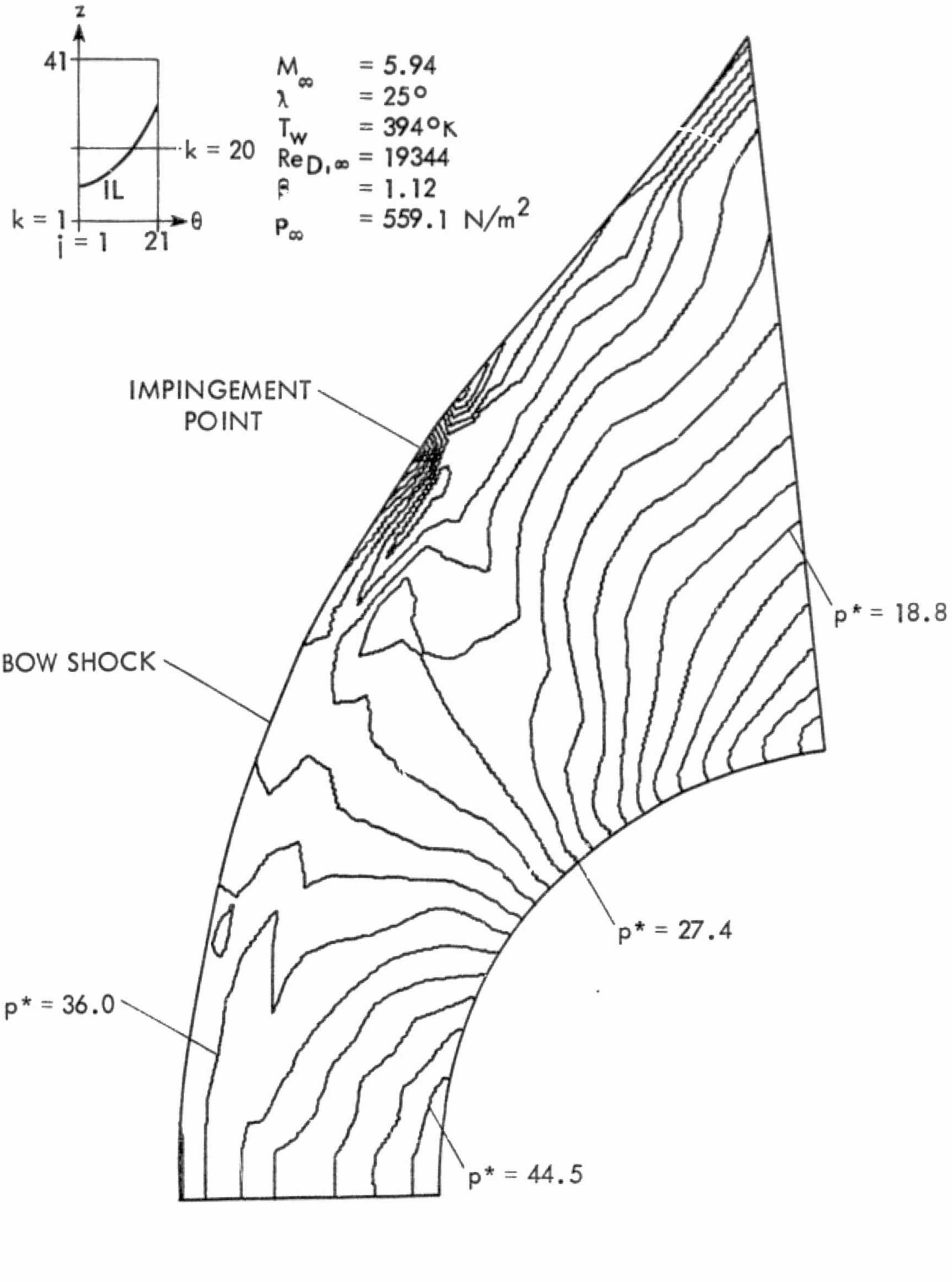

Figure 40. z-plane pressure contours for a swept circular cylinder under the influence of an impinging shock (k = 20).

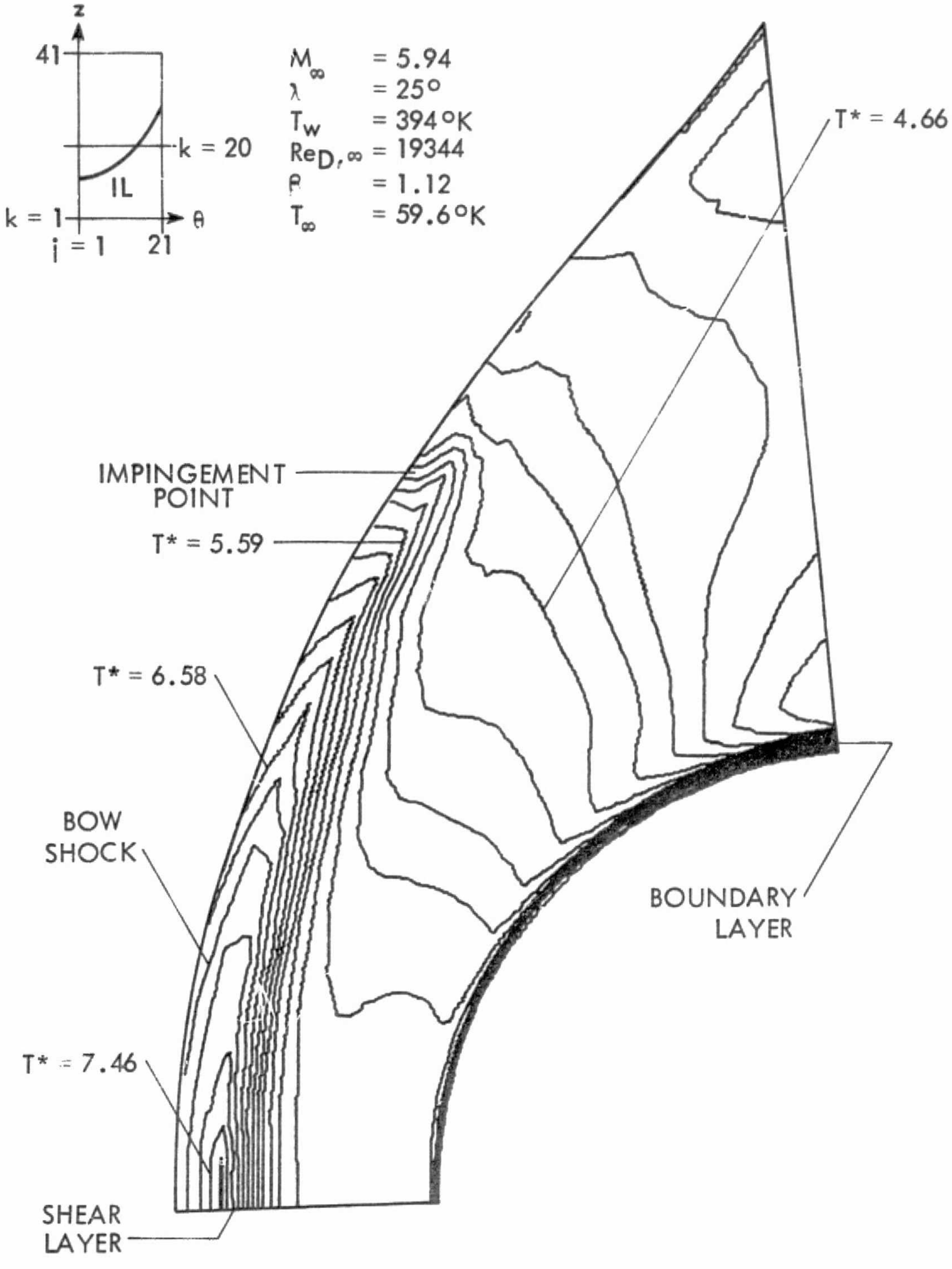

Figure 41. z-plane temperature contours for a swept circular cylinder under the influence of an impinging shock (k = 20).

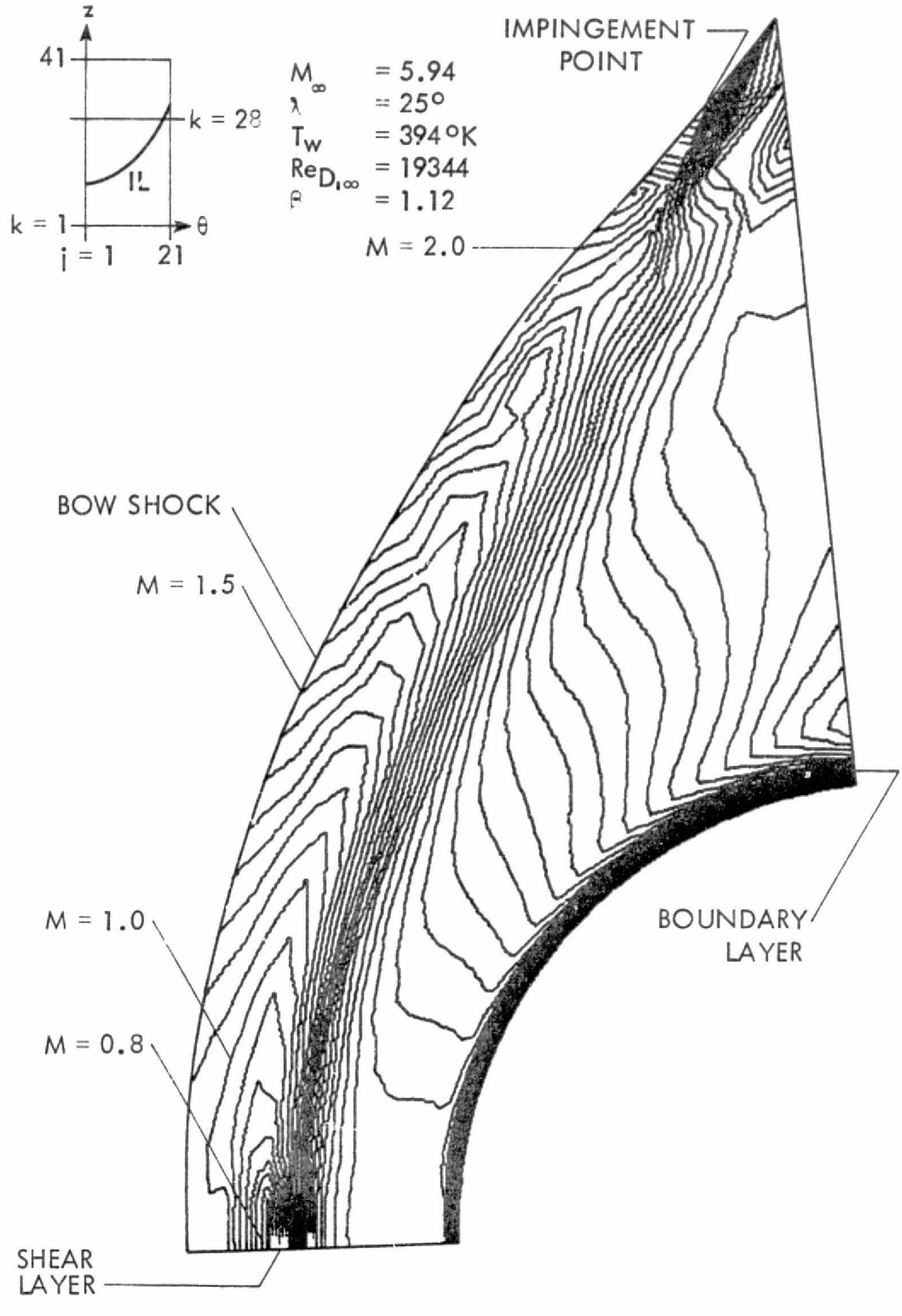

Figure 42. z-plane Mach number contours for a swept circular cylinder under the influence of an impinging shock (k = 28).

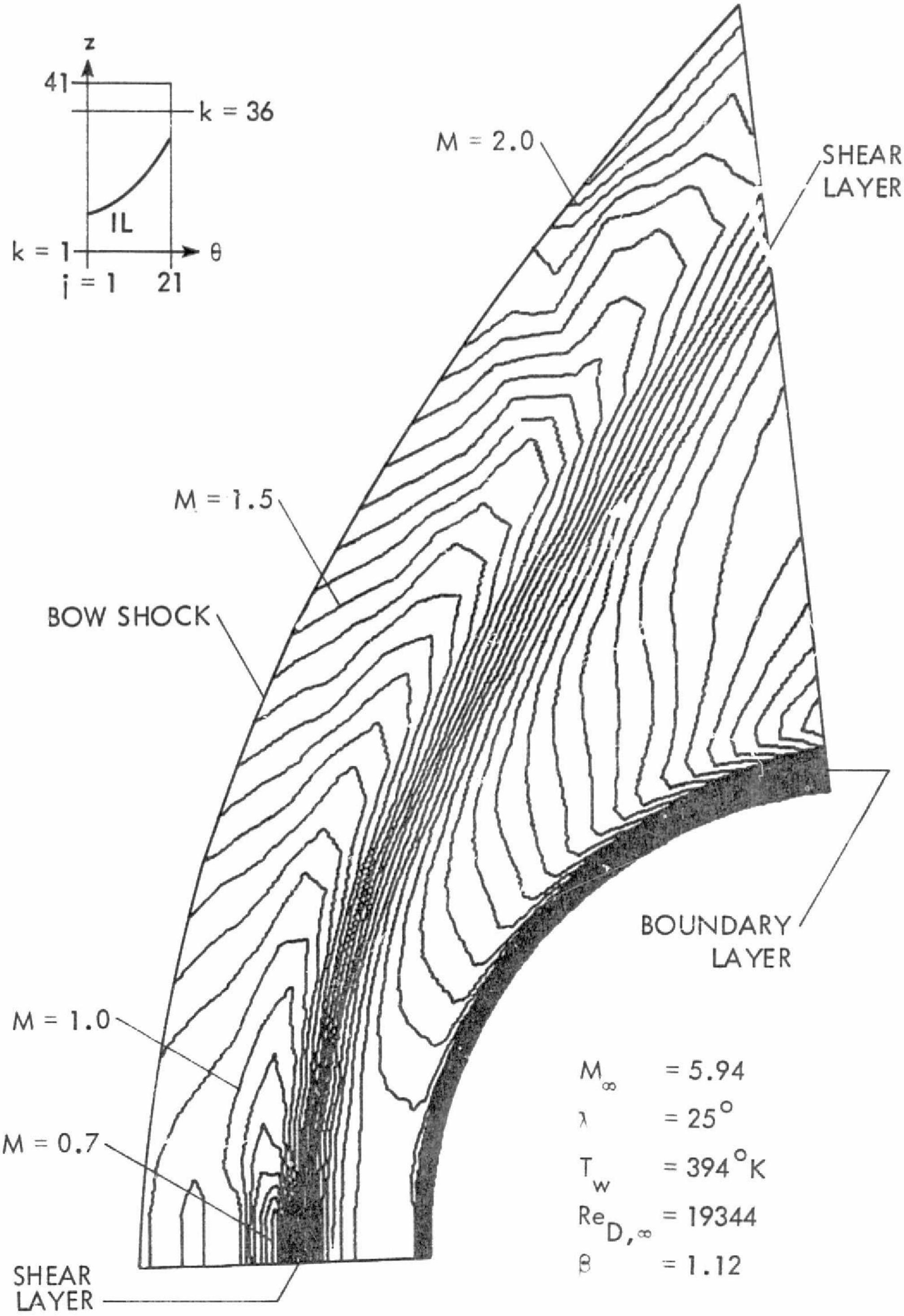

Figure 43. z-plane Mach number contours for a swept circular cylinder under the influence of an impinging shock (k = 36).

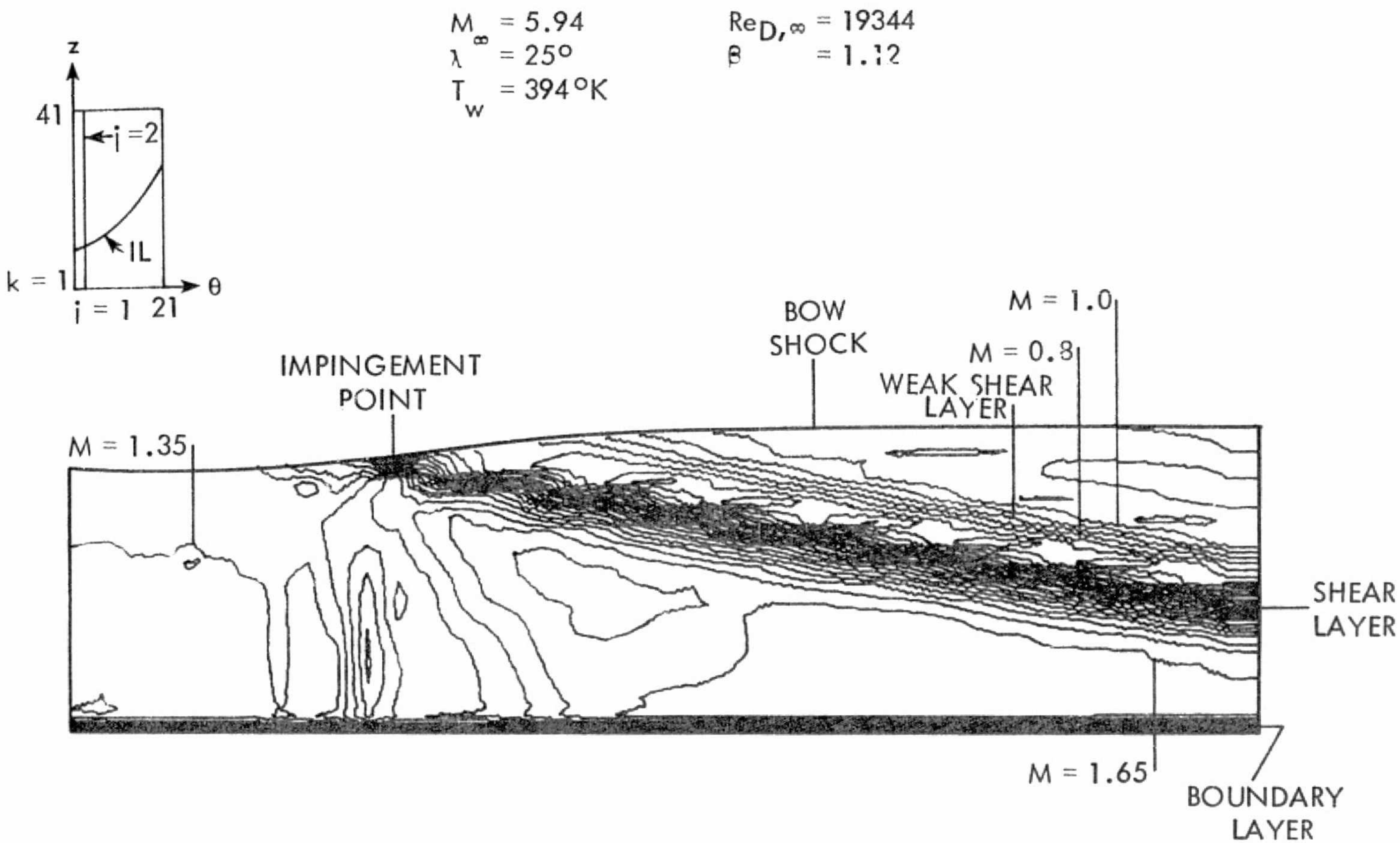

Figure 44. θ-plane Mach number contours on a swept circular cylinder under the influence of an impinging shock (j = 2).

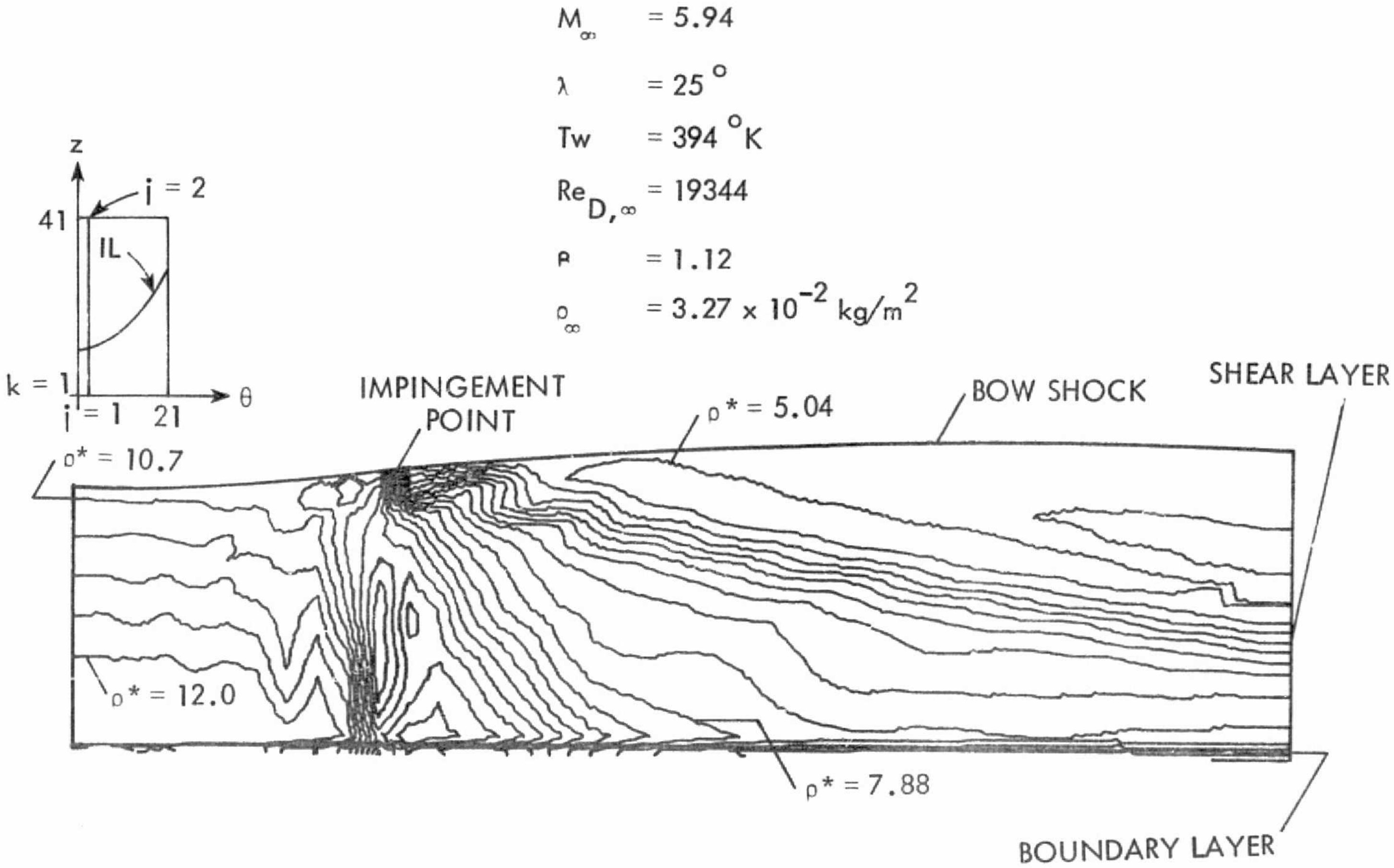

Figure 45. θ-plane density contours on a swept circular cylinder under the influence of an impinging shock ($j = 2$).

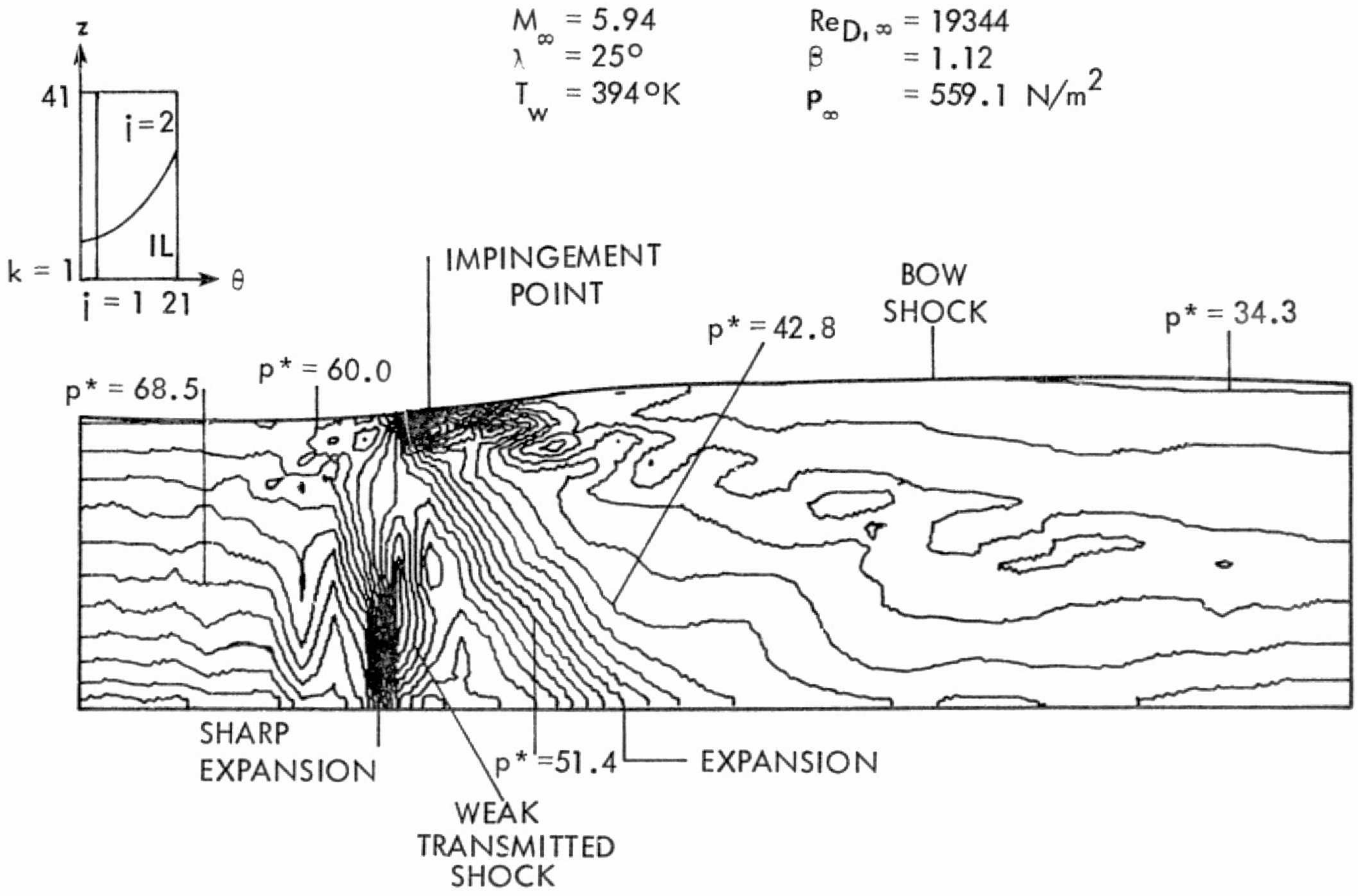

Figure 46. θ-plane pressure contours on a swept circular cylinder under the influence of an impinging shock (j = 2).

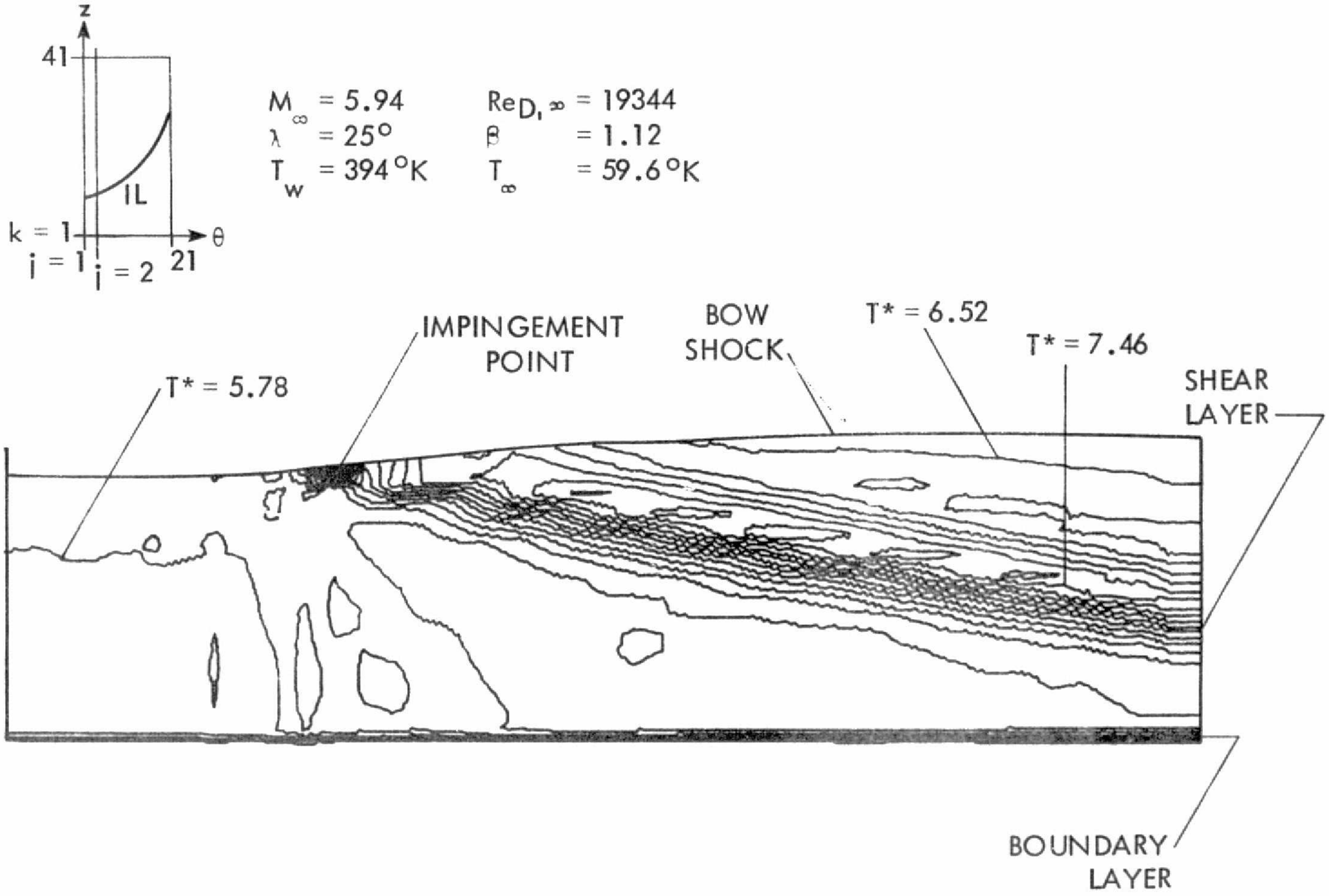

Figure 47. θ-plane temperature contours on a swept circular cylinder under the influence of an impinging shock (j = 2).

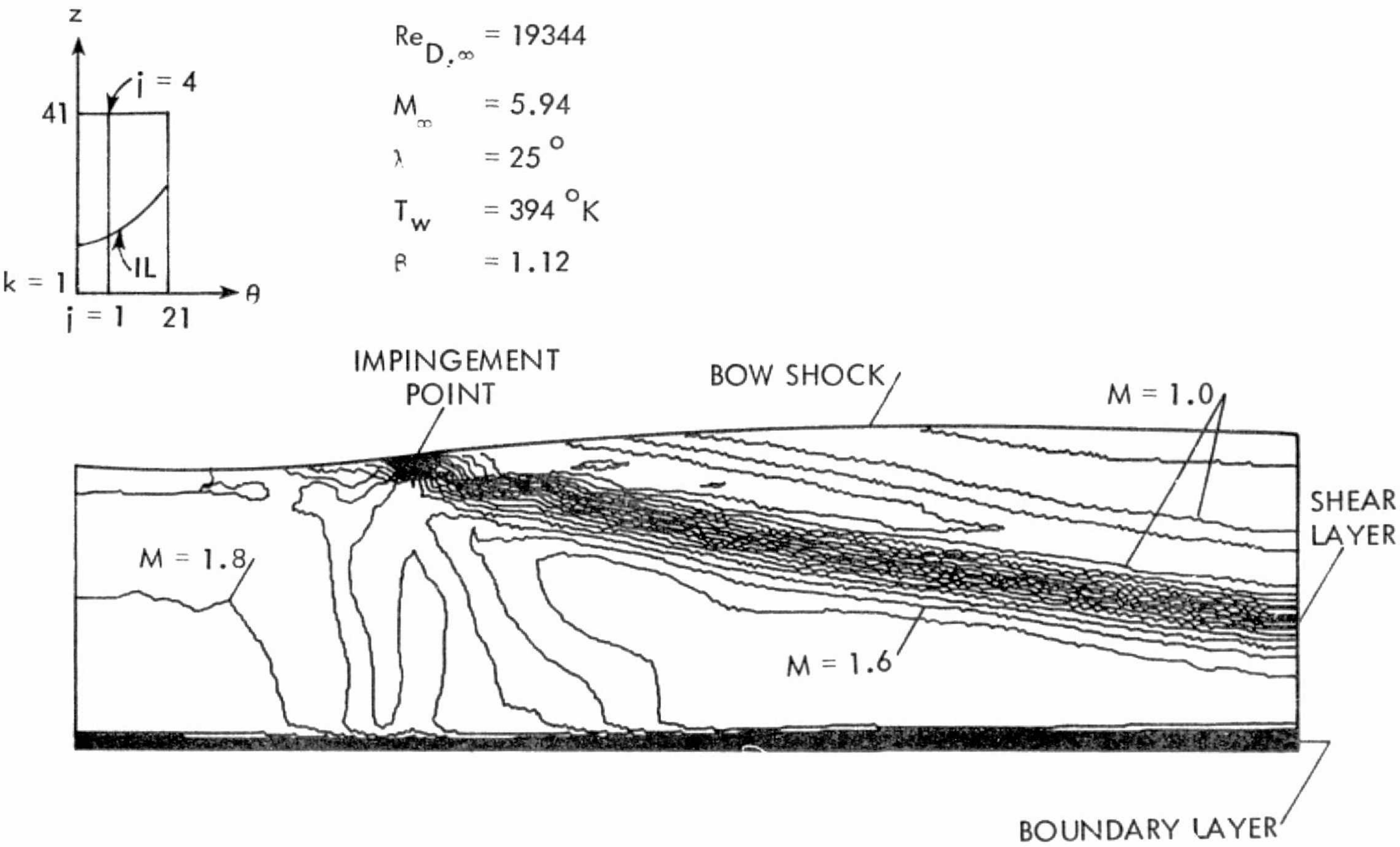

$Re_{D,\infty} = 19344$

$M_\infty = 5.94$

$\lambda = 25^\circ$

$T_w = 394\ ^\circ K$

$\beta = 1.12$

Figure 48. θ-plane Mach number contours on a swept circular cylinder under the influence of an impinging shock (j = 4).

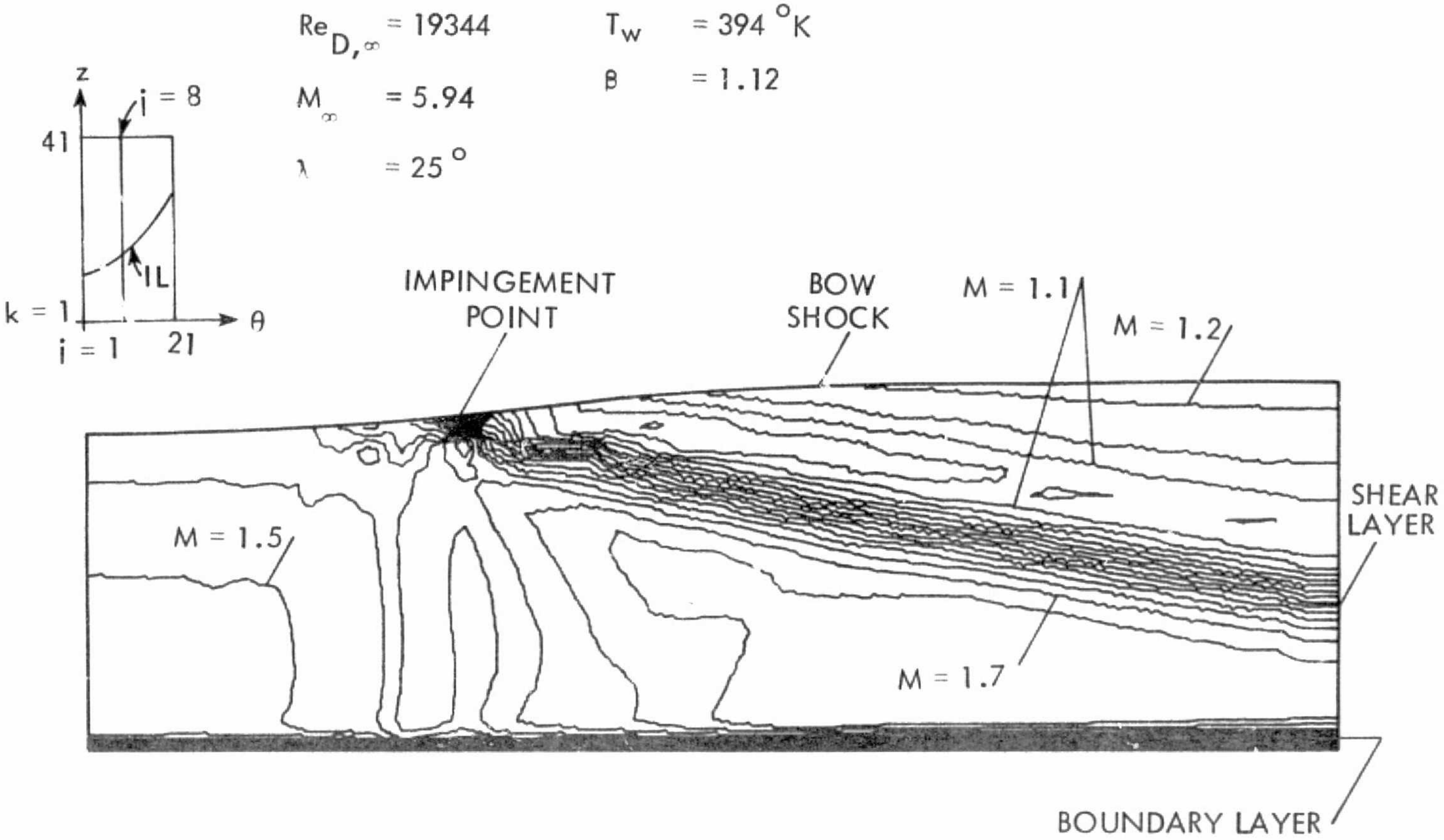

Figure 49. θ-plane Mach number contours on a swept circular cylinder under the influence of an impinging shock (j = 8).

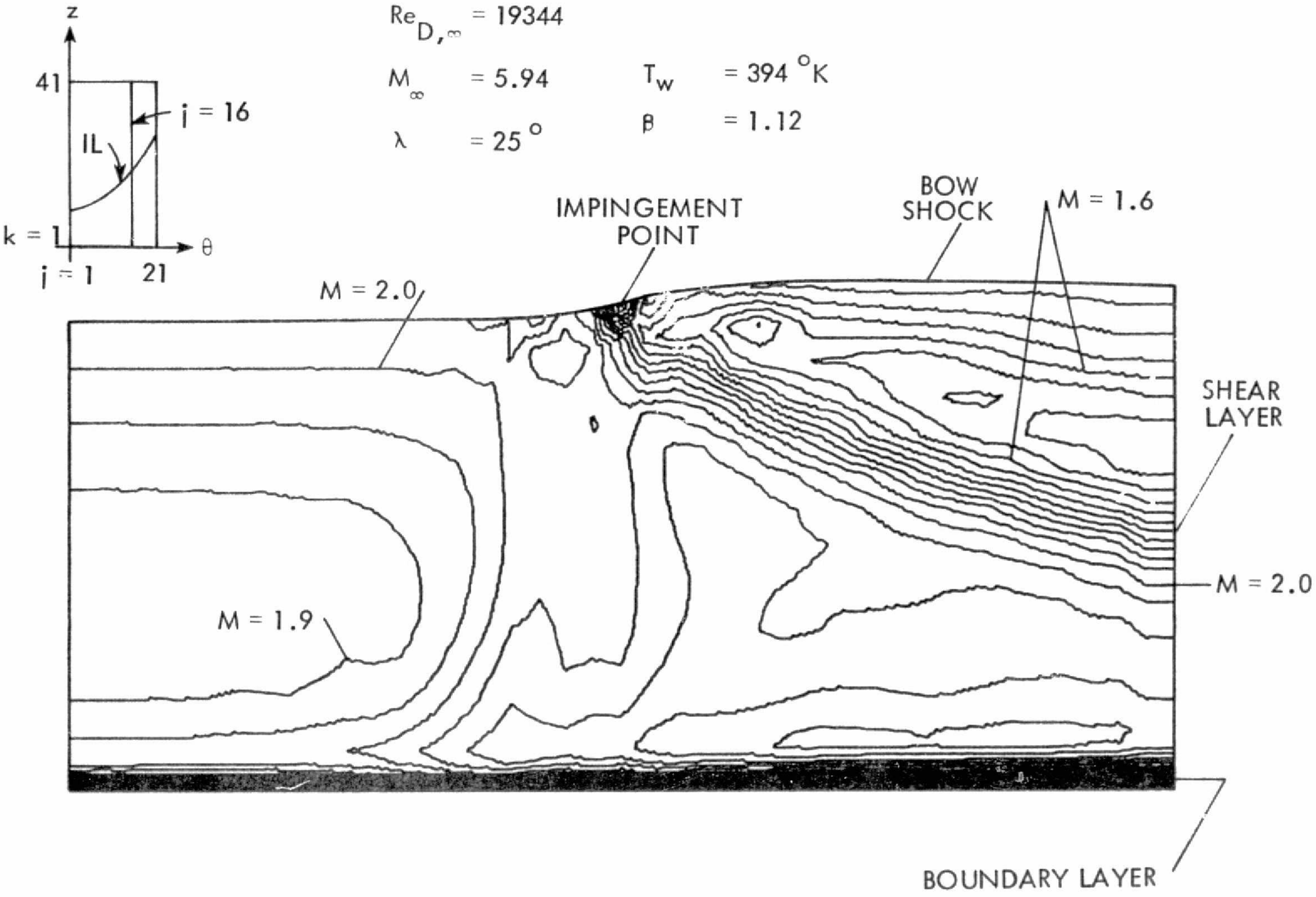

Figure 50. θ-plane Mach number contours on a swept circular cylinder under the influence of an impinging shock (j = 16).

planar impinging shock and the bow shock is quite apparent in several of the z-plane contour plots ($k = 14$, 20, and 28). Of course, no intersection point appears in the z-plane contour plots at $k = 8$ or 36, because the range of the intersection line only extends from $k = 12$ to $k = 30$. The effect of the zeroth-order extrapolation on the θ-outflow boundary condition at $i = 1$ and 2 is seen in most of the z-plane contour plots (bow shock vicinity of the θ-outflow). As pointed out earlier, this boundary condition was employed to prevent extrapolation across the sharp gradient in the flow near the intersection line. Although it succeeds in this respect, it also introduces an inconsistent region in the flow field.

Mach number contour plots at $\theta = 2.1^{\circ}$ ($j = 2$, stagnation plane), 10.7° ($j = 4$), 27.9° ($j = 8$), and 62.3° ($j = 16$), are shown in Figures 44, 48, 49, and 50, respectively. The flow field structure is best studied from these θ-plane contour plots. The strong shear layer produced by the shock impingement appears as a dark band of coalesced contour lines. This shear layer emanates from the bow shock near the intersection line, approaches the body, and finally, passes through the z-outflow boundary.

A secondary coalescence of contour lines (Figure 44) which represents another (weaker) shear layer, lies between the bow shock and the first shear layer. An inspection of the numerical output shows that the flow field between these two shear layers is subsonic. This region of subsonic flow exists only for small values of θ. The extent of the subsonic flow region can be seen in the z-plane Mach number contour plots (Figures 37, 38, 42, and 43). Further inspection of the numerical output reveals a weak jet existing just above the weak shear layer. Both the jet and the weak shear layer follow the stronger shear layer (in a parallel manner) through the z-outflow boundary.

In addition to Mach number, θ-plane contour plots of density, pressure, and temperature at $\theta = 2.1^\circ$ $(j=2$, stagnation plane) are shown in Figures 45-47, respectively. As expected, the strongest shear layer is apparent in both the density and temperature θ-plane contour plots but not the pressure.

A feature of the flow field which is apparent in the density and pressure θ-plane contour plots is the initial formation of the transmitted shock. The darkest coalescence of density or pressure contours, which is approximately perpendicular to the body represents a very sharp expansion. The vertical contour lines immediately downstream of the sharp expansion are the beginnings of a transmitted shock. Still further downstream is another (weaker than the first) expansion. The sharp expansion, followed by a slight pressure jump and then another expansion can best be visualized by referring back to Figure 34 which is a plot of stagnation line wall pressure.

Other noteworthy aspects of the θ-plane contour plots include the boundary layer, the thickening of the shock layer for increasing values of θ, and the approximate validity of the zeroth-order extrapolation for the z-outflow boundary condition.

A Schlieren photograph of a Type V shock impingement on a swept circular cylinder is shown in Figure 51. This experimental result is due to Keyes and Hains [2]. The conditions given in Equations 4.9 and

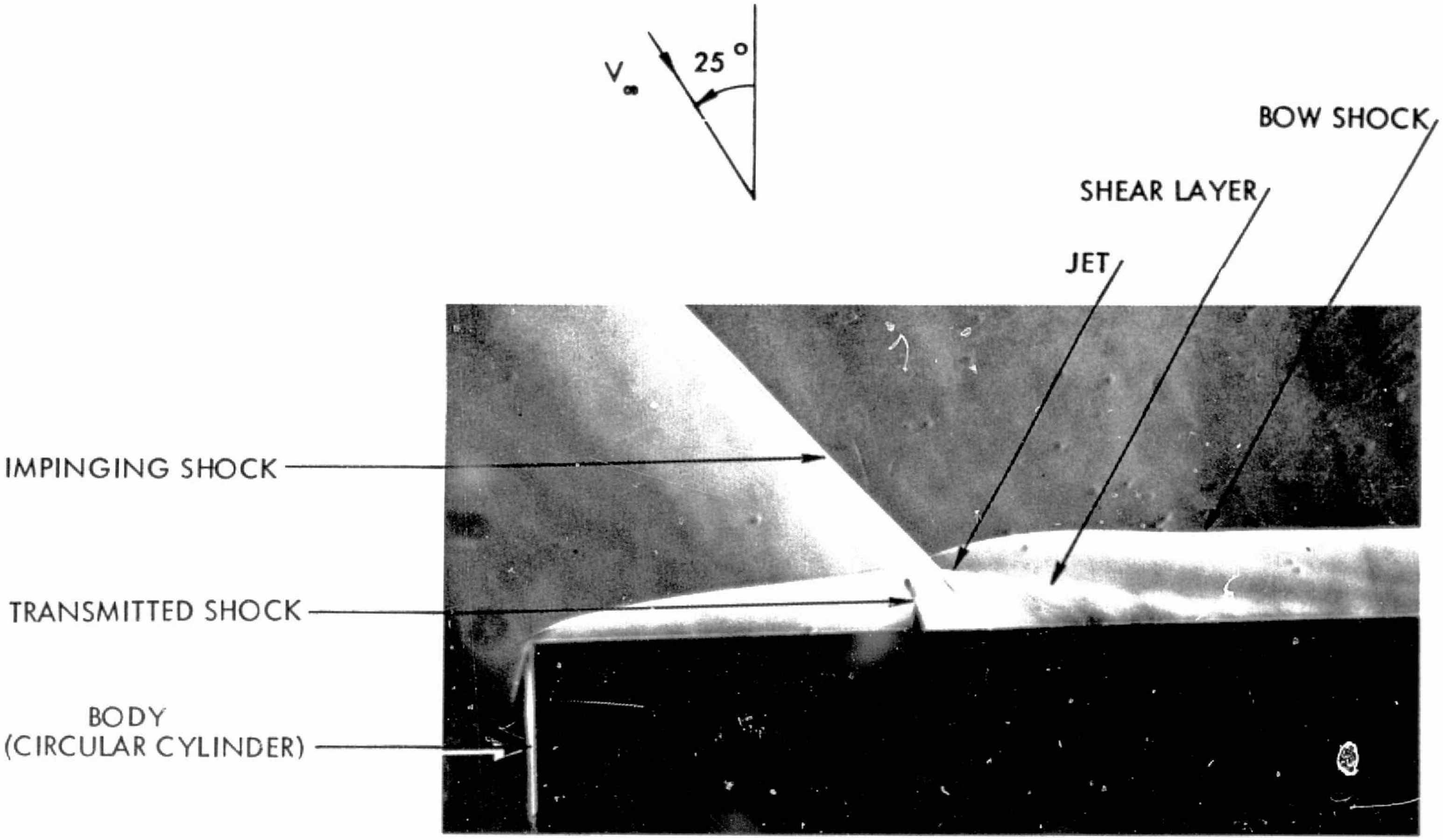

Figure 51. Schlieren photograph of a type V shock interference (Keyes and Hains)

4.10 (except, of course, the freestream Reynolds number) were chosen to match this experiment. Note the existence of the transmitted shock, the shear layer, and the jet. The development of the shock layer from the end of the cylinder is also shown in this photograph.

The failure of the numerical method to more adequately predict the transmitted shock is due largely to the coarse mesh. Another contributing factor is the bow shock smoothing which keeps the two bow shock kinks from forming. This in turn directly affects the shock layer detail especially the transmitted shock.

Contour plots of the wall pressure and heat transfer are shown in Figures 52 and 53, respectively. The overall effect of the shock impingement at the wall is seen quite vividly from these figures. The peak in the heat transfer moves around the body in much the same fashion as the intersection line on the bow shock. The effects of the shock impingement are largest at the stagnation line and diminish in the tangential direction until little change from the infinite cylinder solution is experienced at the θ-outflow boundary.

D. Computational Statistics

The two most important computational statistics associated with the solution of any problem by a finite-difference technique are the execution time and the storage requirements. The execution time, for the most part, determines the cost of the computation. The storage requirement determines the size of the computer needed for the computation. The storage requirement directly limits the computational mesh and

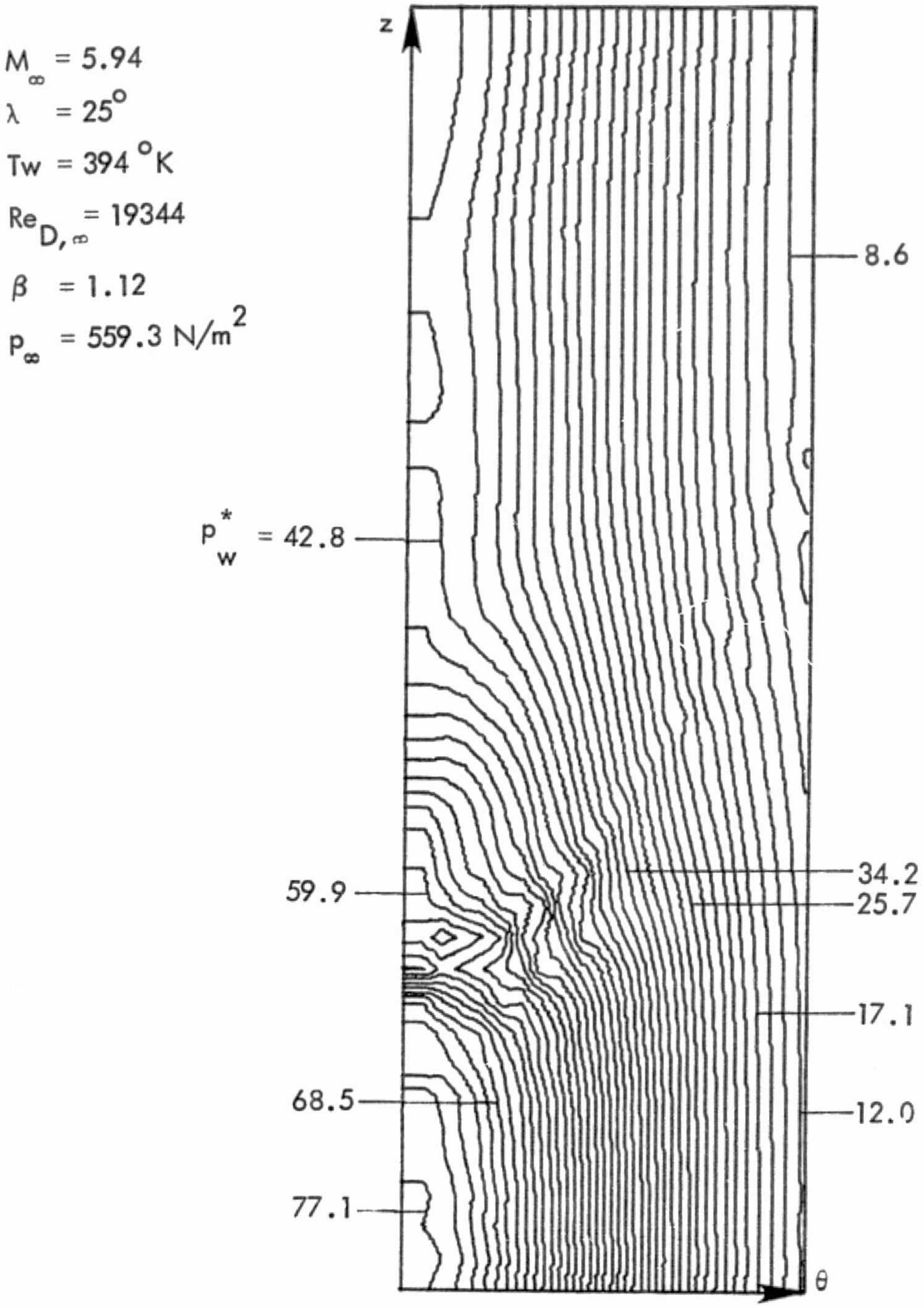

Figure 52. Wall pressure contours on a swept circular cylinder under the influence of an impinging shock.

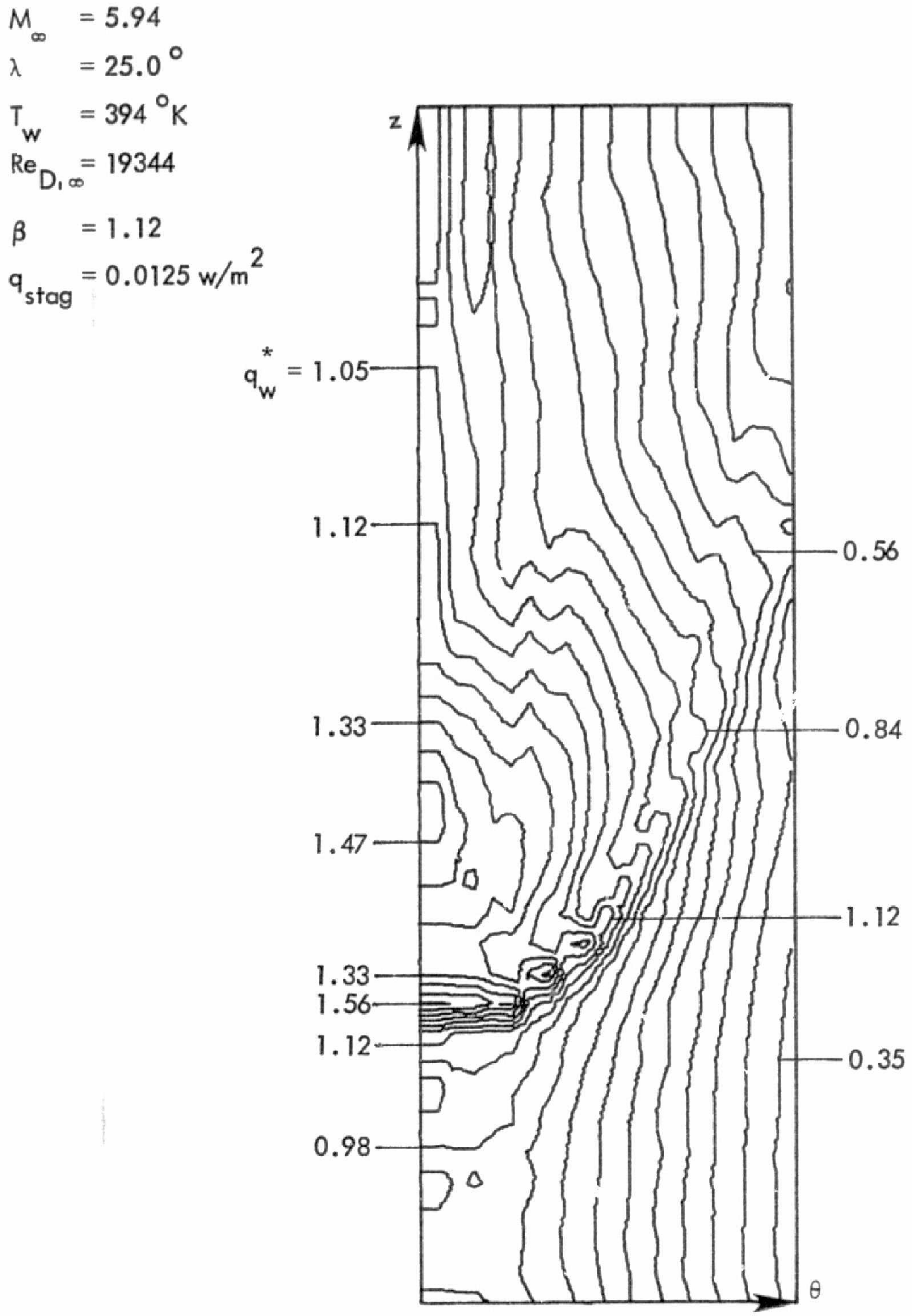

Figure 53. Wall heat transfer contours on a swept circular cylinder under the influence of an impinging shock.

very possibly the quality of the solution (especially for three-dimensional problems). Statistics such as these are examined in this section.

The computational statistics of the solutions presented in this report are given in Table 3. The number of time steps per case varies over a large range because of the different levels of desired convergence. For instance, the infinite cylinder solution (used as the initial condition for the three-dimensional shock impingement solution) was carried to a much higher level of convergence than the other infinite cylinder cases.

As previously mentioned, the large core memory (LCM) is used to store the three-dimensional solution array. Therefore, the required amount of LCM is proportional to the grid size. The small core memory (SCM) is used to store the program and the intermediate result arrays. The amount of storage listed in Table 3 does not include buffer storage or any storage allotted to the system.

The final statistic shows how much execution time is required on a per time step per grid point basis. The last two values in this category (three-dimensional solutions) are higher than the others because proportionally they contain a smaller number of boundary condition points. All execution times are for a Control Data Corporation 7600 Computer.

The small amount of storage required for the three-dimensional solution (only 131K words), is an achievement since the solution array by itself required 90K words. With the savings in storage produced by

Table 3. Computational statistics.

	Two-Dimensional Case	Infinite Cylinder Cases				Three-Dimensional Shock Impingement	
		Case A	Case B	Case C	Initial Condition Case	Coarse Mesh	Fine Mesh
Time steps	900	700	800	600	1500	750	400
No. of runs	6	6	3	3	14	14	13
Storage							
SCM (K words)	30	30	30	30	35	41	41
LCM (K words)	11	11	11	11	9	46	90
Mesh dimensions	21x21x5	21x21x5	21x21x5	21x21x5	21x21x4	21x21x21	21x21x41
Execution time (sec)	475	371	410	310	550	2832	2797
Execution time per time step per grid pt. (msec)	0.24	0.24	0.23	0.23	0.21	0.41	0.39

the sweeping procedure, larger more productive computational meshes can be used.

V. CONCLUDING REMARKS

A time-marching finite-difference method has been used to compute the three-dimensional wing-leading-edge shock impingement problem. The bow shock was treated as a sharp discontinuity across which the exact shock jump conditions (Rankine-Hugoniot relations) were applied. The impinging shock (assumed planar) was introduced by discontinuously changing the freestream conditions across the intersection line at the bow shock. The compressible Navier-Stokes equations were used for this three-dimensional computation. The present method does not require any prior information about the shock impingement flow field to be computed, as is the case with previous semiempirical approaches. In addition, since the shock layer flow field is automatically "captured" in the same manner in each computation, it is possible, in principle, to compute all three types of wing-leading-edge shock impingement with the same computer code.

A special storage-saving procedure for sweeping through the finite-difference mesh has been developed. This sweeping procedure reduces the required amount of computer storage by at least a factor of two without sacrificing the execution time. This savings in storage allows for larger more productive computational meshes which is especially useful for three-dimensional computations.

The shock impingement solution presented in this study demonstrates the feasibility of three-dimensional time-dependent computations involving the Navier-Stokes equations. At the time of this writing, only one other time-dependent solution of the three-dimensional Navier-Stokes equations is known to exist [74]. The computational demands associated with this problem, however, affect the quality of the present three-dimensional solution. The artificially reduced Reynolds number and the relatively coarse mesh are both limitations resulting from these computational demands. As a result of this study, however, it is felt that these limitations can be removed with the present method and with currently available advanced computers.

VI. RECOMMENDATIONS FOR FURTHER STUDY

Several recommendations concerning the extension of this work can be suggested. First, a new version of the shock smoothing technique (the old version is given by Equation 3.39) could greatly improve the results. Obviously this new technique should eliminate the oscillations in the bow shock, but, should not interfere with any physical "kinks" which might appear in the bow shock.

The alleviation of the bow shock oscillations could also be achieved in the shock slope calculation without the addition of any numerical smoothing. For instance, the use of a one-sided difference formula in place of the central difference formula to compute the shock slope might relieve the numerical instability causing the oscillations and therefore, remove the need for a bow shock smoother. One-sided formulas which could be used for this purpose are given by

$$\left(r_{s_z}\right)_{j,k} = \left(r_{s_{j,k+1}} - r_{s_{j,k}}\right)/\Delta z \qquad 6.1$$

$$\left(r_{s_z}\right)_{j,k} = \left(4r_{s_{j,k+1}} - r_{s_{j,k+2}} - 3r_{s_{j,k}}\right)/2\Delta z \qquad 6.2$$

where Equation 6.1 is a first-order forward-difference formula and Equation 6.2 is a second-order forward-difference formula. Both first- and second-order backward-difference formulas or alternating forward-backward formulas could also be tried.

Second, more grid points could improve the resolution of the shock layer detail. By increasing the number of grid points in the radial direction, better boundary layer resolution could be achieved making an accurate solution at higher Reynolds number possible. If the number of grid points in the cross-flow direction were increased, better resolution of the transmitted shock could be achieved. Because of the storage-saving procedure used in this study, the use of more grid points is possible and could be very beneficial. In addition, the resolution of the transmitted shock could be greatly improved by clustering the grid points in the cross-flow direction near the intersection line.

Third, a better comparison with experiment could be obtained if the inflow boundary condition in the cross-flow direction could be made to more adequately match the experiment. This could be achieved by using a different inflow boundary condition or by comparing with an experiment in which the impinging shock strikes the bow shock sufficiently far downstream from the blunted end (about six diameters).

Fourth, different shock interference patterns (Types IV and VI) could be computed by varying the sweep angle (λ). The Type IV interference pattern might be extremely difficult to compute because of the subsonic cross-flow Mach number.

Finally, other problems related to the present problem are given by the following: 1) Shock impingement with real gas effects, including both chemical equilibrium and chemical nonequilibrium. 2) Shock impingement where the body is a hemisphere. 3) A wing leading edge solution in which the body is more accurately modeled as a wing (i.e., variable body radius, taper, angle of attack, etc.).

VII. REFERENCES

1. Edney, B. E. "Anomalous Heat Transfer and Pressure Distributions on Blunt Bodies at Hypersonic Speeds in the Presence of an Impinging Shock." FFA Rept. 115, The Aeronautical Research Institute of Sweden, Stockholm, Sweden, February 1968.

2. Keyes, J. W. and Hains, F. D. "Analytical and Experimental Studies of Shock Interference Heating in Hypersonic Flows." National Aeronautics and Space Administration, TN D-7139, 1973.

3. Korkegi, R. H. "Survey of Viscous Interactions Associated with High Mach Number Flight." AIAA Journal, 9, No. 5 (May 1971), 771-784.

4. Newlander, R. A. "Effect of Shock Impingement on the Distribution of Heat-Transfer Coefficients on a Right Circular Cylinder at Mach Numbers of 2.65, 3.51, and 4.44." National Aeronautics and Space Administration, TN D-642, 1961.

5. Carter, H. S. and Carr, R. E. "Free-Flight Investigation of Heat Transfer to an Unswept Cylinder Subjected to an Incident Shock and Flow Interference From an Upstream Body at Mach Numbers up to 5.50." National Aeronautics and Space Administration, TN D-988, 1961.

6. Beckwith, I. E. "Experimental Investigation of Heat Transfer and Pressures on a Swept Cylinder in the Vicinity of Its Intersection With a Wedge and Flat Plate at Mach Number 4.15 and High Reynolds Numbers." National Aeronautics and Space Administration, TN D-2020, 1964.

7. Jones, R. A. "Heat-Transfer and Pressure Investigation of a Fin-Plate Interference Model at a Mach Number of 6." National Aeronautics and Space Administration, TN D-2028, 1964.

8. Siler, L. G., and Deskins, H. E. "Effect of Shock Impingement on Heat-Transfer and Pressure Distributions on a Cylindrical-Leading-Edge Model at Mach Number 19." AEDC-TDR-64-228, U.S. Air Force, November 1964.

9. Bushnell, D. M. "Interference Heating on a Swept Cylinder in Region of Intersection With a Wedge at Mach Number 8." National Aeronautics and Space Administration, TN D-3094, 1964.

10. Francis, W. L. "Experimental Heat-Transfer Study of Shock Impingement on Fins in Hypersonic Flow." Journal of Spacecraft and Rockets, 2, No. 4 (July - August 1965), 630-632.

11. Gulbran, C. E., Redeker, E., Miller, D. S., and Strack, S. L. "Heating in Regions of Interfering Flow Fields - Part I: Two- and Three-Dimensional Interactions at Mach 8." AFFDL-TR-65-49, Pt. I, U.S. Air Force, July 1965.

12. Knox, E. C. "Measurements of Shock-Impingement Effects on the Heat-Transfer and Pressure Distributions on a Hemicylinder Model at Mach Number 19." AEDC-TR-65-245, U.S. Air Force, November 1965.

13. Popinski, Z. "Shock Wave-Boundary Layer Interaction." Proceedings of the Third International Heat Transfer Conference - Vol. II. Amer. Inst. Chem. Eng., August 1966, pp. 262-273.

14. Ray, A. D. and Palko, R. L. "An Investigation of the Effects of Shock Impingement on a Blunt Leading Edge." AEDC-TR-65-153, U.S. Air Force, July 1965.

15. Gulbran, C. E., Redeker, E., Miller, D. S., and Strack, S. L. "Heating in Regions of Interfering Flow Fields - Part II: Leading Edge Shock Impingement." AFFL-TR-65-49, Pt. II, U.S. Air Force, January 1967.

16. Hiers, R. S. and Loubsky, W. J. "Effects of Shock-Wave Impingement on the Heat Transfer on a Cylindrical Leading Edge." National Aeronautics and Space Administration, TN D-3859, 1967.

17. Uselton, J. C. "Fin Shock/Boundary-Layer Interaction Tests on a Flat Plate With Blunted Fins at M = 3 and 5." AEDC-TR-67-113, U.S. Air Force, June 1967.

18. Bushnell, D. M. "Effects of Shock Impingement and Other Factors on Leading-Edge Heat Transfer." National Aeronautics and Space Administration, TN D-4543, 1968.

19. Watts, J. D. "Flight Experience With Shock Impingement and Interference Heating on the X-15-2 Research Airplane." National Aeronautics and Space Administration, TM X-1669, 1968.

20. Young, F. L., Kaufman, L. G., II, and Korkegi, R. H. "Experimental Investigation of Interactions Between Blunt Fin Shock Waves and Adjacent Boundary Layers at Mach Numbers 3 and 5." ARL 68-0214, U.S. Air Force, December 1968.

21. Jones, R. A., and Hunt, J. L. "Measurements of Mutual Interference Heating for a Probe Antenna Mounted on an Apollo Reentry Configuration." National Aeronautics and Space Administration, TM X-1787, 1969.

22. Mashburn, J. H. "Turbulent Boundary Layer Separation Ahead of Cylindrical Protuberances in Supersonic Flow." ARL-TR-69-17, The University of Texas at Austin, August 1969.

23. Spurlin, C. J. "Heat-Transfer Tests of a Multipurpose Entry Vehicle at Mach Number 10." AEDC-TR-69-206, U.S. Air Force, November 1969.

24. Martindale, W. R. "Interference Heating Measurements on a Hypersonic Cruise Vehicle Wing Using the Phase-Change Paint Technique." AEDC-TR-70-78, U.S. Air Force, April 1970.

25. Teterin, M. P. "Investigation of a Supersonic Gas Flow and Heat Transfer in the Region of an Incident Shock Wave on a Cylinder." National Aeronautics and Space Administration, TT F-11, 795, 1968.

26. Holden, M. S. "Shock Wave-Turbulent Boundary Layer Interaction in Hypersonic Flow." AIAA Paper No. 72-74, January 1972.

27. Kaufman, L. G., II, Korkegi, R. H., and Morton, L. C. "Shock Impingement Caused by Boundary Layer Separation Ahead of Blunt Fins." RM-536, Grumman Aerospace Corporation, February 1972.

28. Haslett, R. A., Kaufman, L. G., II, Romanowski, R. F., and Urkowitz, M. "Interference Heating Due to Shock Impingement." AFFDL-TR-72-66, U.S. Air Force, July 1972.

29. Edney, B. E., Bramlette, T. T., Ives, J., Hains, F. D., and Keyes, J. W. "Theoretical and Experimental Studies of Shock Interference Heating." Bell Aerospace Co. Rep. No. 9500-920-195, October 1970.

30. Hains, F. D., and Keyes, J. W. "Shock Interference Heating in Hypersonic Flows." AIAA Journal, 10, No. 11 (November 1972), 1441-1447.

31. Keyes, J. W. "Off-Center-Line Shock-Interference Heating Patterns on Basic Shapes in Hypersonic Flows." National Aeronautics and Space Administration, TM X-2866, 1973.

32. Doughty, R. O., Erickson, R. C., Brock, O. R., Moore, T. W., and Clifton, J. V. "Convective Heating on Delta-Wing Space-Shuttle Boosters Including Interference Effects." Journal of Spacecraft and Rockets, 9, No. 12 (December 1972), 876-882.

33. Bertin, J. J. and Hinkle, J. C. "An Experimental Investigation of the Flow-Field for Double-Wedge Configurations in a Mach 4.97 Stream." Aerospace Engineering Report 74003, The University of Texas at Austin, June 1974.

34. Palko, R. L. Arnold Air Force Station. Unpublished data from AEDC. Personal Consultation, 1974.

35. Craig, R. R. and Ortwerth, P. J. "Experimental Study of Shock Impingement on a Blunt Leading Edge with Application to Hypersonic Inlet Design." AFAPL-TR-71-10, U.S. Air Force, April 1971.

36. Crawford, D. H. "A Graphical Method for the Investigation of Shock Interference Phenomena." AIAA Journal, 11, No. 11 (November 1973), 1590-1592.

37. Bramlette, T. T. "Simple Technique for Predicting Type III and IV Shock Interference." AIAA Journal, 12, No. 8 (August 1974), 1151-1152.

38. Markarian, C. F. "Heat Transfer in Shock Wave Boundary Layer Interaction Regions." Naval Weapons Center, China Lake, California, NWC TP4485, November 1968.

39. Back, L. H. and Cuffel, R. F. "Changes in Heat Transfer from Turbulent Boundary Layers Interacting with Shock Waves and Expansion Waves." AIAA Journal, 8, No. 10 (October 1970), 1871-1873.

40. Murphy, J. D. "A Critical Evaluation of Analytical Methods for Predicting Laminar-Boundary Layer Shock-Wave Interaction." National Aeronautics and Space Administration, SP228, 1969.

41. Nestler, D. E. "Correlation of Turbulent Heat Flux to Deceleration Flaps in Supersonic Flow." Journal of Spacecraft and Rockets, 5, No. 8 (August 1968), 998-1000.

42. Bushnell, D. M. and Weinstein, L. M. "Correlation of Peak Heating for Reattachment of Separated Flows." Journal of Spacecraft and Rockets, 5, No. 9 (September 1968), 1111-1112.

43. Keyes, J. W. and Morris, D. J. "Correlations of Peak Heating in Shock Interference Regions at Hypersonic Speeds." Journal of Spacecraft and Rockets, 9, No. 8 (August 1972), 621-623.

44. Morris, D. J. and Keyes, J. W. "Computer Programs for Predicting Supersonic and Hypersonic Interference Flow Fields and Heating." National Aeronautics and Space Administration, TM X-2725, 1973.

45. Bertin, J. J., Graumann, B. W., and Goodrich, W. D. "Analysis of High-Velocity and Real-Gas Effects on the Shock-Interference Pattern for Delta-Wing Orbiters." AIAA Paper No. 74-522, June 1974.

46. Hayes, W. D. and Probstein, R. F. Hypersonic Flow Theory. Volume I. Inviscid Flows. 2nd ed. Applied Mathematics and Mechanics. Volume 5A. New York: Academic Press, 1966.

47. Daywitt, J. E. and Anderson, D. A. "Analysis of a Time-Dependent Finite-Difference Technique for Shock Interaction and Blunt-Body Flows." Iowa State University, Ames, Iowa, ERI Report 74074, 1974.

48. Bohachevsky, I. O. and Rubin, E. L. "A Direct Method for Computation of Nonequilibrium Flows with Detached Shock Waves." AIAA Journal, 4, No. 4 (April 1966), 600-607.

49. Burstein, S. Z. "Finite-Difference Calculations for Hydrodynamic Flows Containing Discontinuities." Journal of Computational Physics, 2, (1967), 198-222.

50. Lapidus, A. "A Detached Shock Calculation by Second-Order Finite Differences." Journal of Computational Physics, 2, (1967), 154-177.

51. Moretti, G. and Abbett, M., "A Time-Dependent Computational Method for Blunt Body Flows." AIAA Journal, 4, No. 12 (December 1966), 2136-2141.

52. Li, C. P. "Numerical Solution of Viscous Reacting Blunt Body Flows of a Multicomponent Mixture." AIAA Paper No. 73-202, January 1973.

53. Tannehill, J. C. and Holst, T. L. "Numerical Computation of Two-Dimensional Viscous Blunt Body Flows with an Impinging Shock." Iowa State University, Ames, Iowa, ERI Report 74057, 1974.

54. Tannehill, J. C., Holst, T. L., and Rakich, J. V. "Numerical Computation of Two-Dimensional Viscous Blunt Body Flows with an Impinging Shock." AIAA Paper No. 75-154, January 1975.

55. Holst, T. L., Tannehill, J. C., and Rakich, J. V. "Numerical Computation of Viscous Blunt Body Flows with a Planar Impinging Shock." Presented at the NASA Conference on Aerodynamic Analysis Requiring Advanced Computers, March 4-6, 1975, Langley Research Center, Hampton, Virginia.

56. Yuan, S. W. Foundations of Fluid Mechanics. Englewood Cliffs, New Jersey: Prentice-Hall, Inc., 1967.

57. Tsien, H. S. "The Equations of Gas Dynamics." Fundamentals of Gas Dynamics, H. W. Emmons, ed., Princeton, New Jersey: Princeton University Press, 1958.

58. Owczarek, J. A. Fundamentals of Gas Dynamics. Scranton, Pennsylvania: International Textbook Company, 1964.

59. Roberts, G. O. "Computational Meshes for Boundary Layer Problems." In Lecture Notes in Physics, Vol. 8, New York: Springer-Verlag, 1971, pp. 171-177.

60. MacCormack, R. W. "The Effect of Viscosity in Hypervelocity Impact Cratering." AIAA Paper 69-354, 1969.

61. Tannehill, J. C., Mohling, R. A., and Rakich, J. V. "Numerical Computation of the Hypersonic Rarefied Flow Near the Sharp Leading Edge of a Flat Plate." AIAA Paper 73-200, 1973.

62. Thomas, P. D., Vinokur, M., Bastianon, R. A., and Conti, R. J. "Numerical Solution for Three-Dimensional Inviscid Supersonic Flow." AIAA Journal, 10, No. 7 (July 1972), 887-894.

63. Kutler, P., Reinhardt, W. A., and Warming, R. F. "Numerical Computation of Multishocked, Three-Dimensional Supersonic Flow Fields With Real Gas Effects." AIAA Paper 72-702, 1972.

64. Ames Research Staff. "Equations, Tables and Charts for Compressible Flow." National Advisory Committee for Aeronautics, NACA Report 1135, 1953.

65. Billig, F. S. "Shock-Wave Shapes Around Spherical - and Cylindrical - Nosed Bodies." Journal of Spacecraft and Rockets, 4, No. 6 (June 1967), 822-823.

66. MacCormack, R. W. "Numerical Solution of the Interaction of a Shock Wave With a Laminar Boundary Layer." In Lecture Notes in Physics, Vol. 8, New York: Springer Verlag, 1971, pp. 151-163.

67. Horstman, C. C., Kussoy, M. I., Coakley, T. J., Rubesin, M. W., and Marvin, J. G. "Shock-Wave-Induced Turbulent Boundary-Layer Separation at Hypersonic Speeds." AIAA Paper 75-4, 1975.

68. Kutler, P. and Sakell, L. "Three-Dimensional, Shock-on-Shock Interaction Problem." AIAA Paper No. 75-49, January 1975.

69. Deiwert, G. S. "Numerical Simulation of High Reynolds Number Transonic Flows." AIAA Paper 74-603, 1974.

70. Baldwin, B. S. and MacCormack, R. W. "Numerical Solution of the Interaction of a Strong Shock Wave with a Hypersonic Turbulent Boundary Layer." AIAA Paper 74-558, 1974.

71. MacCormack, R. W. "Numerical Methods for Hyperbolic Systems." Short Course on Advances in Computational Fluid Dynamics, The University of Tennessee Space Institute, Tullahoma, Tennessee, December 10-14, 1973.

72. Beckwith, I. E. and Cohen, N. B. "Application of Similar Solutions to Calculation of Laminar Heat Transfer on Bodies with Yaw and Large Pressure Gradient in High-Speed Flow." National Aeronautics and Space Administration, TN D-625, 1961.

73. Beckwith, I. E. and Gallagher, J. J. "Local Heat Transfer and Recovery Temperatures on a Yawed Cylinder at a Mach Number of 4.15 and High Reynolds Numbers." National Aeronautics and Space Administration, Technical Report R-104, 1961.

74. Goodrich, W. D., Li, C. P., Houston, C. K., Myers, R. M., Olmedo, L. "Scaling of Orbiter Aerothermodynamic Data Through Numerical Flow Field Simulations." Presented at the NASA Conference on Aerodynamic Analysis Requiring Advanced Computers, March 4-6, 1975, Langley Research Center, Hampton, Virginia.

75. Tannehill, J. C. and Mohling, R. A. "Development of Equilibrium Air Computer Programs Suitable for Numerical Computation Using Time-Dependent or Shock-Capturing Methods." National Aeronautics and Space Administration, CR-2134, 1972.

76. Tannehill, J. C. and Mugge, P. H. "Improved Curve Fits for the Thermodynamic Properties of Equilibrium Air Suitable for Numerical Computation Using Time-Dependent or Shock-Capturing Methods." National Aeronautics and Space Administration, CR-2470, 1974.

VIII. ACKNOWLEDGMENTS

The support of this work by NASA Ames Research Center under grant NGR 16-002-038 and by the Iowa State University Engineering Research Institute is gratefully acknowledged.

IX. APPENDIX A: REAL GAS SOLUTION PROCEDURE

Presented in this appendix is the solution procedure (including the shock jump conditions) when real gas effects are included. The fluid is assumed to be air in chemical equilibrium. The solution procedure is identical to the procedure used for a perfect gas case with the following two exceptions: First, all thermodynamic properties of the fluid are determined from curve fits designed especially for use with finite-difference methods [74,75]. The curve fits available are indicated by

$$\begin{aligned} p &= p(e,\rho) \\ a &= a(e,\rho) \\ T &= T(e,\rho) \qquad\qquad \text{A.1} \\ h &= h(p,\rho) \\ T &= T(p,\rho) \end{aligned}$$

where p is the pressure, e is the internal energy, ρ is the density, a is the speed of sound, T is the temperature, and h is the static enthalpy. These curve fits are valid for temperatures up to 25,000 ^{o}K and densities from 10^{-7} to 10^{3} amagats.

Second, the expressions for ρ_2 and V_N in the shock jump conditions (Equations 3.14 and 3.15) are not valid when the fluid is assumed to be in chemical equilibrium across the bow shock. Closed-form analytical expressions for ρ_2 and V_N for the real gas case cannot be found because a closed-form analytical expression for the equation of state does not exist. Therefore, for the real gas case, an iterative procedure is required.

The freestream density (ρ_∞), the freestream pressure (p_∞), and the freestream static enthalpy (h_∞) are all known and held constant, just as in the perfect gas case. The pressure just downstream of the bow shock (p_2) is computed by exactly the same technique used in the perfect gas case. The iteration procedure, which is used to determine ρ_2 and V_N, begins at this point. The density ratio ($DR = \rho_\infty / \rho_2$) is the basic iteration parameter. Both lower and upper bounds for the density ratio (DR_{min} and DR_{max}) must be computed at the start of the iteration and are given by

$$DR_{min} = 0.0 \qquad \text{A.2}$$

$$DR_{max} = \frac{\frac{p_2}{p_\infty}\frac{\gamma-1}{\gamma+1} + 1}{\frac{\gamma-1}{\gamma+1} + \frac{p_2}{p_\infty}} \qquad \text{A.3}$$

Notice that the upper bound density ratio (Equation A.3) is obtained from the perfect gas formula.

Next, the exact value of the density ratio (DR) is approximated by

$$DR = (DR_{min} + DR_{max})/2 \qquad \text{A.4}$$

Using this density ratio, a value for V_N is computed from

$$V_N = \sqrt{\frac{p_2 - p_\infty}{\rho_\infty(1 + DR)}} \qquad \text{A.5}$$

which is an exact shock jump relation. Next, a value for h_2 is computed from the curve fit formula

$$h_2 = h(p_2, \rho_2) \qquad \text{A.6}$$

With these values of V_N and h_2, the density ratio is recomputed from

$$DR_{com} = 2\sqrt{\frac{h_1 - h_2}{V_N^2} + 1} \qquad \text{A.7}$$

which is another independent relation obtained from the shock jump conditions. At this point a convergence test, which involves a comparison between $|DR - DR_{com}|$ and a predetermined error tolerance, is made. If the test is passed, the iteration is stopped, and the current values of ρ_2 and V_N are used to compute the velocity components ($u_{r,2}$, $u_{\theta,2}$, and $u_{z,2}$) and the radial shock velocity (r_{s_t}) from Equations 3.16 - 3.19. If the test fails, either DR_{min} or DR_{max} is updated according to the following scheme:

$$\text{If } DR_{com} > DR \quad \text{then } DR_{min} = DR \qquad \text{A.8}$$

$$\text{If } DR_{com} < DR \quad \text{then } DR_{max} = DR \qquad \text{A.9}$$

With the newly computed value for either DR_{min} or DR_{max} the process given by Equations A.4 - A.9 is repeated until the convergence test is satisfied.

During the iteration process a special problem associated with Equation A.7 may occur. If the density ratio given by Equation A.4 is far enough from the desired result the radical in Equation A.7 will be negative. This situation is alleviated by returning to Equation A.4 with DR_{max} set equal to the current value of DR.

The process just presented is known as a bisection type of iteration. Convergence is guaranteed providing that the final value for DR lies between the initial values of DR_{min} and DR_{max}. Because this routine only halves the solution interval for each iteration, many iterations are required to obtain reasonable accuracy. To reduce the number of iterations a linear interpolating procedure for obtaining improved density ratio approximations has been added. A schematic of this procedure is shown in Figure A1 where the density ratio values lie along the horizontal axis and the errors ($ER = |DR - DR_{com}|$) lie along the vertical axis. Notice that both the minimum and maximum density ratios and the corresponding errors for these density ratios are indicated in Figure A1. Improved approximations for DR are obtained by replacing Equation A.4 with

$$DR = DR_{min} + ER_{min} \frac{DR_{max} - DR_{min}}{ER_{min} + ER_{max}} \qquad A.10$$

where ER_{min} and ER_{max} are determined from

$$ER_{min} = \left| DR_{min} - DR_{com} \right| \qquad A.11$$

$$ER_{max} = \left| DR_{max} - DR_{com} \right| \qquad A.12$$

The use of this linear interpolating scheme may speed up the iteration process by as much as three times.

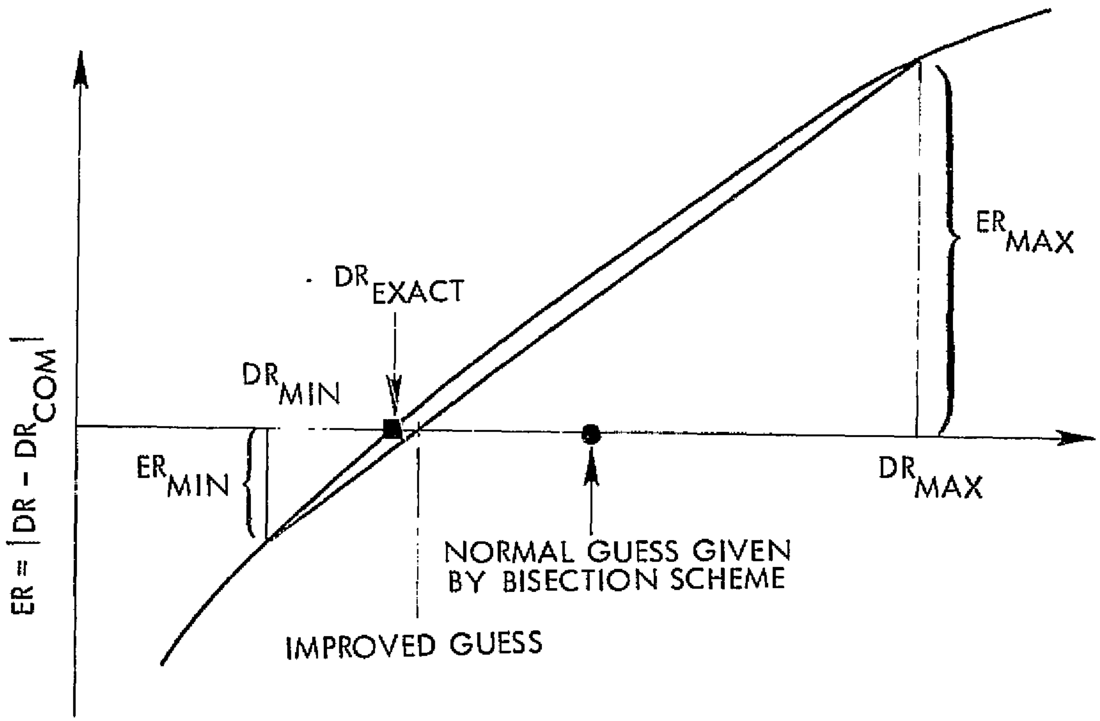

Figure A1. Linear interpolating procedure used in the shock jump iteration scheme.

The zero normal pressure gradient boundary condition which was used to compute wall values of density if given by

$$\rho_{NI} = \rho_{NI-1} e_{NI-1} / e_{NI} \qquad \text{A.13}$$

where the subscripts NI and NI - 1 represent the values at the wall and one grid row above the wall, respectively. This boundary condition was used in the real gas computation, even though its formulation requires a perfect gas assumption. For physically realistic cold wall solutions in the real gas range, however, the temperature in the vicinity of the wall (i.e., in the lower part of the boundary layer) is probably low enough to make this boundary condition valid.

Sutherland's viscosity law, in conjunction with a constant Prandtl number assumption, were used to compute the coefficients of viscosity (μ) and thermal conductivity (k). These assumptions are generally not valid for real gas calculations. However, other alternatives, such as curve fit approximations (for μ and k), are not available at the present time.

The above real gas procedure was used in conjunction with the previously presented finite-difference procedure to compute a sample infinite cylinder solution. Because of the inaccurate method for computing the real gas transport properties, the solution computed with the real gas procedure was chosen to be in the perfect gas range. Comparisons made between the real gas solution and the corresponding perfect gas solution were very good. The real gas computation required 50 percent more execution time on a per time step per grid point basis than the perfect gas computation. By this means the real gas procedure was tested. Before any effective real gas computations can be made with this procedure, a fast approximate method for evaluating the transport properties of air in the real gas regime must be found.

X. APPENDIX B: SHOCK JUMP CONDITIONS

The derivations of the three-dimensional shock jump conditions as well as the three-dimensional radial shock velocity equation are presented in this appendix. The resulting equations are in a form convenient for computer application. Figure B1 shows a sketch of the local shock-fixed coordinate system ($\hat{i}_N, \hat{i}_T, \hat{i}_B$) along with the standard cylindrical coordinate system ($\hat{i}_r, \hat{i}_\theta, \hat{i}_z$).

A. Three-Dimensional Shock Jump Conditions

The resultant velocity vector on the downstream side of the bow shock ($\vec{V}_2$) may be expressed as the vector sum of the freestream velocity vector ($\vec{V}_\infty$) and some arbitrary velocity vector increment ($\Delta\vec{V}$) as given in Equation B.1.

$$\vec{V}_{2,s} = \vec{V}_{\infty,s} + \Delta\vec{V}_s \qquad \text{B.1}$$

Equation B.1 is written in the shock-fixed coordinate system (see Figure B1). $\vec{V}_{\infty,s}$ and $\vec{V}_{2,s}$ are given by

$$\vec{V}_{\infty,s} = u_{N,\infty}\hat{i}_N + u_{T,\infty}\hat{i}_T + u_{B,\infty}\hat{i}_B \qquad \text{B.2}$$

$$\vec{V}_{2,s} = u_{N,2}\hat{i}_N + u_{T,2}\hat{i}_T + u_{B,2}\hat{i}_B \qquad \text{B.3}$$

where $u_{N,\infty}$, $u_{T,\infty}$, and $u_{B,\infty}$ are the components of $\vec{V}_{\infty,s}$ in the shock normal, tangent, and binormal directions, respectively, and $u_{N,2}$, $u_{T,2}$,

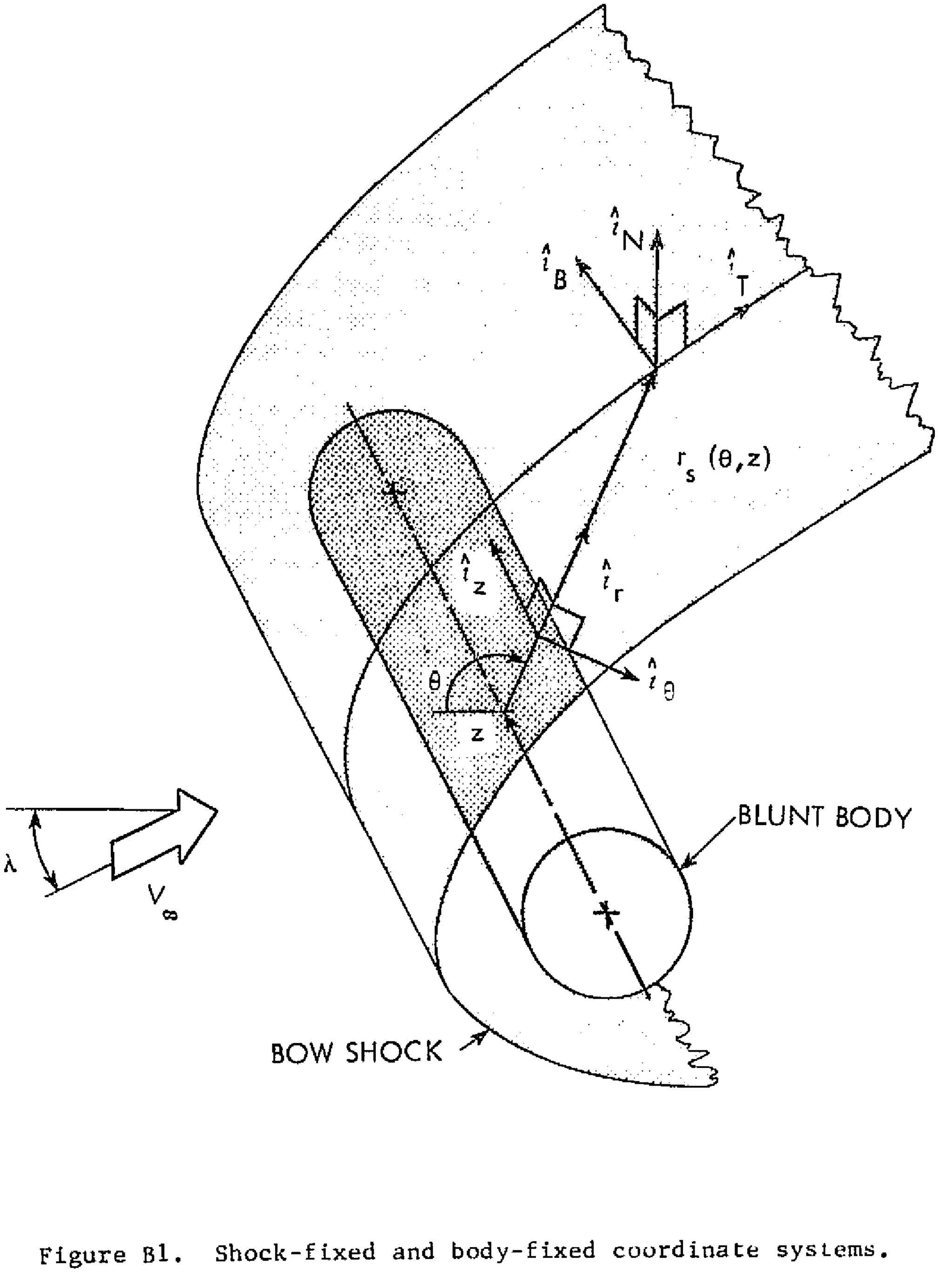

Figure B1. Shock-fixed and body-fixed coordinate systems.

and $u_{B,2}$ are the components of $V_{2,s}$ in the shock normal, tangent and binormal directions, respectively.

Upon substitution of Equations B.2 and B.3 into Equation B.1 and applying the fact that tangential components of velocity pass through shock waves unaltered yields

$$\Delta\vec{V}_s = (u_{N,2} - u_{N,\infty})\hat{i}_N \qquad \text{B.4}$$

Note that the arbitrary velocity vector increment ($\Delta\vec{V}_s$) is normal to the bow shock as expected.

The relative velocity equations for the $\vec{V}_2$ and $\vec{V}_\infty$ velocity vectors between the shock-fixed and the body-fixed coordinate systems can be written as

$$\vec{V}_{2,s} = \vec{V}_{2,b} - \vec{V}_{s/b} \qquad \text{B.5}$$

$$\vec{V}_{\infty,s} = \vec{V}_{\infty,b} - \vec{V}_{s/b} \qquad \text{B.6}$$

where $\vec{V}_{s/b}$ is the relative velocity of the bow shock with respect to the body and $\vec{V}_{2,b}$ and $\vec{V}_{\infty,b}$ are given by

$$\vec{V}_{2,b} = u_{r,2}\hat{i}_r + u_{\theta,2}\hat{i}_\theta + u_{z,2}\hat{i}_z \qquad \text{B.7}$$

$$\vec{V}_{\infty,b} = u_{r,\infty}\hat{i}_r + u_{\theta,\infty}\hat{i}_\theta + u_{z,\infty}\hat{i}_z \qquad \text{B.8}$$

where $u_{r,2}$, $u_{\theta,2}$, and $u_{z,2}$ are the components of $\vec{V}_{2,b}$ in the body coordinate system and $u_{r,\infty}$, $u_{\theta,\infty}$, and $u_{z,\infty}$ are the components of $\vec{V}_{\infty,b}$ in the body coordinate system. Substitution of Equations B.4, B.5

and B.6 into Equation B.1 yields

$$\vec{V}_{2,b} = \vec{V}_{\infty,b} + (u_{N,2} - u_{N,\infty})\hat{i}_N \qquad \text{B.9}$$

By taking components of Equation B.9 in the r-, θ-, and z-directions yields

$$u_{r,2} = \vec{V}_{2,b}\cdot\hat{i}_r = u_{r,\infty} + (u_{N,2} - u_{N,\infty})(\hat{i}_N\cdot\hat{i}_r) \qquad \text{B.10}$$

$$u_{\theta,2} = \vec{V}_{2,b}\cdot\hat{i}_\theta = u_{\theta,\infty} + (u_{N,2} - u_{N,\infty})(\hat{i}_N\cdot\hat{i}_\theta) \qquad \text{B.11}$$

$$u_{z,2} = \vec{V}_{2,b}\cdot\hat{i}_z = u_{z,\infty} + (u_{N,2} - u_{N,\infty})(\hat{i}_N\cdot\hat{i}_z) \qquad \text{B.12}$$

The three components $u_{r,2}$, $u_{\theta,2}$, and $u_{z,2}$ are the desired velocity components just downstream of the bow shock in the body coordinate system. More useable expressions for the second terms on the right hand sides of these three equations must now be found.

The general expression for the bow shock surface is given by

$$r_s = f(\theta,z) \qquad \text{B.13}$$

or written in a different way

$$F(r,\theta,z) = r_s - f(\theta,z) = 0 \qquad \text{B.14}$$

An outward unit normal vector to the shock surface can be found by using

$$\hat{i}_N = \frac{\nabla F}{|\nabla F|} \qquad \text{B.15}$$

where the $\nabla(\,)$ operator in cylindrical coordinates is defined by

$$\nabla(\,) = \frac{\partial()}{\partial r}\,\hat{i}_r + \frac{1}{r}\frac{\partial()}{\partial \theta}\,\hat{i}_\theta + \frac{\partial()}{\partial z}\,\hat{i}_z \tag{B.16}$$

which yields

$$\hat{i}_N = \frac{\hat{i}_r - (r_{s_\theta}/r_s)\hat{i}_\theta - r_{s_z}\hat{i}_z}{\sqrt{1 + (r_{s_\theta}/r_s)^2 + (r_{s_z})^2}} \tag{B.17}$$

Taking components of Equation B.17 in the r-, θ-, and z-directions yields

$$\hat{i}_N\cdot\hat{i}_r = \frac{1}{\sqrt{1 + (r_{s_\theta}/r_s)^2 + (r_{s_z})^2}} \tag{B.18}$$

$$\hat{i}_N\cdot\hat{i}_\theta = \frac{-r_{s_\theta}/r_s}{\sqrt{1 + (r_{s_\theta}/r_s)^2 + (r_{s_z})^2}} \tag{B.19}$$

$$\hat{i}_N\cdot\hat{i}_z = \frac{-r_{s_z}}{\sqrt{1 + (r_{s_\theta}/r_s)^2 + (r_{s_z})^2}} \tag{B.20}$$

Next, an expression for $(u_{N,2} - u_{N,\infty})$ in terms of freestream quantities and the pressure just downstream of the bow shock (p_2) is desired. To this end the Rankine-Hugoniot equations are used and are given by [58]

$$p_\infty + \rho_\infty u_{N,\infty}^2 = p_2 + \rho_2 u_{N,2}^2 \tag{B.21}$$

$$\rho_\infty u_{N,\infty} = \rho_2 u_{N,2} \tag{B.22}$$

Combination of these two equations yields

$$u_{N,2} - u_{N,\infty} = \frac{p_\infty - p_2}{\rho_\infty u_{N,\infty}} \tag{B.23}$$

Substitution of Equations B.18, B.19, B.20, and B.23 into Equations B.10, B.11, and B.12 yields the shock jump conditions for the velocity components in body-fixed coordinates, which are given by

$$u_{r,2} = u_{r,\infty} + \frac{p_\infty - p_2}{\rho_\infty u_{N,\infty}} \frac{1}{\sqrt{1 + (r_{s_\theta}/r_s)^2 + (r_{s_z})^2}} \tag{B.24}$$

$$u_{\theta,2} = u_{\theta,\infty} + \frac{p_\infty - p_2}{\rho_\infty u_{N,\infty}} \frac{-r_{s_\theta}/r_s}{\sqrt{1 + (r_{s_\theta}/r_s)^2 + (r_{s_z})^2}} \tag{B.25}$$

$$u_{z,2} = u_{z,\infty} + \frac{p_\infty - p_2}{\rho_\infty u_{N,\infty}} \frac{-r_{s_z}}{\sqrt{1 + (r_{s_\theta}/r_s)^2 + (r_{s_z})^2}} \tag{B.26}$$

To complete this set of shock jump conditions expressions for $u_{N,\infty}$ and ρ_2 in terms of freestream quantities and p_2 are needed. The expression for $u_{N,\infty}$ is usually written in terms of another quantity defined by

$$V_N = \bar{V}_{\infty,s} \cdot (-\hat{i}_N) = -u_{N,\infty} \tag{B.27}$$

For the case of a real gas where the flow is everywhere in chemical equilibrium, including across the bow shock, closed-form expressions for V_N and ρ_2 do not exist. Appendix A deals with this case by utilizing curve fits for the properties of air and an iteration procedure to compute V_N and ρ_2.

For the case of a perfect gas, closed-form expressions for V_N and ρ_2 are available [54,64]. By using these expressions and the new definition for V_N, the entire set of three-dimensional shock jump conditions can be stated as

$$\rho_2 = \rho_\infty \frac{\dfrac{\gamma-1}{\gamma+1} + \dfrac{p_2}{p_\infty}}{\dfrac{p_2}{p_\infty}\dfrac{\gamma-1}{\gamma+1} + 1} \tag{B.28}$$

$$V_N = \sqrt{\frac{\gamma+1}{2}\frac{p_\infty}{\rho_\infty}\left(\frac{\gamma-1}{\gamma+1} + \frac{p_2}{p_\infty}\right)} \tag{B.29}$$

$$u_{r,2} = u_{r,\infty} - \frac{p_\infty - p_2}{\rho_\infty V_N}\frac{1}{\sqrt{1 + (r_{s_\theta}/r_s)^2 + (r_{s_z})^2}} \tag{B.30}$$

$$u_{\theta,2} = u_{\theta,\infty} + \frac{p_\infty - p_2}{\rho_\infty V_N}\frac{r_{s_\theta}/r_s}{\sqrt{1 + (r_{s_\theta}/r_s)^2 + (r_{s_z})^2}} \tag{B.31}$$

$$u_{z,2} = u_{z,\infty} + \frac{p_\infty - p_2}{\rho_\infty V_N}\frac{r_{s_z}}{\sqrt{1 + (r_{s_\theta}/r_s)^2 + (r_{s_z})^2}} \tag{B.32}$$

B. Three-Dimensional Radial Shock Velocity Equation

Figure B2 shows a sketch of a segment of the bow shock at time t and t + Δt and some of the key notation used in this derivation. The relative velocity equation for the freestream velocity vector ($\vec{V}_\infty$) between the shock-fixed and the body-fixed coordinate systems is given by Equation B.6. The freestream velocity component normal to the bow shock, measured in shock-fixed coordinates, and positive inward (V_N) can be written with the aid of Equation B.6 as

$$V_N = \vec{V}_{\infty,s} \cdot (-\hat{i}_N) = (\vec{V}_{\infty,b} - \vec{V}_{s/b}) \cdot (-\hat{i}_N) \qquad \text{B.33}$$

Equation B.33 may be simplified by using Equation B.8, B.18, B.19, and B.20 to yield

$$V_N = \frac{-u_{r,\infty} + u_{\theta,\infty}(r_{s_\theta}/r_s) + u_{z,\infty} r_{s_z}}{\sqrt{1 + (r_{s_\theta}/r_s)^2 + (r_{s_z})^2}} + \vec{V}_{s/b} \cdot \hat{i}_N \qquad \text{B.34}$$

At this point reference to Figure B2 is necessary to obtain a more useful relationship for the last term of Equation B.34. Note that $\vec{V}_{s/b}$ is the component of $r_{s_t} \hat{i}_r$ in the shock normal direction which yields

$$\vec{V}_{s/b} = (r_{s_t} \hat{i}_r \cdot \hat{i}_N)\, \hat{i}_N \qquad \text{B.35}$$

where r_{s_t} is the desired radial shock velocity. Substituting this result into Equation B.34 and simplifying with the aid of Equation B.18 yields

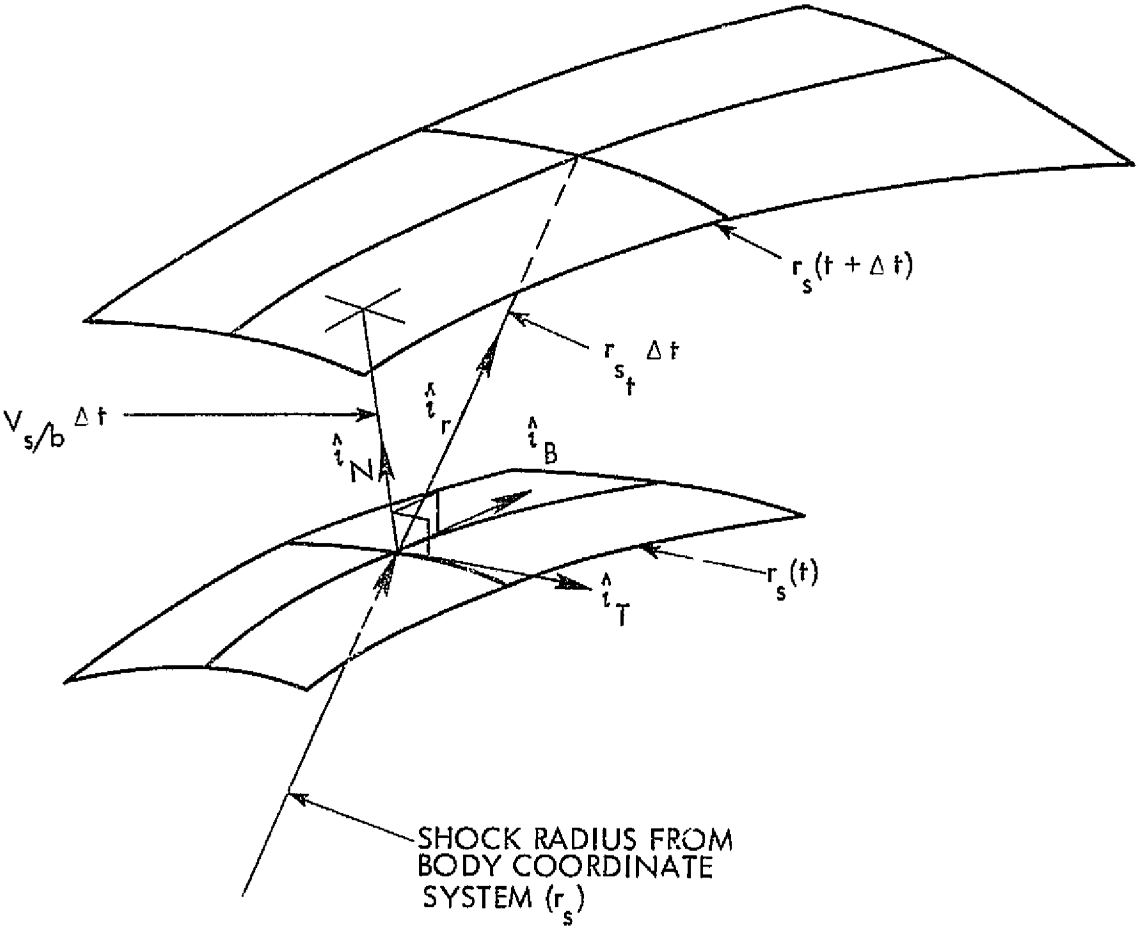

Figure B2. Notation used in the derivation of the three-dimensional radial shock velocity equation.

$$V_N = \frac{-u_{r,\infty} + u_{\theta,\infty}(r_{s_\theta}/r_s) + u_{z,\infty} r_{s_z} + r_{s_t}}{\sqrt{1 + (r_{s_\theta}/r_s)^2 + (r_{s_z})^2}} \qquad \text{B.36}$$

Solving this expression for r_{s_t} yields the final result which is given by

$$r_{s_t} = V_N \sqrt{1 + (r_{s_\theta}/r_s)^2 + (r_{s_z})^2} + u_{r,\infty}$$

$$- u_{\theta,\infty}(r_{s_\theta}/r_s) - u_{z,\infty} r_{s_z} \qquad \text{B.37}$$